

**High-resolution cryo-electron microscopy study of structure and  
dynamics of yeast fatty acid synthase by single particle analysis.**

Dissertation  
zur Erlangung des Doktorgrades  
der Naturwissenschaften  
vorgelegt im Fachbereich 14 Biochemie, Chemie und Pharmazie  
der Johann Wolfgang Goethe Universität  
in Frankfurt am Main

von  
Preeti Kumari  
Aus  
Munger  
Indien

Frankfurt am Main (2009)

(D30)

# CONTENTS

<b>ABSTRACT</b>	<b>8</b>
<b>CHAPTER 1</b>	<b>10</b>
<b>INTRODUCTION</b>	<b>10</b>
<b>1.1 FATTY ACIDS</b>	<b>10</b>
<b>1.2 FATTY ACID SYNTHESIS</b>	<b>12</b>
<b>1.3 TYPE I FATTY ACID SYNTHASE: A MEGASYNTHASE MACHINE</b>	<b>18</b>
1.3.1 MAMMALIAN FATTY ACID SYNTHASE	18
1.3.2 FUNGAL FATTY ACID SYNTHASE	21
<b>1.4 FAS INHIBITION</b>	<b>24</b>
<b>1.5 ACYL CARRIER PROTEIN</b>	<b>26</b>
<b>CHAPTER 2</b>	<b>28</b>
<b>ELECTRON MICROSCOPY &amp; METHODS</b>	<b>28</b>
<b>2.1 INTRODUCTION</b>	<b>28</b>
<b>2.2 SINGLE PARTICLE ANALYSIS</b>	<b>33</b>
2.2.1 IMAGE FORMATION	33
2.2.2 NOISE IN EM-IMAGES	33
2.2.3 CONTRAST TRANSFER FUNCTION	34
2.2.4 2D IMAGE ALIGNMENT AND CLASSIFICATION	38
2.2.5 3D-RECONSTRUCTION METHODS	41
2.2.6 RESOLUTION ASSESSMENT	46
2.2.7 MAP ANALYSIS	47
<b>2.3 MATERIALS AND METHODS</b>	<b>49</b>
2.3.1 NEGATIVE STAIN	49
2.3.2 CRYO-SAMPLE PREPARATION	49
2.3.3 ELECTRON CRYO-MICROSCOPY	50
2.3.4 X-RAY SOLUTION SCATTERING	51
2.3.5 DATA PROCESSING	51
2.3.6 RESOLUTION ASSESSMENT	52
2.3.7 ESTIMATE OF 3D-VARIANCE	52
2.3.8 MAP VISUALIZATION AND ANALYSIS	53
<b>CHAPTER 3</b>	<b>54</b>
<b>RESULTS</b>	<b>54</b>
<b>3.1 INITIAL 3D-MAP</b>	<b>54</b>
<b>3.2 HIGH RESOLUTION 3D-MAP</b>	<b>60</b>
<b>3.3 3D-MAP ANALYSIS AT 5.9 Å</b>	<b>65</b>
<b>3.4 STRUCTURE OF THE <math>\alpha_6</math> WHEEL</b>	<b>69</b>
<b>3.5 DIFFERENT ORGANIZATION OF THE REACTION CHAMBER WALL</b>	<b>71</b>
<b>3.6 MULTIPLE POSITIONS OF THE ACYL CARRIER PROTEIN</b>	<b>75</b>
<b>3.7 ACP DOCKING AND RELATIVE OCCUPANCIES</b>	<b>79</b>

<b>CHAPTER 4</b>	<b>80</b>
<b>DISCUSSION</b>	<b>80</b>
<b>PART I: ANALYSIS OF YEAST FAS EM-MAP AT 5.9 Å</b>	<b>80</b>
4.1 STRUCTURE AND DYNAMICS OF YEAST FAS	80
4.2 STRUCTURE OF THE $\alpha_6$ WHEEL	80
4.3 REACTION CHAMBER CONFORMATION AND BIOSYNTHETIC ACTIVITY	81
4.4 SUBSTRATE SHUTTLING MECHANISM	83
4.5 LINKER PEPTIDE	83
<b>PART II: SINGLE PARTICLE ANALYSIS TOWARDS HIGHER RESOLUTIONS</b>	<b>86</b>
4.6 FACTORS LIMITING HIGH-RESOLUTION IN EM	87
4.6.1 EM-DATA COLLECTION	87
4.6.2 EM-DATA PROCESSING	91
4.7 BREAKING THE RESOLUTION BARRIER FOR YEAST FAS STRUCTURE	92
4.8 NEAR-ATOMIC & SUB-NANOMETER RESOLUTION STRUCTURES BY SPA	93
4.9 CONCLUSIONS AND OUTLOOK	98
4.10 ACCESSION CODE	99
<b>BIBLIOGRAPHY:</b>	<b>100</b>
<b>ZUSAMMENFASSUNG</b>	<b>109</b>
<b>PUBLICATIONS</b>	

## LIST OF FIGURES

### CHAPTER 1

<b>Figure 1</b> Structural representation of saturated and unsaturated fatty acids where decanoic acid (C-10) is used for illustration (Nelson and Cox 2000).	10
<b>Figure 2.</b> Fatty acid synthesis reaction cycle (Gipson et al. 2009). Numbers denote the steps in the fatty acid chain elongation cycle as follows: (1)(3) acetyl/malonyl transfer; (2) condensation; (4) ketoacyl reduction; (5) dehydration; (6) enoyl reduction.	12
<b>Figure 3.</b> Structural representation of acetyl- and malonyl-CoA used as substrates in fatty acid synthesis.	13
<b>Figure 4.</b> Structural representation of thiol-group of cysteine in KS and phosphopantetheine arm of ACP found in both Type I and II FAS systems (Wakil et al.).	14
<b>Figure 5a.</b> Reaction step 1, 2 and 3 in the synthesis of fatty acids (Wakil et al. 1983)	15
<b>Figure 5b.</b> Reaction step 4, 5 and 6 in the synthesis of fatty acids (Wakil et al. 1983)	16
<b>Figure 5c.</b> Reaction step 4, 5 and 6 in the synthesis of fatty acid (Wakil et al. 1983)	17
<b>Figure 6a.</b> Diagrammatic representation of one $\alpha$ -polypeptide chain in mammalian FAS showing its linear domain organization (Maier et al. 2006).	18
<b>Figure 6b.</b> First cryo-EM map of mammalian FAS showing different views (Brink et al. 2002).	20
<b>Figure 6c.</b> X-ray structure of mammalian FAS at 4.5 Å (Maier et al. 2006).	20
<b>Figure 6d.</b> 3D-reconstructions obtained by EM of mammalian FAS showing conformational flexibility (Brignole et al. 2009).	20
<b>Figure 7a.</b> Diagrammatic representation of one $\alpha$ - and $\beta$ -polypeptide chain in fungal FAS showing its linear domain organization (Gipson et al. 2009).	21
<b>Figure 7b.</b> Early tomographic reconstruction of negatively stained yeast FAS (Hoppe 1976).	22
<b>Figure 7c.</b> Structure of yeast FAS by early single particle analysis of negatively stained specimen (Kolodziej et al. 1996).	22
<b>Figure 7d.</b> X-ray structure of fungal FAS at 3.1 Å (Jenni et al. 2007).	22
<b>Figure 8.</b> Structure of cerulenin (Morisaki et al. 1993).	25

### CHAPTER 2

<b>Figure 1.</b> Negative staining of FAS particles showing an uneven distribution of the Uranyl acetate stain.	30
<b>Figure 2a.</b> Holey-C grid showing vitrified water in the holes, where dark colored holes show thick ice.	32
<b>Figure 2b.</b> Electron micrograph showing FAS particles in different orientations embedded in vitrified water.	32
<b>Figure 3.</b> (a) Contrast transfer function for a defocus series, plots for defocus values at 2, 2.5 and 3 $\mu$ m are shown in black, blue and red respectively; (b) dark rings seen around images due to inaccurate CTF correction; (c) images with accurate CTF correction show no dark rings around them.	36
<b>Figure 4.</b> Different methods to calculate average power spectra of an EM-image: on left is shown a periodogram generation from a micrograph using the small overlapping windows method, while on right is shown usage of a particle stack obtained from a micrograph for generating an average power spectrum.	37
<b>Figure 5.</b> Flow chart representing an outline for unsupervised and supervised classification in single particle analysis.	40
<b>Figure 6.</b> (a) Pictorial representation of angular reconstitution method (van Heel 1987a) showing that at least 3 views are needed for 3D-reconstruction of any asymmetric structure. (b) Sinogram correlation function for two different views of FAS.	42
<b>Figure 7.</b> Principle of random conical tilt method, showing how many rotated images within a cone come together to form a surface (Radermacher et al. 1987).	43
<b>Figure 8a.</b> Back projection reconstructs an image by taking each view (shown as 1D view 1, 2 & 3) and "smearing" it along its direction of projection. The resulting image shown as a 2D disc in (a) is a blurry	

version of the original image. When a sufficient number of views are used during back projection the object can be reconstructed more accurately as shown as a 2D disc in (b) (Smith 2002). \_\_\_\_\_ 45

**Figure 8b.** Forward projection of the reconstructed image (shown as a 2D-disc here) in the direction of the original views (shown as 1D views here) produces its “re-projections”. A comparison between the original projection and its re-projection can be used to assess if the images were assigned correct angles during back-projection (Smith 2002). \_\_\_\_\_ 45

**Figure 9. (a) & (b)** represent the mapping of Euler angles on a sphere for a set of FAS particles, where the former shows an uneven distribution of views, while the latter represents a more evenly distributed set of views. \_\_\_\_\_ 46

### CHAPTER 3

**Figure 1.** Flow chart for *ab initio* model building using the angular reconstitution approach: the projections assigned with wrong Euler angles does not match its re-projection (encircled in red). \_\_\_\_\_ 56

**Figure 2b.** Slices (3.6 Å thick) of the initial 3D-volume parallel to the equator. \_\_\_\_\_ 57

**Figure 2a.** Views of the initial 3D-model (D3 symmetry) of yeast FAS at 18 Å showing two side views along the two-fold axes and a top view along the 3-fold axis of the barrel. \_\_\_\_\_ 57

**Figure 2c:** Initial model showing one reaction chamber of yeast FAS at 18 Å as seen in a side view and down the 3-fold axis. The color scheme represents different domains contributed by  $\alpha$  and  $\beta$ -chains in one reaction chamber (Johansson et al. 2008). \_\_\_\_\_ 58

**Figure 3:** Fitting of yeast FAS X-ray structure (Leibundgut et al. 2007) into the initial EM-map (shown for one dome). \_\_\_\_\_ 59

**Figure 4.** Image data. (a) Electron micrograph showing different orientations of FAS particles in vitreous ice at 1.5  $\mu\text{m}$  defocus (scale bar, 260 Å). (b) Representative class averages of characteristic top and side views with (c) corresponding map re-projections. \_\_\_\_\_ 62

**Figure 5.** (a) SNR plot of an image from the second dataset showing signal at sub-nanometer resolutions generated using CTFIT in EMAN (Ludtke et al. 1999). (b) Fourier shell correlation plot indicating map resolution at 0.5 cut-off, comparing half datasets (Bottcher et al. 1997) (7.2 Å; green) and the full dataset (Rosenthal and Henderson 2003) at 0.143 cut-off (5.9 Å; red) \_\_\_\_\_ 63

**Figure 6.** X-ray solution scattering curve for yeast FAS representing a 3D- rotationally averaged, normalized, intensity (Y-axis) at different spatial frequencies (X-axis). The scattering profile was applied to restore amplitude decay caused by the CTF-envelope in EM-images \_\_\_\_\_ 64

**Figure 7.** Diagrammatic representation of one  $\alpha$ - and  $\beta$ -polypeptide chain in fungal FAS representing the color scheme used for different domains in the subsequent figures. \_\_\_\_\_ 65

**Figure 8.** 3D map of yeast FAS at 5.9 Å resolution, without and with the domains of the X-ray structure (pdb 2VKZ) (Johansson et al. 2008) fitted as rigid bodies. The domains are colored as per the color scheme shown in Fig. 8; (a, b) Side view of the  $\alpha_6\beta_6$  assembly. (c, d) Central map section showing the  $\alpha_6$  wheel. (e, f) The helix pair near the KS dimer on the outside of the  $\alpha_6$  wheel showing the helix pitch. \_\_\_\_\_ 66

**Figure 9.** Details of the EM map with fitted structure (a, b) The MPT domain (red), which is mainly  $\alpha$ -helical, and the DH domain (orange), which is rich in  $\beta$ -sheets, shown in two different views. \_\_\_\_\_ 67

**Figure 10.** Clear density is visible for the FMN cofactor (orange) in the ER domain (yellow). \_\_\_\_\_ 68

**Figure 11.** Complete structure of  $\alpha_6$  wheel. (a) Differences between yeast (yellow, 2VKZ)<sup>17</sup> and *Thermomyces* FAS (blue, 2UV9) (Jenni et al. 2007); yellow arrows indicate EM density and structure of the yeast model not present in *Thermomyces* FAS. Blue arrow indicates the position of the KR four-helix bundle as seen in the *Thermomyces* X-ray structure, the purple arrow points at the corresponding density in the EM map. (b) Fit of the PPT domain (gold) (2WAS) (Johansson et al. 2009) to the EM density at the KS dimer (cyan). The density is shown at 1.5 $\sigma$  isosurface threshold. \_\_\_\_\_ 70

**Figure 12.1.** Differences between the yeast FAS structure fitted to the EM map and the X-ray structure (2VKZ) (Johansson et al. 2008). Fitted domains are colored according to figure 8, while the corresponding X-ray structure is white. (a) Remodeling of the MPT domain in the EM map density. (b).The MPT domain is displaced by ~10 Å in the crystal structure. The  $\alpha$ -helical hairpin loop protruding into the solvent is encircled in yellow. \_\_\_\_\_ 72

**Figure 12.2.** Differences between the yeast FAS structure fitted to the EM map and the X-ray structure (2VKZ) (Johansson et al. 2008). Fitted domains are colored according to figure 8, while the

corresponding X-ray structure is white. (a) Remodeling of the DH and MPT domains in the EM map density. (b) The X-ray structure (white) does not fit the structural domain near the three-fold axis (encircled in yellow). Refitting (pink) reveals a movement of up to 15 Å. The contact with the adjacent AT domain (green) remains intact. \_\_\_\_\_73

**Figure 13.** Overall differences between the yeast FAS structure fitted to the EM map (color scheme Fig. 8) and the X-ray structure (2VKZ, white) (Johansson et al. 2008). (a) The trimer contact at the tip of the barrel is completely different in the EM and X-ray structures. The double-headed arrow indicates the movement of this helix in the crystal structure with respect to the EM- structure. (b) Side view of one dome (scale bar, 20 Å); the arrows indicate the overall movement of domains in the crystal structure relative to the EM map due to compression by crystal contacts. Overall, the FAS barrel is shorter by ~20 Å and the dome is wider by up to 18 Å in solution. \_\_\_\_\_74

**Figure 14.** (a) Catalytic domains in one reaction chamber shown as colored spheres (b) Slice (20 Å thick) of the 3D-variance map (light blue) of the EM FAS-structure (yellow) as seen from the top of the barrel. \_\_\_\_\_75

**Figure 15.** Multiple locations of the ACP domain in the reaction chamber. The domains are colored according to figure 1, depending on which catalytic domain they are next to. The walls of the reaction chamber are contoured at  $2\sigma$ , while the ACP densities are contoured at  $1.5\sigma$ . The ACP X-ray structure (Johansson et al. 2008) is shown as a purple ribbon fitted to the EM-density. (a) Section through two reaction chambers with ACP density next to the AT (green) and the KS domain (cyan); (b) ACP next to the KR (blue) and KS (cyan) domain; (c) ACP next to the AT (green) and ER (yellow) domains. \_\_\_\_\_77

**Figure 16.** Movement of ACP in the reaction chamber. The three chambers in one dome are delineated by structural domains (light green). \_\_\_\_\_78

## CHAPTER 4

**Figure 1.** A slice view of 45 Å thickness showing the crystal contacts seen in all crystals of yeast and *Thermomyces* FAS. \_\_\_\_\_82

**Figure 2.** Two ~50 Å-long densities in the reaction chamber, at an isosurface threshold of  $1.6\sigma$ . The densities are not resolved in the X-ray structures and might correspond to the peripheral linker peptide which connects the ACP ( $1.5\sigma$ , yellow mesh) to the  $\alpha$  chain segment (cyan) of the MPT domain (red). Secondary structure prediction of peripheral ACP linker obtained from PHYRE server can be seen below (c: coil, h:  $\alpha$ -helix, e:  $\beta$ -sheet). The linker sequence is shown below the green bar, while the neighboring MPT and ACP domains are presented below red and purple bars respectively. \_\_\_\_\_85

**Figure 3.** SNR plot of images of amorphous film recorded on CCD and photographic film. Solid line represents the SNR calculated from image collected on CCD, dotted line represents the SNR calculated from digitized image taken on film (Booth et al. 2004). Table (below) shows the variation of sampling value, specimen area and  $2/5$  Nyquist frequency at an effective magnification relative to those at 82,800x magnification (Booth et al. 2004; Stagg et al. 2008). \_\_\_\_\_90

**Figure 4.** Near-atomic resolution structures by SPA. (A) Overall structure of rotavirus filtered at 20 Å (a); (b) a single viral protein (VP6) at 3.88 Å; (c) & (d) fitting of side chains from the corresponding X-ray structure into the EM-density (shown at 3.88 Å) (Zhang et al. 2008). (B) Overall structure of CPV virus at 3.88 Å (a); (b) an asymmetric unit (at 3.88 Å); (c) & (d) EM-density for an alpha-helix and individual beta-strands fit with the corresponding X-ray structure; (e) fit of C $\alpha$ -model of a  $\beta$ -strand into the EM-density, the EM-map shows clear density for side-chains (Zhou 2008). \_\_\_\_\_93

**Figure 5.** Low-symmetry structures obtained by SPA at 5-6 Å. (A), (B) & (C) overall structure of GroEL at 6 Å, 5.4 Å and 4.2 Å respectively (Ludtke et al. 2008); (D) overall structure of yeast FAS at 5.9 Å, where a side-view and the equatorial-wheel are shown (Gipson et al. 2009). \_\_\_\_\_94

**Figure 6.** Asymmetric structures obtained by SPA at 6-7 Å. (A) & (B) a surface representation of ribosome along with elongation factor EF-Tu at 6.4 Å (left) (Schuette et al. 2009); structure of ribosome bound to signal recognition complex (SRP) at 7.4 Å resolution (right) (Halic et al. 2006). \_\_\_\_\_95

## LIST OF TABLES

### CHAPTER 2

*Table 1. Freezing conditions, where blue and green colors are for values corresponding to initial data and the second high-resolution dataset:* \_\_\_\_\_ 50

*Table 2. Imaging conditions, where the color scheme is the same as used in Table 1:* \_\_\_\_\_ 51

### CHAPTER 2

*Table 1-4. Imaging conditions of various structures (submitted in EM-database with their respective EMID) solved in a resolution range of 3-4 Å (Table 1), 4-5 Å (Table 2), 5-6 Å (Table 3), 6-8 Å (Table 4) by SPA.* \_\_\_\_\_ 96

## ABSTRACT

This thesis presents a 5.9 Å map of yeast FAS obtained by cryo-electron microscopy using single particle analysis (SPA). The EM-map has been analyzed both by quantitative and qualitative analysis to aid in understanding of the structure and dynamics of yeast FAS. This study approaches the factors limiting the resolution in EM (>20 Å) and further discusses the possibilities of achieving higher-resolutions (<10 Å) in cryo-EM by single particle analysis.

Here, SPA is highlighted as a powerful tool for understanding the structure and dynamics of macro-molecular complexes at near native conditions. Though SPA has been used over the last four decades, the low-resolution range (20-30 Å) of the method has limited its use in structural biology. Over the last decade, sub nanometer resolution (<10 Å) structures solved by SPA have been reported --both in studies involving symmetric particles, such as GroEL (D7) and asymmetric particles, such as ribosomes (C1). Recently, near-atomic resolution in the range of 3.8-4.2 Å has been achieved in cases of highly symmetric icosahedral viral capsid structures as well. The yeast FAS structure (D3) presented here is one of two low symmetry structures submitted to the EM-database in a resolution range of 5-6 Å; the other being GroEL (D7).

Fatty acid synthase (FAS) is the key enzyme for the biosynthesis of fatty acids in living organisms. There are two types of FAS, namely the type II FAS system in prokaryotes, consisting of a set of individual enzymes, and type I FAS found in eukaryotes as a multi-enzyme complex. Yeast fatty acid synthase (FAS) is a 2.6 MDa barrel-shaped multienzyme complex, which carries out cyclic synthesis of fatty acids. By electron cryo-microscopy of single particles we obtained a 3D map of yeast FAS at 5.9 Å resolution. Compared to the crystal structures of fungal FAS, the EM map reveals major differences and new features that indicate a considerably different arrangement of the complex in solution, as well as a high degree of variance inside the barrel. Distinct density regions in the reaction chambers next to each of the catalytic domains fit well with the substrate-binding acyl carrier protein (ACP) domain. In each case, this resulted in the expected



distance of  $\sim 18 \text{ \AA}$  from the ACP substrate binding site to the active site of the catalytic domains. The multiple, partially occupied positions of the ACP within the reaction chamber provide direct insight into the proposed substrate-shuttling mechanism of fatty acid synthesis in this large cellular machine.

# CHAPTER 1

## INTRODUCTION

### 1.1 Fatty Acids

Fatty acids are composed of a long hydrophobic hydrocarbon tail and a hydrophilic carboxylic ( $-\text{COOH}$ ) head group (Nelson and Cox 2000) (Fig. 1). The carboxyl group of fatty acids is highly reactive and as a result, almost all fatty acids in a cell are found covalently attached to other molecules. Two different types of fatty acid are characterized based on their chemical structure: saturated and unsaturated fatty acids (Fig. 1).

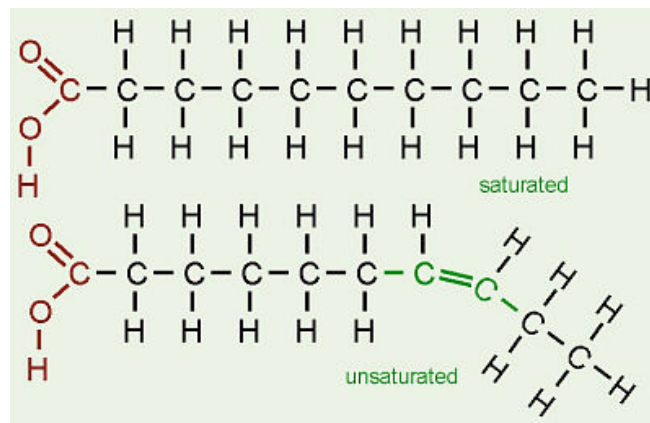


**Figure 1** Structural representation of saturated and unsaturated fatty acids where decanoic acid (C-10) is used for illustration (Nelson and Cox 2000).

Saturated fatty acids have the maximum number of hydrogen atoms in the acyl-chain as they do not contain any double bonds in their hydrocarbon tail. Palmitic (C-16) and stearic (C-18) acids are two commonly found saturated fatty acids in both plant and animal cells. The hydrocarbon tail of unsaturated fatty acids contain one or multiple double bonds leading to mono- or polyunsaturated fatty acids respectively, for e.g. oleic

acid is a mono-saturated fatty acid. The presence of a double bond causes a kink in the hydrocarbon tail of unsaturated fatty acids (Fig.1).

Fatty acids are one of the essential components required for cellular proliferation and development (Harwood 1988; Kniazeva et al. 2004). Fatty acids and their derivatives, such as triacylglycerols, phospholipids, steroids constitute a diverse group of biological compounds called lipids. The intrinsic amphiphilic property of lipids has been used by nature during evolution in cellular and sub-cellular compartmentalization by forming membranes such as phospholipids and galactolipids predominant in animal and plant cell membranes respectively. The C-C bonds in the acyl chains of fatty acids are used in the storage of metabolic energy; such as storage lipids contribute 80% of the mass of an adipocyte cell (Nelson and Cox 2000). A smaller group of lipids participate actively in metabolic pathways as metabolites and messengers (Nelson and Cox 2000). Some of them act as potent blood transported signals such as steroid hormones, or as intracellular messengers such as phosphatidylinositols and sphingosine triggered by extracellular signals. Eicosanoids are paracrine hormones, which are not transported by blood and therefore act only on cells near the point of hormone synthesis, they are derived from arachidonic acid which is a 20-C polyunsaturated fatty acid. Eicosanoids are namely prostaglandins, thromboxanes and leukotrienes, which can stimulate contraction of uterine wall during labor, blood clotting and contraction of the muscle lining the airways to the lung respectively.

## 1.2 Fatty Acid Synthesis

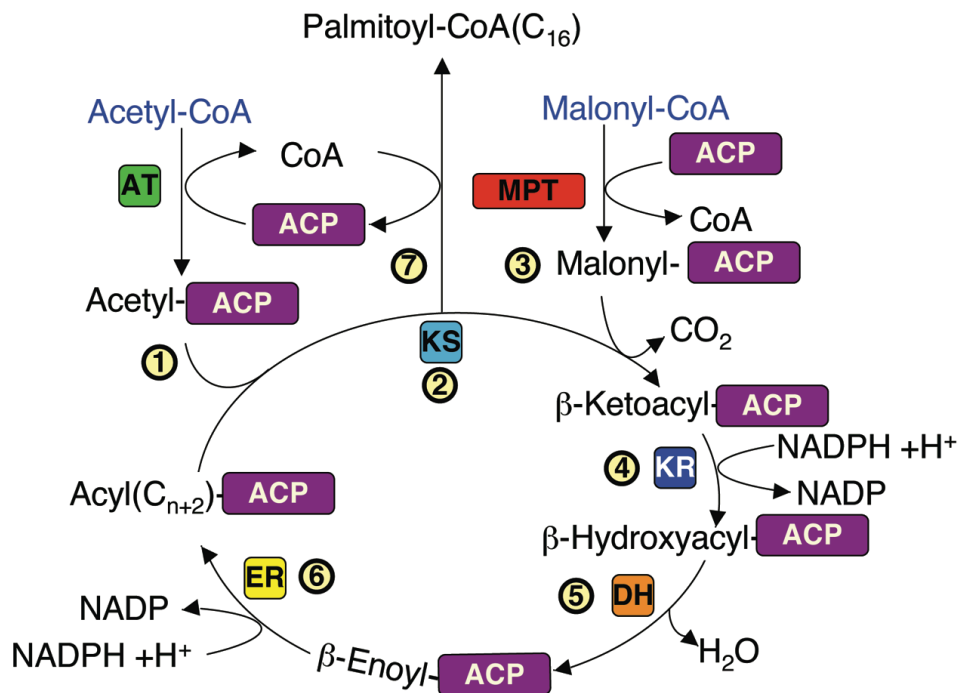


**Figure 2.** Fatty acid synthesis reaction cycle (Gipson et al. 2009). Numbers denote the steps in the fatty acid chain elongation cycle as follows: (1)(3) acetyl/malonyl transfer; (2) condensation; (4) ketoacyl reduction; (5) dehydration; (6) enoyl reduction.

Synthesis of fatty acids is a complex cellular process and exists as a highly conserved pathway in all organisms (Wakil et al. 1983) (Fig. 2). Fatty acid synthase (FAS) represents a complete enzymatic system for *de novo* biosynthesis of fatty acids. In nature two types of FAS systems are observed: the Type II system which exists as a set of individual enzymes, as found in prokaryotes (White et al. 2005) and the Type I system which forms multi-enzyme complexes, as found in eukaryotes (Wakil et al. 1983; Brink et al. 2002).

Acetyl and malonyl groups are the precursors in the synthesis of fatty acids in the cell (Fig. 3) (Wakil et al. 1983). These substrates are the intermediates of several biosynthetic pathways and are stabilized in the cell by attachment to the thiol group of coenzyme-A, which in turn delivers these moieties to various enzymatic pathways such as fatty acid synthesis, fatty acid oxidation and citrate acid cycle.

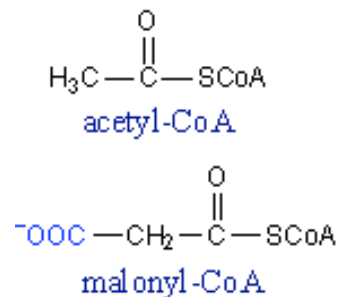


**Figure 3.** Structural representation of acetyl- and malonyl-CoA used as substrates in fatty acid synthesis.

The attachment of the acyl-substrates (Fig. 2) during fatty acid synthesis uses two thiol groups present in FAS: the thiol group of cysteine moiety present in the condensing enzyme called ketoacyl synthase, and the thiol group consisting of a long phosphopantetheine arm present on the acyl carrier protein (ACP, Fig. 4) (Wakil et al. 1983). The Phosphopantetheine transferase (PPT) enzyme present in FAS is responsible for the attachment of the phosphopantetheine group to a hydroxyl group of serine in ACP. This covalently attached phosphopantetheine group acts as a flexible ~18 Å long arm for the delivery of substrate to different catalytic sites during fatty acid synthesis (Leibundgut et al. 2007).

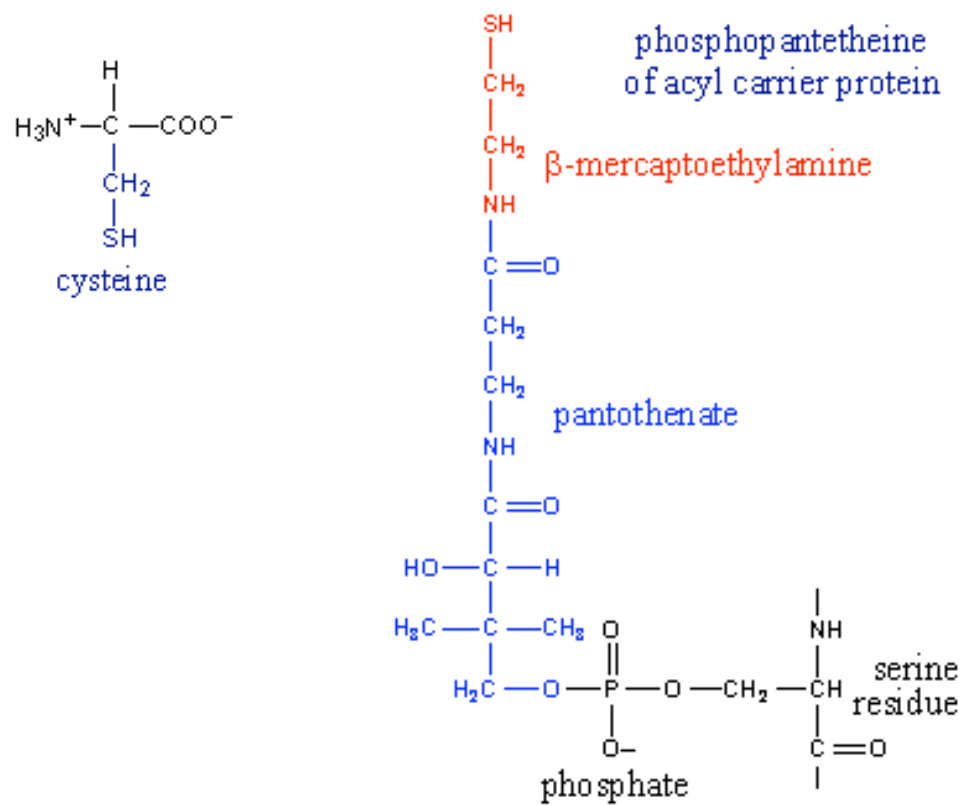


**Figure 4.** Structural representation of thiol-group of cysteine in KS and phosphopantetheine arm of ACP found in both Type I and II FAS systems (Wakil et al.).

On the following pages, the steps involved in the synthesis of fatty acids are described (acetyl-group colored blue, malonyl in red, reaction steps highlighted yellow) (Wakil et al. 1983):

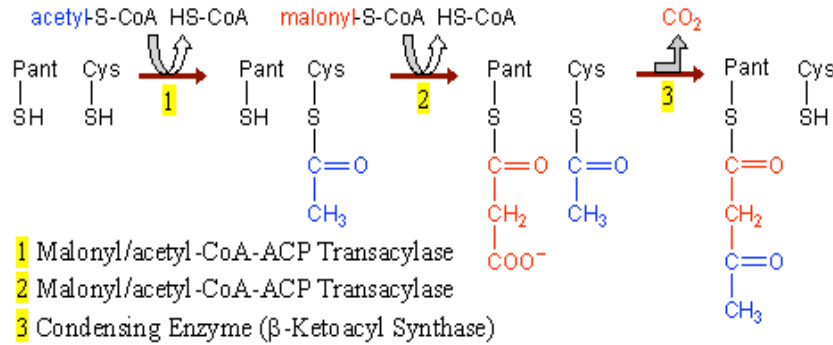


**Figure 5a.** Reaction step 1, 2 and 3 in the synthesis of fatty acids (Wakil et al. 1983)

**Step 1/Acetyl Transfer:** The acetyl group delivered by Co-A is transferred to a serine hydroxy group of malonyl-acetyl transferase (MAT) in mammalian FAS, while in yeast FAS it is transferred to the acetyl transferase (AT) domain (Fig. 5a).

**Step 2/Malonyl Transfer:** Substrate malonyl delivered by Co-A attaches to MAT in mammalian FAS and to the malonyl-palmitoyl transferase (MPT) domain in yeast FAS. The acetyl substrate is transferred to the -SH group of the cysteine of the condensing enzyme called ketoacyl synthase. Both malonyl and acetyl substrates are transferred by the -SH group of the pantetheine arm of ACP to the KS domain (Fig. 5a).

**Step 3/Condensation:** The KS domain catalyzes the condensation step of acetyl and malonyl groups where a decarboxylation reaction, i.e. release of a  $\text{CO}_2$  molecule occurs (Fig. 5a).

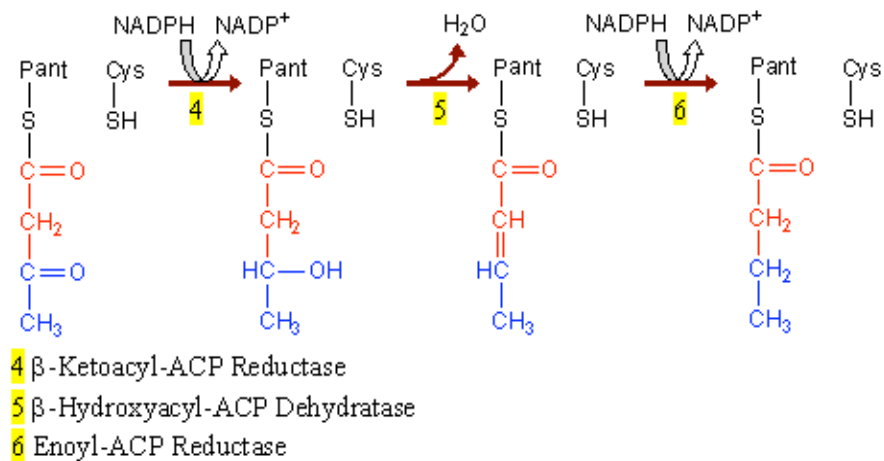


*Figure 5b. Reaction step 4, 5 and 6 in the synthesis of fatty acids (Wakil et al. 1983)*

**Step 4/Reduction:** In this step, the ketone (C=O) group is reduced by the enzyme ketoacyl reductase (KR) where NADPH is used as a reducing agent (Fig. 5b).

**Step 5/Dehydration:** In this step, the hydroxyl generated in step 4 is dehydrated by the enzyme dehydratase (DH) where one H<sub>2</sub>O molecule is released (Fig. 5b).

**Step 6/Reduction:** The C=C bond generated in step 5 is reduced by the enzyme enoyl reductase (ER) where NADPH is used as the electron donor (Fig. 5b).



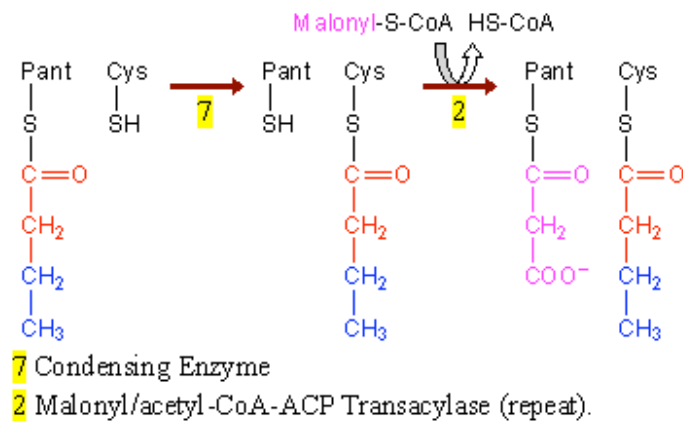


*Figure 5c. Reaction step 4, 5 and 6 in the synthesis of fatty acid (Wakil et al. 1983)*

**Step 7:** The acyl-substrate is transferred to the condensing enzyme by the pantetheine of the ACP domain to the condensing enzyme KS domain and the complete cycle begins again (Fig. 5c).

**Step 8:** Once a fatty acid of chain length C-16 to -18 is obtained, it is released into the cytosol by attachment to the highly polar Co-A, which is catalyzed by the MPT domain in yeast and the thioesterase domain in the case of mammalian FAS (Fig. 5c).

The palmitate or stearate released as the end product of fatty acid synthesis is used as precursors of other long-chain saturated and unsaturated fatty acids. These products are carried by coenzyme-A for further processing to a set of fatty acid elongation systems located in the smooth endoplasmic reticulum and mitochondria to form several other types of lipids such as triacylglycerols, glycerolipids, sphingolipids and phospholipids.

### 1.3 Type I Fatty Acid Synthase: a megasynthase machine

Type I FAS is the key enzyme for the biosynthesis of fatty acids in eukaryotes (Singh et al. 1985; Smith et al. 2003). The individual enzymes responsible for fatty acid synthesis (Fig. 2) exist as multi-enzyme complexes, where the enzymes are contributed by one or two polypeptide chains. In mammals FAS is an  $\alpha_2$  homo-dimer (Rangan et al. 2001; Brink et al. 2002; Asturias et al. 2005; Maier et al. 2006), while type I fungal FAS is an  $\alpha_6\beta_6$  hetero-dodecameric complex (Wakil et al. 1983; Singh et al. 1985; Kolodziej et al. 1996). Although fungal and mammalian FAS have very different structures, they conserve all the necessary enzymes found in the FAS type II systems required for fatty acid synthesis (Fig. 2). The following sections discuss the structural studies available on mammalian and fungal FAS.

#### 1.3.1 Mammalian Fatty Acid Synthase



**Figure 6a.** Diagrammatic representation of one  $\alpha$ -polypeptide chain in mammalian FAS showing its linear domain organization (Maier et al. 2006).

Mammalian FAS is a dimer of two  $\alpha$ -polypeptide chains (Fig. 6a), where each subunit has a molecular weight of 270 kDa (Brink et al. 2002; Asturias et al. 2005; Maier et al. 2006). Initial structural studies on this complex started in the 90s, when only topological information was available from biochemical studies (Rangan et al. 2001). Later, studies by cryo-electron microscopy (cryo-EM) revealed an initial structure (Fig. 6b) (Brink et al. 2002). These studies proposed that the two  $\alpha$ -chains are arranged in an anti-parallel, head to tail fashion. Only later, by improved EM-studies of FAS mutants, was this model proved to be wrong (Cronan 2004; Witkowski et al. 2004). Instead it was revealed that

the two polypeptide chains are arranged in a head-to-head fashion rather than an anti-parallel arrangement as suggested earlier. Recent X-ray crystallography studies (Fig. 6c), at resolutions of 4.5 Å and 3.2 Å, reveal a head to head arrangement of the monomers forming the two reaction chambers for fatty acid synthesis (Maier et al. 2006; Maier et al. 2008). So far, the mobile ACP and the thioesterase domains have not yet been resolved in any of these structures.

In spite of the above structural studies, the mechanism of mammalian FAS has remained unknown, as the expected position of the unresolved mobile ACP domain is at a long-range distance in order to reach all the catalytic sites to deliver the substrates (Fig. 6c). Only this year, EM results (Brignole et al. 2009) on mammalian FAS have shown that it is a highly flexible complex, where all the catalytic domains can undergo long-range movements (Fig. 6d). These movements include 90° swiveling of the lower domains w.r.t. the top domains, leading this protein to be known as “the dancing protein”. With these movements, and the flexibility of the multi-enzyme complex, the ACP domain in mammalian FAS is able to access its distant catalytic sites easily.

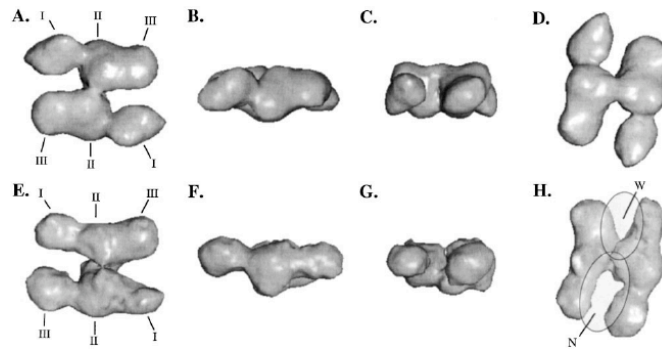


**Figure 6b.** First cryo-EM map of mammalian FAS showing different views (Brink et al. 2002).

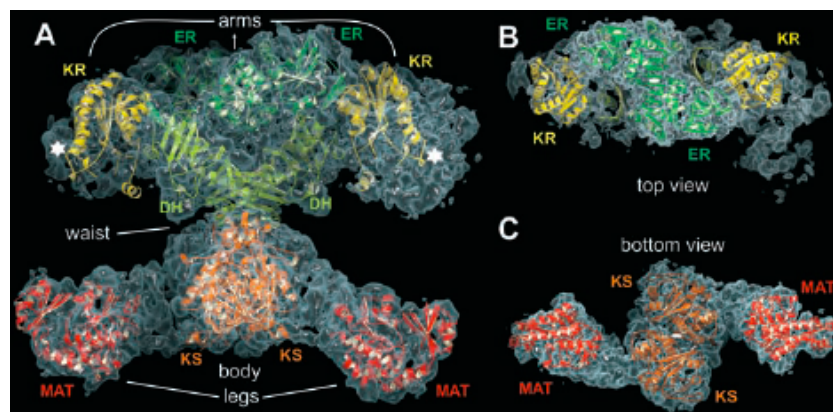


**Figure 6c.** X-ray structure of mammalian FAS at 4.5 Å (Maier et al. 2006).

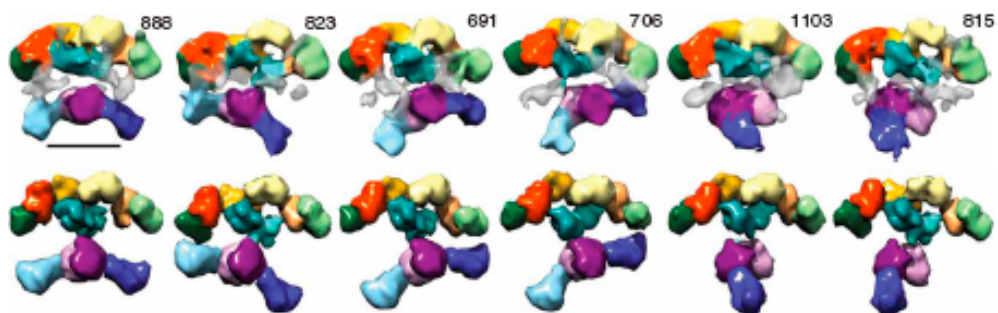


**Figure 6d.** 3D-reconstructions obtained by EM of mammalian FAS showing conformational flexibility (Brignole et al. 2009).

### 1.3.2 Fungal Fatty Acid Synthase

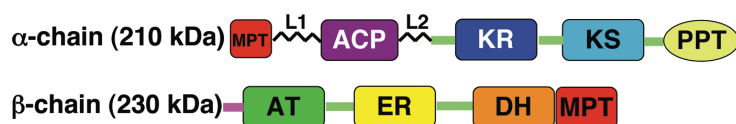


**Figure 7a.** Diagrammatic representation of one  $\alpha$ - and  $\beta$ -polypeptide chain in fungal FAS showing its linear domain organization (Gipson et al. 2009).

Fungal FAS is a 2.6 MDa multi-enzyme complex, composed of six of each  $\alpha$  and  $\beta$  polypeptide chains (Fig. 7a) (Leibundgut et al. 2007; Lomakin et al. 2007; Johansson et al. 2008). Structural studies on yeast FAS started in 1974, when it was used as an experimental sample for the first tomographic reconstructions (Fig. 7b) (Hoppe 1976). In this study tilt series of negatively stained yeast FAS sample, within an angular range -40 to +40 degrees at an increment of 10 degrees, was imaged at Seimens Elmiskop at 100kV. A 3D-reconstruction of yeast FAS from 9 projection images was generated at a resolution of  $\sim 40$  Å (Fig. 7b) by the common lines method --the method is discussed in next chapter. Further, low resolution early EM-studies (Kolodziej et al. 1996) showed that yeast FAS is a  $260$  Å x  $230$  Å barrel of D3 symmetry (Fig. 7c). Recent X-ray structures of *Thermomyces lanuginosus* (Jenni et al. 2007) and *S. cerevisiae* FAS at  $3.1$  Å and  $4.0$  Å resolution (Leibundgut et al. 2007; Lomakin et al. 2007; Johansson et al. 2008), present an essentially identical structure (Fig. 7d).

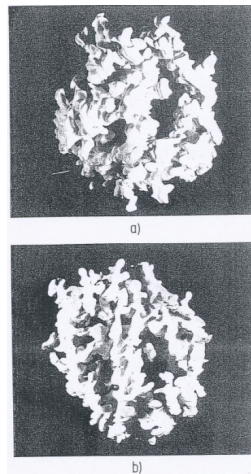


**Figure 7b.** Early tomographic reconstruction of negatively stained yeast FAS (Hoppe 1976).

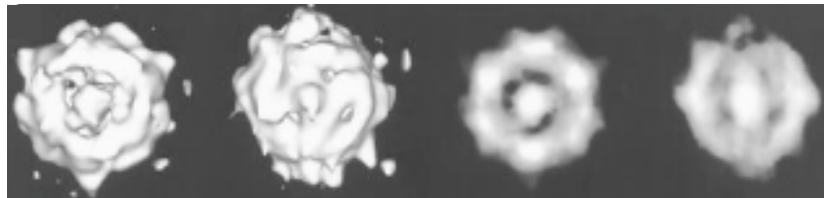


**Figure 7c.** Structure of yeast FAS by early single particle analysis of negatively stained specimen (Kolodziej et al. 1996).

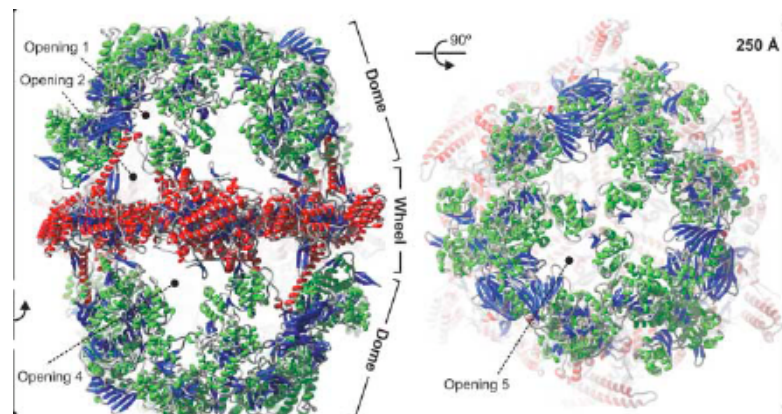


**Figure 7d.** X-ray structure of fungal FAS at 3.1 Å (Jenni et al. 2007).

The six  $\alpha$ -subunits form an equatorial wheel, which divides the barrel into two separate domes, each consisting of three  $\beta$ -subunits. The  $\alpha$ - and  $\beta$ -subunits define three reaction chambers per dome and contain eight catalytic centers. Of these, the  $\alpha$ -subunit contributes the phosphopantetheinyl transferase (PPT), acyl carrier protein (ACP), ketoacyl synthase (KS), ketoacyl reductase (KR), and part of the malonyl-palmitoyl transferase (MPT) domain. The  $\beta$ -subunit contributes the acetyl-transferase (AT), enoyl-reductase (ER), dehydratase (DH), and the major part of the MPT domain. In addition to the catalytic domains, six structural domains, two in the  $\alpha$ -subunit (SD1-2 $\alpha$ ) and four in the  $\beta$ -subunit (SD1-4 $\beta$ ), constitute the supporting framework for this mega-synthase structure. Previous stoichiometric studies involving volumetric methods (Singh et al. 1985) have shown that the reaction chambers in yeast FAS work independently of one another.

In fungal FAS, the ACP is tethered by two flexible linkers, which connect it to the MPT domain and the central hub of the equatorial wheel. The linker domains define the radius of action of the ACP, which agrees broadly with the dimensions of the reaction chamber (Jenni et al. 2007; Leibundgut et al. 2007; Lomakin et al. 2007). These flexible linkers differ in length where the short linker consisting of 25 residues i.e.,  $\sim 75$  Å in length attaches the ACP to the equator, while the long linker is a stretch of 45 residues i.e.,  $\sim 150$  Å in length, which tethers ACP to the MPT domain. These linkers have not been observed in any of the above structural studies.

With the exception of the PPT domain, the active sites of all catalytic domains face the reaction chambers in the interior of the FAS barrel (Leibundgut et al. 2007; Lomakin et al. 2007; Johansson et al. 2008), unlike in mammalian FAS where the catalytic sites face the external side of the reaction chamber (Maier et al. 2006; Maier et al. 2008).

In spite of sharing the same reaction scheme, both fungal and mammalian FAS have evolved into completely different machines for the synthesis of fatty acids. Yeast FAS exhibits a rigid cage-like structure. The structural domains contribute almost half of its molecular weight providing a rigid framework, unlike in mammalian FAS where only a

few structural domains are present (Brignole et al. 2009). Yeast mostly depends on endogenous fatty acid synthesis, and has developed the rigid cage-like FAS machinery with six-reaction chambers for the increased efficiency of fatty acid synthesis. Here, ACP is proposed (Leibundgut et al. 2007; Lomakin et al. 2007) to be the only mobile domain performing the substrate shuttling, unlike the open mammalian FAS structure which has two reaction chambers where the efficiency of the fatty acid synthesis is determined by the high conformational flexibility of the protein (Brignole et al. 2009). The proposed substrate shuttling mechanism by ACP in both fungal and mammalian FAS has not yet been observed.

#### **1.4 FAS Inhibition**

The conserved and essential biosynthetic pathway of fatty acid synthesis makes it an important target for antimicrobial drugs. The first antibiotic discovered against FAS was cerulenin (Morisaki et al. 1993), which is a natural antibiotic produced by the fungus *Cephalosporium caerulens*. Polyketide cerulenin (Fig. 8) is a competitive irreversible inhibitor which covalently binds to a cysteine residue in the binding pocket for the malonyl substrate in the KS enzyme, which in turn prevents the condensation reaction of fatty acid synthesis. Other natural antibiotics targeting the KS enzyme of FAS are platensimycin, thiolactomycin produced by *Streptomyces* species of fungi. In contrast to cerulenin which targets both type I and II FAS systems, the latter FAS inhibitors are shown to be selective towards the type II FAS system found in prokaryotes (Johansson et al. 2008). Synthetic compounds such as C75 (López and Diéguez 2007) can target multiple enzymes of the FAS system, while drugs such as isoniazid and triclosan target the ER enzyme in bacterial FAS system. Both natural and synthetic FAS inhibitors are being tested and developed as potential antibacterial drugs. In mice, FAS inhibitors have been shown to lead to a reduction in food intake and body weight (Loftus et al. 2000), where it is proposed that the inhibitors might directly affect the appetite centers in the brain. The increased levels of malonyl-CoA in the cell, due to decreased fatty acid synthesis, may lead to a reduced amount of nutrition mediated insulin hormone (Loftus et



al. 2000), hence FAS inhibitors have been proposed to be potential drugs for the treatment of obesity.

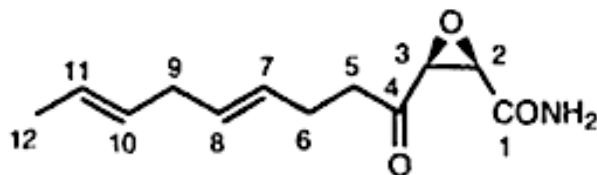


*Figure 8. Structure of cerulenin (Morisaki et al. 1993).*

In tumor cells FAS is highly expressed, as a result FAS and fatty acid metabolism has become a very important target for cancer treatment (Kuhajda 2006). The resulting over-expressed FAS produce palmitate, which drives phospholipid synthesis in tumor cells (Little et al. 2007). Several cancer studies have shown that the inhibition of fatty acid synthesis by FAS-inhibitors kills carcinoma cells, although the reason for this is an active area of investigation (Kuhajda et al. 2000; Kuhajda 2006). Some recent studies show that FAS-inhibitors induce a stress response in the endoplasmic reticulum of tumor cells, leading to the inhibition of protein synthesis, which in turn induces cell apoptosis (Little et al. 2007). The anti-tumor effects of FAS-inhibition have made FAS a potential drug target in cancer research.

For this study yeast FAS inhibited by cerulenin at the KS domain has been used, which was provided by our collaborators (Johansson et al. 2008).

## 1.5 Acyl Carrier Protein

The ACP (Majerus et al. 1965a; b) belongs to a class of universal and highly conserved carrier proteins which bind acyl intermediates via the  $\sim 18$  Å phosphopantetheine arm and are active in various metabolic pathways, including the biosynthesis of polyketides or fatty acids (Finking and Marahiel 2004; Byers and Gong 2007). Both Type I and Type II ACP have a completely  $\alpha$ -helical structure, with a conserved four-helix bundle that harbors the binding site for acyl chain intermediates. The ACP-dependent enzymatic pathways are essential for the cell, making them important potential drug target (Byers and Gong 2007).

In type I FAS systems (Schweizer and Hofmann 2004) found in yeast and mammals, ACP exists as an independent domain of the multi-enzyme complex, while in type II FAS systems (Byers and Gong 2007) in bacteria ACP is present as a small monomeric protein. In the soluble, dissociated type II FAS systems ACP carries out a sequential transfer of acyl-substrates to the different catalytic enzymes involved in fatty acid synthesis.

Yeast FAS contains six ACP domains (Lynen 1980), where one ACP is present in each reaction chamber acting as a carrier of substrates to the seven catalytic sites, thus making a very efficient machinery composed of six independently acting reaction chambers for fatty acid synthesis.

It has been postulated that the ACP domain carries the growing fatty acid chain substrate iteratively to the various catalytic sites in the reaction chamber (Leibundgut et al. 2007; Lomakin et al. 2007; Johansson et al. 2008). Of these, the AT domain participates in the initiation of fatty acid chain synthesis. The MPT, KS, KR, DH and ER domains each carry out different steps in the chain elongation cycle. The growing fatty acid chain is attached to the carrier domain, which shuttles between the successive catalytic sites. In yeast, fatty acid synthesis is carried out in the confined environment of a catalytic cage. This makes the process more efficient compared to prokaryotic type-II FAS, which relies

on the diffusion of ACP to the individual enzymes. So far, however, there has been no experimental evidence for such a substrate shuttling mechanism. In the three X-ray structures of yeast FAS (Leibundgut et al. 2007; Lomakin et al. 2007; Johansson et al. 2008) the ACP is fixed in a single position at the equator near the KS domain. The relative affinities of the catalytic domains for the ACP are unknown.

The independent nature of the six chambers, each having six catalytic sites, means that  $6^6$  (~48000) static locations for ACP are possible inside the barrel, discounting intermediate states. Such a highly random dynamic property would be unfeasible to study by any static structural method. As such, a continuous description of local structure variation is required to describe the behavior of such a system. It is possible to trace the mobility of such a mobile domain in electron density maps, by calculating a 3D-variance map of the structure using the bootstrap technique (Penczek et al. 2006a; Penczek et al. 2006b).

As discussed in this chapter, ACP has not been yet resolved in mammalian FAS and the proposed substrate shuttling mechanism has not yet been observed both in mammalian and fungal FAS, owing to the dynamic nature of the ACP domain. Cryo-electron microscopy is a method of choice for studying such dynamic proteins (Frank 2001a; b), as the freezing of the sample under its native conditions preserves all mobile and flexible domains and the electron density of such domains can be easily seen in EM-maps. The next chapter discusses different EM methods used to study the structure and function of proteins over the years.

## CHAPTER 2

# ELECTRON MICROSCOPY & METHODS

### 2.1 Introduction

One of the first biological discoveries using electron microscopy was the origin of the iridescent colors of butterfly wings (Frank 1996). Electron microscopy bridges the gap between light microscopy and X-ray crystallography, as it can be used to study scales ranging from a whole cell to a single protein molecule present in the cell. The two most commonly used forms of EM are transmission electron microscopy, where a beam of electrons is transmitted through a specimen which, due to electron-specimen interaction, produces the image of the sample. The other is scanning electron microscopy (SEM) which is a method where a focused electron beam is used to scan over small (1-5 nm) rectangular areas of the specimen and the energy lost in the process generates low-energy secondary electrons which are recorded as a signal (Frank 1996). TEM provides a high-resolution 2D-projection for a specimen, while SEM can provide a surface view of the specimen at low resolution.

Over the last four decades several techniques have been developed and applied to study different biological samples by TEM. Electron crystallography is a method used for studying proteins that exist natively as (or can be brought into the form of) highly ordered 2D-crystals, ideally one unit cell thick, and so is called 2D-crystallography (Glaeser 1999). The difference between electron (2D) and X-ray crystallography, besides the fact that X-Ray crystals are 3D, is that the availability of real-space images in the former case provides the phases, which are lost in the X-ray diffraction patterns. By the method of electron crystallography, close to atomic resolution has been achieved in several studies such as -- bacteriorhodopsin at 3.5 Å (Henderson et al. 1990) later improved to 3 Å (Mitsuoka et al. 1999), light-harvesting complex at 3.4 Å (Kuhlbrandt et al. 1994),

microtubule structure at 3.7 Å (Nogales et al. 1998), aquaporin at 1.9Å (Gonen et al. 2005).

The idea of the full 3D-reconstruction of a specimen by imaging the sample at several tilt-angles where a 3D-volume is generated by relating the tilt series was first proposed by Walter Hoppe et al., (1972), with a first attempt using yeast fatty acid synthase as a sample (Hoppe 1976). Currently it is a widely used technique known as “tomography” and the 3D- volume generated by it is called a “tomogram”. The development of tomography has helped in the understanding of the 3D-organization of sub-cellular organelles, membranes etc (Baumeister 2002). Biological samples are easily damaged at high electron doses, hence radiation damage of the sample at the microscope is one of the limiting factors for techniques such as tomography. A high total electron dose (40-80 e<sup>-</sup>/Å<sup>2</sup>) is accumulated during the collection of tilted images of the same sample. Recently, cryo-electron tomography, where the sample is embedded in ice, has become the method of choice for the study of biological samples at close to their native state (Milne and Subramaniam 2009). The method of 3D-classification and averaging which were initially applied in single particle analysis (as discussed later) are now routinely applied for the study of individual protein complexes observed in tomograms, which in turn provides a 3D-distribution of proteins in the sub-cellular environment (Milne and Subramaniam 2009). The resolution of this method is so far limited between 30-60 Å owing to the radiation damage and comparatively thick sections of biological samples (Lucic et al. 2005).

A method of direct observation of a protein molecule in EM is called “single particle analysis” (Frank 2002) (SPA) and unlike 2D-crystallography (Glaeser 1999) it uses no crystals for imaging. In electron-crystallography, redundancy of protein molecules in 2D-crystals is used to generate a virtually noise-free average. SPA also uses the same basic principle by averaging molecules in the same orientation to improve signal to noise ratio (SNR). The main advantage of studying single particles over any crystallographic method

is that the difficult task of producing crystals is not needed and proteins can be studied near their native conditions.

In the single particle method, the sample can be observed in the EM by staining the sample with heavy metal negative stains (Hall 1955; Kiselev et al. 1990) or by freezing in vitrified water (Dubochet et al. 1988). In the former case, heavy metal stains such as uranyl acetate are used to stain the sample, which scatter electrons more strongly than the light atoms (C, N, O) of biological materials, producing high contrast in the images where the sample appears lighter than the stain and hence is called the “negative-stain method” (Fig. 1). The disadvantage of this method is that the protein is not visualized directly, rather an uneven distribution of the stain on the sample is observed which can produce artifacts in the final 3D-reconstruction, while a shallow staining can lead to a flattening of the sample and the use of a carbon-support film for sample preparation leads to a distribution of proteins in a few preferred orientations.

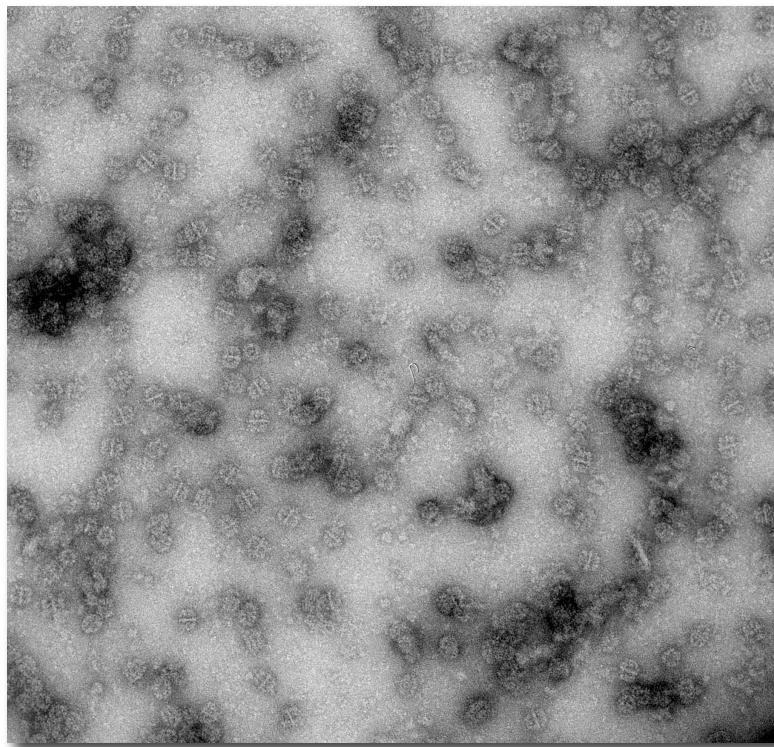


**Figure 1.** *Negative staining of FAS particles showing an uneven distribution of the Uranyl acetate stain.*

The freezing of protein sample by rapidly plunging into liquid ethane ( $-177^{\circ}\text{C}$ ) produces vitrified (“glassy”) water. When freezing is done on C-film with holes the single molecules are trapped in almost all possible orientations inside the vitrified water present in the holes (Dubochet et al. 1988) (Fig. 2a,b). Here the sample is always present in solution, which preserves the native structure of the protein. Hence, freezing of sample allows the visualization of the protein sample in its most native form, unlike in crystallization methods where the protein may not be in its physiological form due to crystallization conditions and induced crystal contacts. The limiting factor in achieving high-resolution from frozen samples using SPA is the poor-contrast of images, due to which its usage is limited to particles with mass  $>100$  kDa (Henderson 1995).

Recent development of several computational algorithms to overcome the technical problems has produced near atomic resolution (Zhang et al. 2008; Zhou 2008) ( $\sim 3.8\text{-}4.5$  Å) in studies of large highly symmetric complexes such as viruses (Jiang et al. 2008; Yu et al. 2008), and structures of less symmetric molecules. These include GroEL (seven-fold) at  $4.2$  Å (Ludtke et al. 2008) and even asymmetric molecules such as ribosomes at  $7.5$  Å (Matadeen et al. 1999) using SPA. In all these methods, several thousands of images were used to improve the SNR in the final reconstructions by the averaging techniques discussed later. Our study using the single particle method has produced a  $5.9$  Å 3D-map of yeast fatty acid synthase (D3) using  $\sim 19000$  particles (Gipson et al. 2009). The method used for this study will be further introduced in relevant details in the subsequent sub-sections.

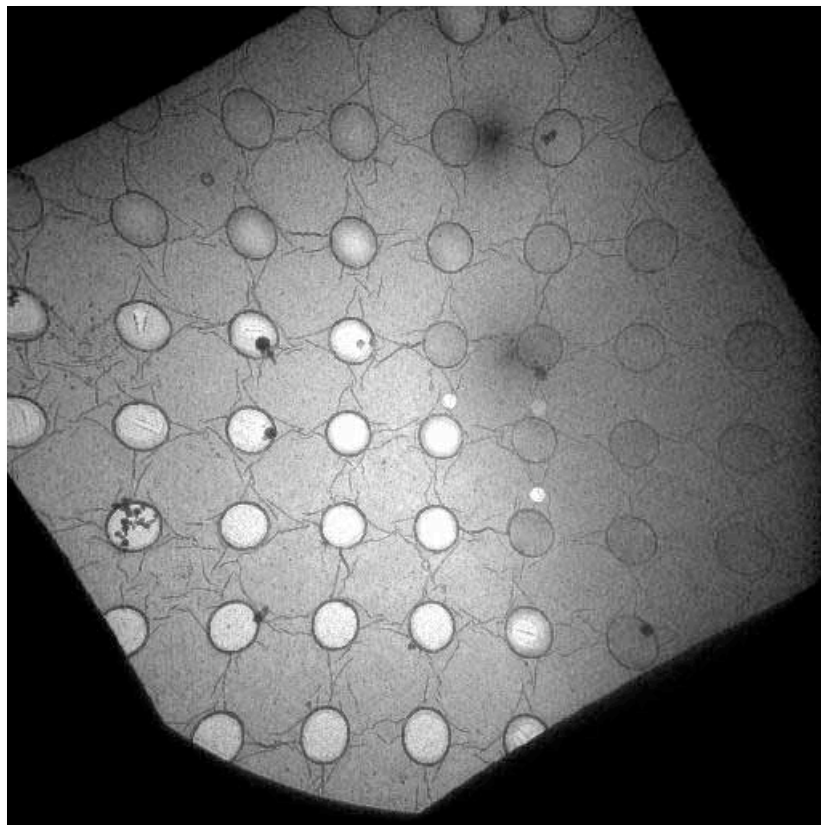


*Figure 2a. Holey-C grid showing vitrified water in the holes, where dark colored holes show thick ice.*



*Figure 2b. Electron micrograph showing FAS particles in different orientations embedded in vitrified water.*



## **2.2 Single Particle Analysis**

### **2.2.1 Image formation**

In EM an image is formed due to the electron-specimen interaction, which results in elastic and inelastic scattering of electrons (Frank 1996). Elastic scattering involves no energy loss, has a wide angular distribution and gives rise to high resolution information. While inelastic scattering involves a loss of energy, has a narrow angular distribution and leads to undesired background noise (low resolution) in the image. The phase shift resulting from elastic scattering leads to interference between the scattered and unmodified incident beam; this generates the phase-contrast in the image. The virtual loss of electrons in the event of both elastic and inelastic scattering contributes to the amplitude contrast in the image. The images collected from the electron microscope especially in the case of biological samples have low signal to noise (SNR) ratio, due to poor scattering by low atomic weight elements such as C, H, O and N constituting the biological samples. Improving the SNR in EM-images constitutes the major part of data processing. The sources and types of noise present in EM-images are described next.

### **2.2.2 Noise in EM-images**

Noise in an image can be of two kinds: “stochastic noise” and “fixed pattern noise” (Frank 1996). The latter can be produced by instruments, such as by damage to the pixels on the CCD, but subtraction or division can easily remove this as it is constant across all images. On the other hand, stochastic noise is difficult to determine as it can be contributed to by various sources and can be both “signal-dependent and -independent” noise. The sources of noise also include the medium on which the image is collected such as CCD or photographic emulsions. In the former case the noise is added due to the statistical variation in the number of electrons reaching the recording plate, also called “shot noise”. In the case of the photographic images the noise is contributed by the irregular distribution of silver grains in the electron micrographs and digitization of images which also adds some noise due to the conversion of continuous optical densities to discrete values (DeRosier and Klug 1968). In order to reduce the noise from electron

micrograph images an increase in magnification can be used as it causes a contraction of the specimen's spectrum relative to the noise spectrum in Fourier space. This occurs as the change in magnification is inversely related to the amount of information presented by a fixed size silver grain on a photographic film. Therefore, with an increase in magnification the noise level remains constant, whereas the information in the image increases. (Frank 1996). Additionally, scanning of images on a 16-bit scale, which has 65536 values, rather than an 8-bit scale, which has 256 values, provides a higher dynamic range.

### 2.2.3 Contrast Transfer Function

As mentioned above, contrast in an EM image is contributed by both amplitude and phase effects. Variations in phase and amplitude contrast form the contrast transfer function (CTF) of the microscope (Fig. 2a). Otto Scherzer in the 1950s derived the formula for the CTF of an electron microscope, given as follows:

*Scherzer's formula:*

$$\gamma(u) = 2\pi W/\lambda = \pi/2 [ C_s \lambda^3 u^4 - 2\Delta z \lambda u^2 ]$$

$\sin(\gamma(u))$  = phase contrast transfer function

$\cos(\gamma(u))$  = amplitude contrast transfer function

$u$  = scattering vector ( $\sim$ scattering angle)

$W$  = wave function

$\lambda$  = electron wavelength

$\Delta z$  = defocus

$C_s$  = spherical aberration constant

An artificial phase-shift is introduced in the images by defocusing the electron beam in order to improve the phase contrast in images at particular resolution ranges (Frank

1996). This leads to the fluctuation of the CTF between positive and negative values, and induces several zeroes, i.e. information loss, in the spectrum of an image based on the chosen defocus value. The CTF can be corrected by using existing methods (Frank 1996) such as:

*phase-flipping:*

$$\text{NewImage} = \text{FT}^{-1} \{ \text{FT}(\text{Image}) \cdot \text{sign}(\text{CTF}) \}$$

*multiplication with the CTF:*

$$\text{NewImage} = \text{FT}^{-1} \{ \text{FT}(\text{Image}) \cdot (\text{CTF}) \}$$

*and Wiener filtering:*

$$\text{NewImage} = \text{FT}^{-1} \{ \text{FT}(\text{Image}) \cdot (\text{CTF}) / (\text{CTF}^2 + \text{N}^2) \}$$

Here, FT = Fourier transform; N = Noise in image

The most commonly used method is phase-flipping, while the zeroes are filled in by taking data from different defocus range such that the various CTF curves compensate for each other's zeroes (Penczek et al. 1997) (Fig. 3a). An accurate defocus determination is crucial, as an error in the CTF correction applies inappropriate phase reversals, qualitatively appearing as dark rings around the images (Frank 1996) (Fig. 3b, c) and thus produces artifacts in the final 3D-reconstruction. In order to determine the defocus for each micrograph a “periodogram” (Schuster 1898) can be generated which represents the average of the power spectrum for several overlapping sub-windows in a micrograph (Fig. 3). Scant particle distribution on the micrograph, however, can produce too low signal to calculate an accurate defocus value (Fig. 4). CTF determination from an averaged particle stack from each micrograph produces better signal, and hence better estimation of the CTF zeroes (Fig. 4).

**Figure 3.** (a) Contrast transfer function for a defocus series, plots for defocus values at 2, 2.5 and 3  $\mu\text{m}$  are shown in black, blue and red respectively; (b) dark rings seen around images due to inaccurate CTF correction; (c) images with accurate CTF correction show no dark rings around them.

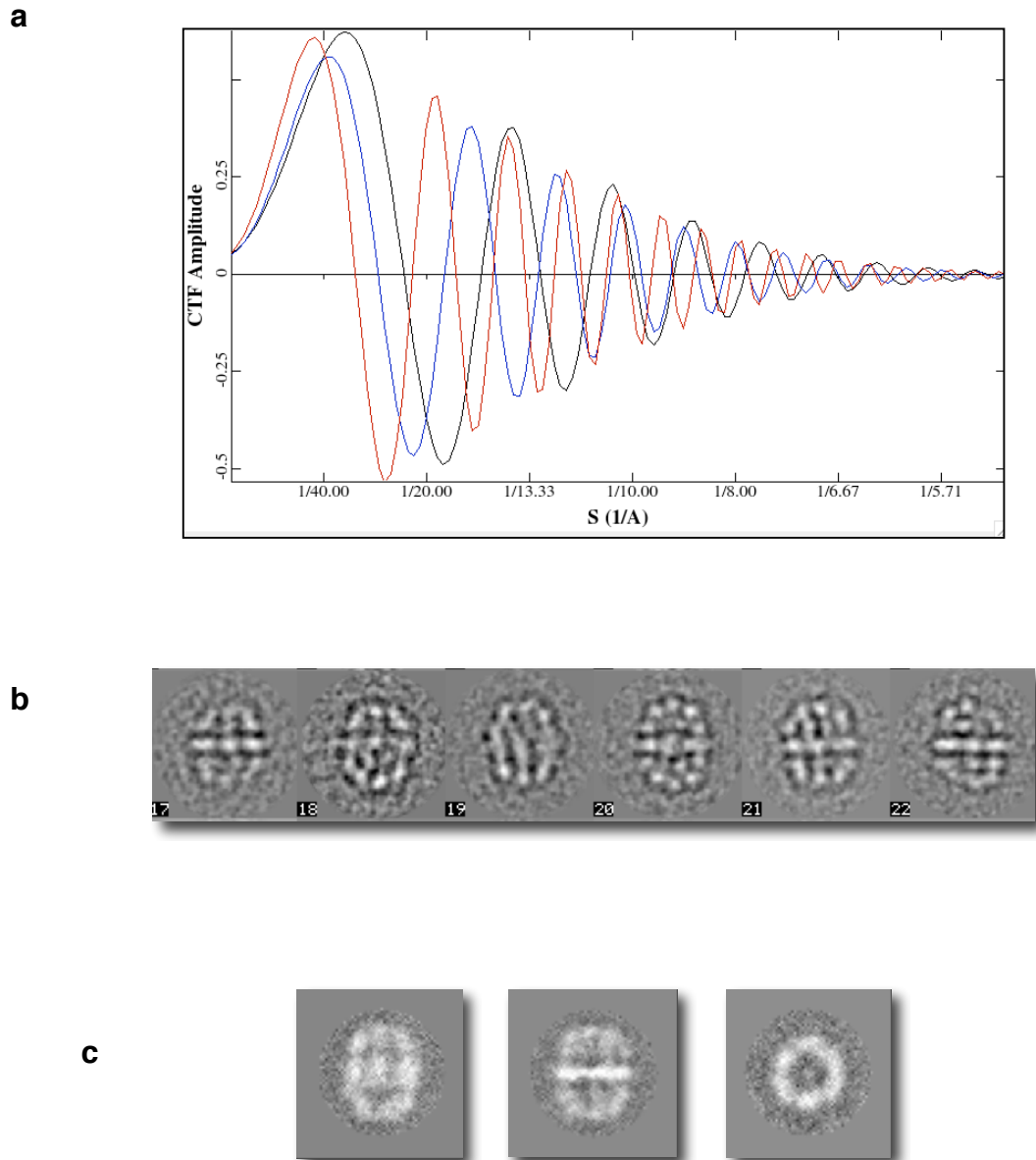
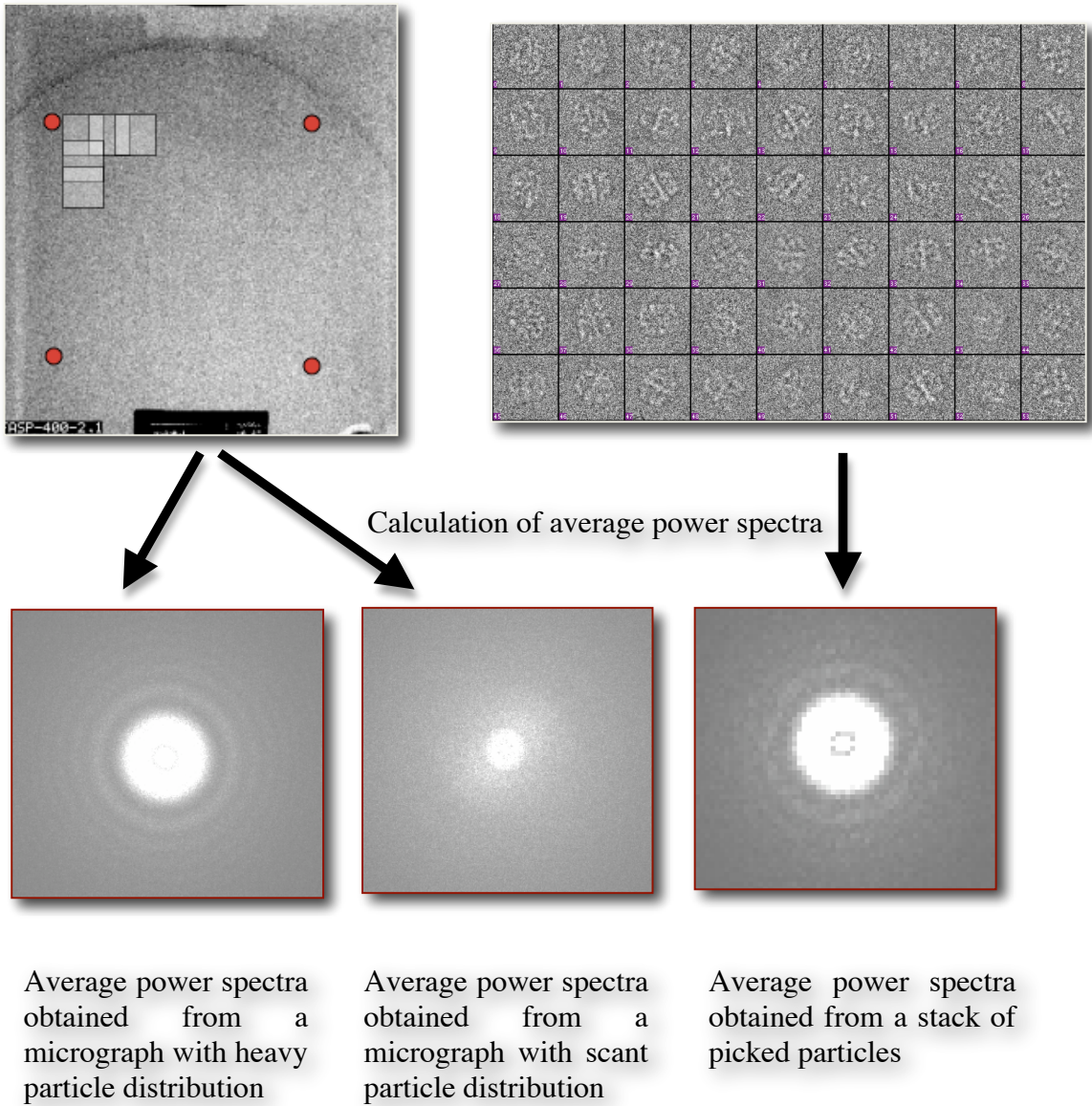


**Figure 4.** Different methods to calculate average power spectra of an EM-image: on left is shown a periodogram generation from a micrograph using the small overlapping windows method, while on right is shown usage of a particle stack obtained from a micrograph for generating an average power spectrum.



#### 2.2.4 2D Image Alignment and Classification

One of the important steps in single particle analysis is to identify the characteristic views of the protein complex and classify the images present in similar orientations. The different views of the protein are obtained from film or CCD images collected at the electron microscope. From these, the particle images representing the characteristic views of the protein are selected either manually or by using semi-automatic selection methods (Ludtke et al. 1999; Suloway et al. 2005; Woolford et al. 2007). The selected particle images are then stacked into a single file for further processing. The particle image stack is treated with a low-pass filter to reduce any background noise. The filtered particles are then centered w.r.t. to a circularly averaged reference image, which is generated from the stack of images present in the dataset. The filtered and centered particle images are then analyzed for the presence of characteristic views (Fig. 5). This is done by classification which is based on multivariate statistical analysis (van Heel 1984) (MSA) or similarity based measuring methods (van Heel 1987b; Frank 1990).

MSA is used to calculate the eigenvalues and eigen-images of a dataset, which can represent characteristic features, i.e. a fingerprint (van Heel 1984) of the dataset, where each image is a vector in a multidimensional space. This method is useful for initial unsupervised classification of a dataset, when no initial reference is available to align the images. As few eigenvalues are used to present the complete data, MSA helps in reducing the size and dimensionality of the data while preserving the most important features. This method might not be very efficient for certain data types which lack a characteristic distribution of the data cloud in hyper-dimensional image space (i.e. showing high inter-image variance) --an effect which is worsened for cryo-specimens with poor contrast.

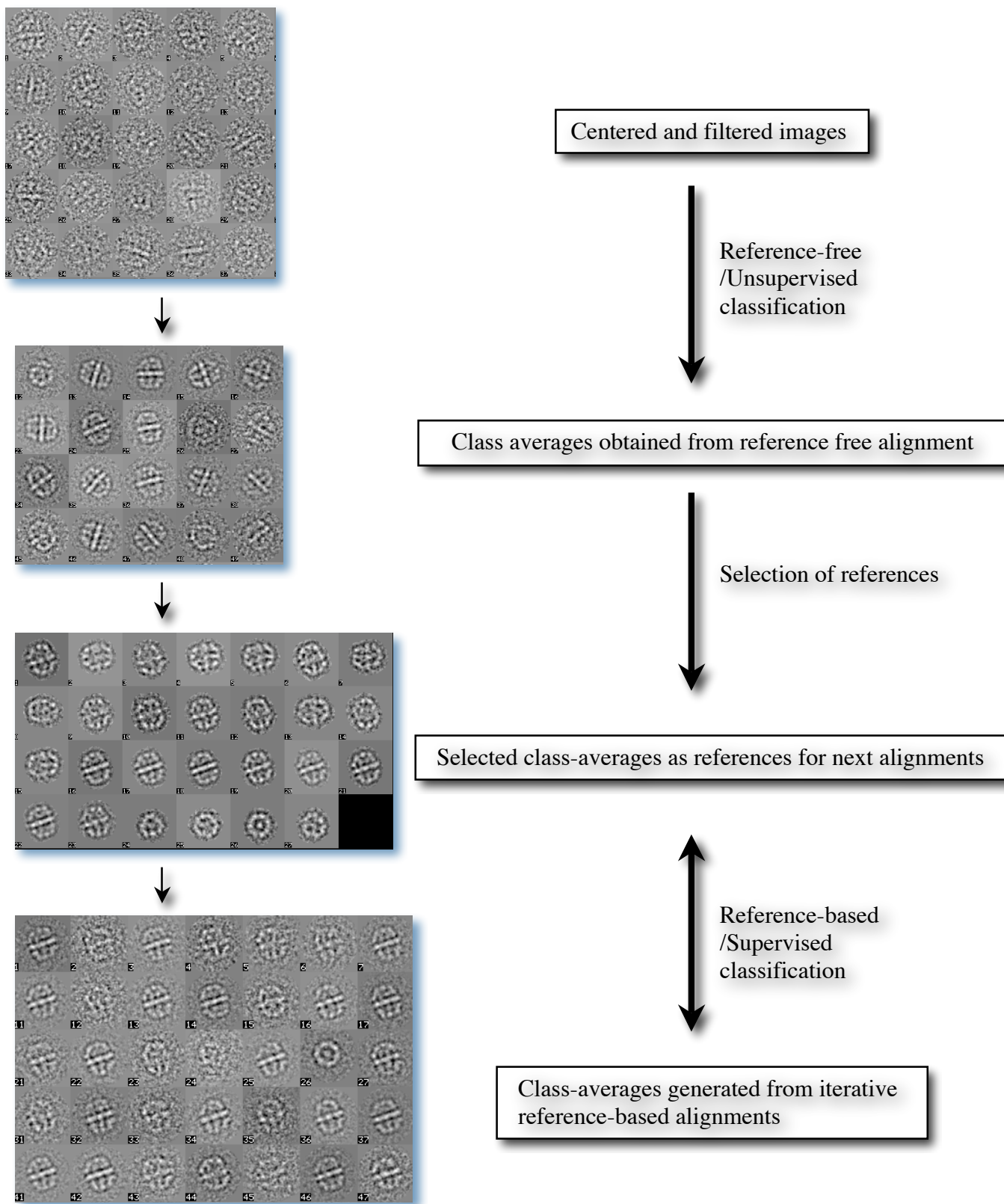
Other classification methods use a “similarity criterion” for dividing the data into several classes (van Heel 1987b). The basis for measuring similarity is usually intra-class variance, where the images are iteratively classified with other images of similar orientation in such a way as to have the least variance within a class and the highest inter-class variance. This can be achieved by assigning a value to the intra-class variance, based on which the images are divided hierarchically into increasing orders of classes,

such that the final number of classes is determined by the assigned value of the similarity criterion. As a result this method is also called “Hierarchical Ascendant Classification (HAC)” (van Heel 1987b; Frank 1990). Some other similarity measures used for classification of images are phase residuals, Fourier ring correlation and structure factors. Here, for a given set of two images, the difference between their phases (phase residual), correlation derived from their Fourier rings and similarity to the structure factor profile, obtained by the X-ray scattering curve of the particle, is used respectively for the classification of the two images in the same or different classes.

Another important feature of classification is that it can be either of “hard” or “fuzzy” types (van Heel 1987b; Frank 1990). In the former, each image is allowed to be only in one class, while the latter allows the image to be assigned to other, similar, classes but in each case is weighted according to the similarity measure. Both of these methods were applied for this data; the hard classification was used on the initial dataset, and the final refinements at very small angular increments used fuzzy classification. Here, the classes tend to look similar at small angular increments ( $1-3^\circ$ ), hence some images are allowed to contribute to more than one class, as angular assignment in this range can be inaccurate. Hard and fuzzy methods are typically used in tandem depending on the angular increment used in the alignment step during iterative processing.

After classification, the images present in each class are averaged to form a single representative of each class called “class-averages” (Fig. 3). Averaging of images leads to high SNR in the class-averages with a reduced background noise. Class-averages are used for further alignment of the data and 3D-reconstruction iteratively (Fig. 5), such that the accuracy in alignment parameters is improved in each iteration until convergence is reached.

**Figure 5.** Flow chart representing an outline for unsupervised and supervised classification in single particle analysis.





## 2.2.5 3D-Reconstruction Methods

### 2.2.5.1 Angular Reconstitution

This is a method (van Heel 1987a) used for 3D-reconstruction in single particle analysis which is based on the central section theorem --that every Fourier transform of a 2D-projection of a 3D-object passes through the center of the Fourier transform of that 3D-object at that particular angle. Thus, for any asymmetric structure, at least 3 different views are needed to reconstruct its approximate 3D-density (Fig. 6a). For any 2D-image when projected with an angular increment of  $1^\circ$  within a range of  $0-360^\circ$  angles to form an array of 1D line projections, this is known as a sinogram (van Heel 1987a). To find the angle of orientation between any two given 2D-projections, their sinograms are correlated using a sinogram correlation function to find the common 1D-line of projection between them (Fig. 6b). The angle between the common lines of two sinograms provide the in-plane angle between the images, while a third projection in a different plane is added to find the two out of plane angles between the three images. Similarly, more projections are added and their relative angles are calculated w.r.t each other. Hence this method is also called the “common lines” (Crowther et al. 1970) method and is used widely for generating an ab-initio model in single particle analysis. The limitation of this method is that the handedness of the protein cannot be absolutely determined, but handedness of helices in the case of high resolution ( $<5.4 \text{ \AA}$ ) maps or the fitting in of known X-ray structures can be used to assess it later. Another method of 3D-reconstruction which can determine the handedness of a protein is the random conical tilt method as described next.

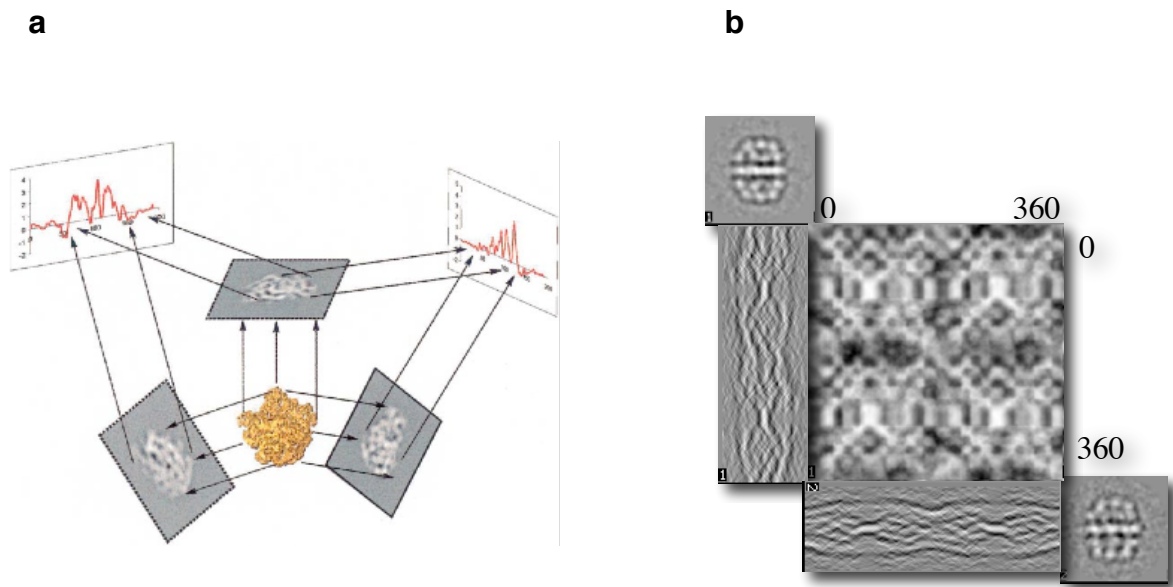


**Figure 6.** (a) Pictorial representation of angular reconstitution method (van Heel 1987a) showing that at least 3 views are needed for 3D-reconstruction of any asymmetric structure. (b) Sinogram correlation function for two different views of FAS.

### 2.2.5.2 Random Conical Tilt (RCT)

This is another commonly used method (Radermacher et al. 1987) for 3D-reconstruction in single particle analysis, used mostly for negative stain samples to generate an initial model. Here, the sample is imaged twice, once at a fixed tilt angle in the microscope and the other at zero tilt (Fig. 7). As the tilt direction is known from the microscope this method can provide the handedness of the model. The un-tilted images are used for determination of in-plane 2D-alignment parameters, which are then applied to the tilted images. The tilted dataset alone is then used to generate a 3D-volume. RCT is highly suitable for proteins with a preferred orientation on the grid and benefits greatly from the use of negative stain in order to improve alignments, though this leads to flattening and uneven staining artifacts as discussed earlier. Moreover, the tilted images are classified using the un-tilted images as references, which can result in ambiguities arising from the

fact that un-tilted images are obtained from the second exposure of electrons on a sample which might already be damaged due to electron dose.

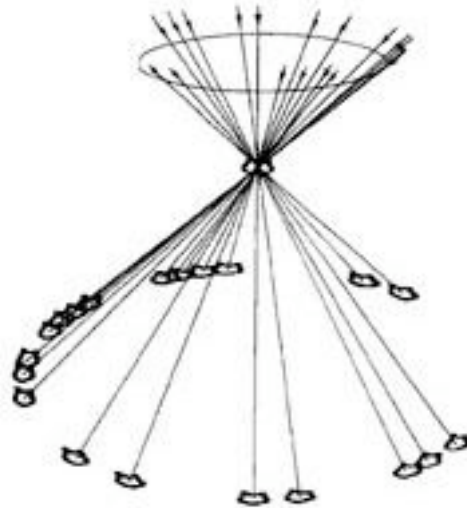


**Figure 7.** Principle of random conical tilt method, showing how many rotated images within a cone come together to form a surface (Radermacher et al. 1987).

### 2.2.5.3 Weighted Back Projection

The angular orientation of the images, also called Euler angles (alpha, beta and gamma) (Radermacher et al. 1987; van Heel 1987a), w.r.t each other are found by the methods described above. In order to generate a 3D-volume from a set of images the method called back-projection (van Heel 1987a) (Fig. 8a) is used, in which the 2D-projections are re-projected back along the direction of their projection in real space. Here, a back projection of an image corresponds to a plane in Fourier space orthogonal to its direction of projection.

In order to determine if a particular projection was assigned a correct set of Euler angles, it's corresponding re-projection obtained by the forward-projection of the 3D-volume is checked for similarity (Fig. 8b). This method is used in almost all the reconstruction software including IMAGIC (van Heel et al. 1996) and EMAN (Ludtke et al. 1999). The back projection method requires an even distribution of images (Fig. 9) to produce a high-resolution structure (Radermacher et al. 1987; van Heel 1987a). Preferred orientations of the particles, however lead to over-representation of some views and generate artifacts in the reconstruction. In addition, the low spatial frequencies are over-represented when back projecting through a central section, while the density of information at high spatial frequency is comparatively small due to widening of the angular gap (Frank 1996). A proper weighting function based on the angular distribution of the images is applied to rectify these errors, this is known as the "weighted back projection" method. Application of a filter function to the 2D-images before back-projecting helps in reducing noise-induced artifacts, hence generating a closer to original 3D-structure.

Other methods such as Fourier and algebraic methods are also used for 3D-reconstruction in single particles (Frank 1996), which use the same basic principle as discussed above except that they differ in the algorithmic formulation in addressing the same problem. Fourier methods (Grigorieff 2007) perform all the calculation in Fourier space, although they produce results similar to the real-space methods described above. Algebraic methods (Elmlund et al. 2008) are computationally intensive, as their solution space is

large and the algorithm needs several iterations to get the right values of unknown parameters.

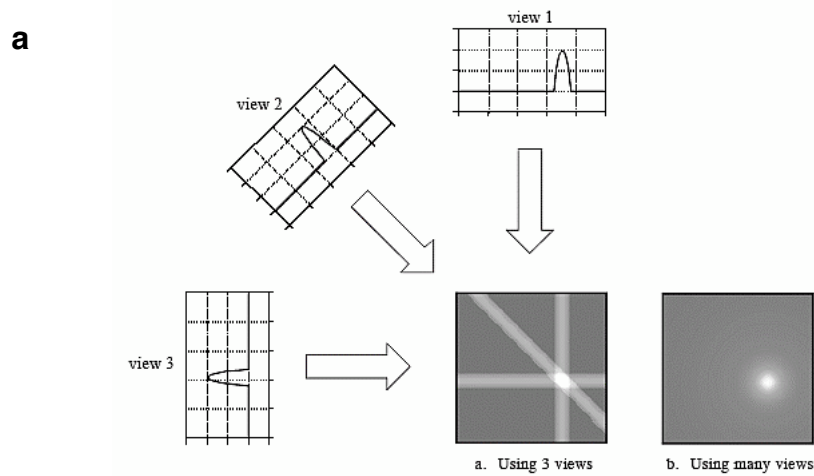


**Figure 8a.** Back projection reconstructs an image by taking each view (shown as 1D view 1, 2 & 3) and “smearing” it along its direction of projection. The resulting image shown as a 2D disc in (a) is a blurry version of the original image. When a sufficient number of views are used during back projection the object can be reconstructed more accurately as shown as a 2D disc in (b) (Smith 2002).

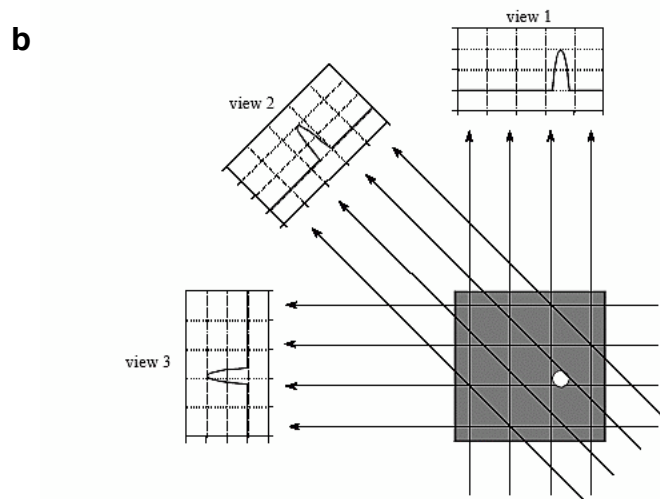


**Figure 8b.** Forward projection of the reconstructed image (shown as a 2D-disc here) in the direction of the original views (shown as 1D views here) produces its “re-projections”. A comparison between the original projection and its re-projection can be used to assess if the images were assigned correct angles during back-projection (Smith 2002).

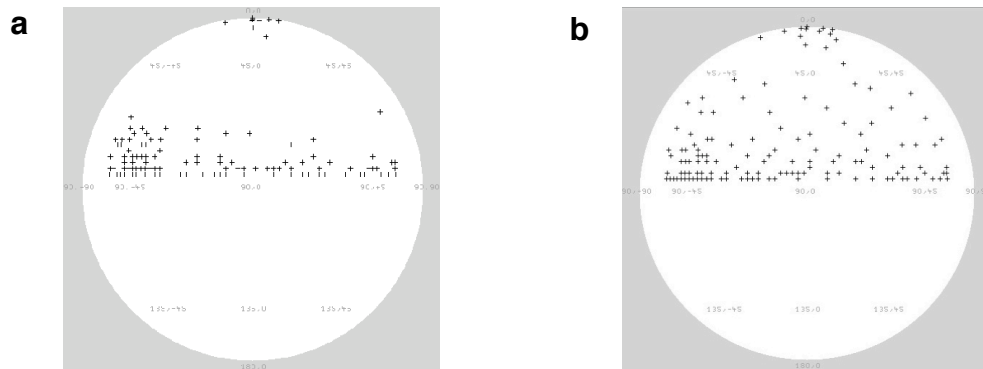


**Figure 9.** (a) & (b) represent the mapping of Euler angles on a sphere for a set of FAS particles, where the former shows an uneven distribution of views, while the latter represents a more evenly distributed set of views.

### 2.2.6 Resolution Assessment

The measure of resolution in single particle analysis is calculated by Fourier shell Correlation (van Heel 1987b) (FSC) between two independent 3D-reconstructions, which is plotted as correlation value between the two volumes at a spatial frequency along the x-axis. For this, data is divided into two halves, mostly by splitting the even and odd numbered images into two sets and performing a separate 3D-reconstruction for each dataset before calculating a Fourier-shell correlation between the maps. To assess a single value of resolution there exist several criteria to read the plot. One such example is based on choosing a correlation value, for instance  $FSC=0.5$  (Bottcher et al. 1997). At this value the SNR is equal to “1” and below this value SNR starts to fall, i.e.  $<1$  (Frank 1996). The FSC represents the real-space correlation between the two independent maps generated from half datasets, with resolution measured at  $FSC=0.5$ . This method, calculated from only half the data, is considered to be conservative as it underestimates the resolution of the full dataset. Later it was suggested in a study (Rosenthal and Henderson 2003) that if the two independent sets can be averaged to produce a map for the complete dataset, then a value of  $FSC=0.143$  would correspond to the resolution of

the complete dataset. This was derived by comparing the full dataset to an imagined, virtual, noise-free model, both represented strictly in terms of SNR, which was shown to be entirely represented in terms of the half dataset FSC (Rosenthal and Henderson 2003). This method has been used in near-atomic resolution studies by SPA (Sachse et al. 2007; Zhang et al. 2008; Zhou 2008), where the structural features in the EM-map are observed in good agreement with the corresponding X-ray structures of similar resolution. Other resolution assessment criteria interpret the resolution at a particular sigma level in the Fourier shell correlation plot generated from a half dataset such as the commonly used  $3\sigma$  criterion (van Heel 1987b). For the dataset in this study the Fourier shell correlation method (van Heel 1987b) using the 0.5 (Bottcher et al. 1997) and 0.143 (Rosenthal and Henderson 2003) criteria have been used for resolution assessment.

### **2.2.7 Map Analysis**

Further analysis of the EM-map is done by rigid body fitting of homologous or known structural domains if their structure is available from the same or a related organisms. An EM-map represents a continuous density distribution of a protein sample, so structures with varying flexibility are seen at different threshold levels. For this the EM-map is segmented based on grey-level histogram at different threshold levels to analyze different features. Both rigid-body fitting and map segmentation were applied for the analysis of the 3D-map presented here.

High resolution EM-maps can be used for the secondary structure prediction (Ludtke et al. 1999) and backbone tracing of proteins such as done in the case of the 6 Å cryo-EM map of GroEL (Ludtke et al. 2008). Recently computational algorithms based on an elastic deformation model (Schroder et al. 2007) have been developed which can generate an energy minimized backbone trace structure from low resolution EM-density maps. In the case of existing X-ray structures this method can also be used to study differences between the X-ray and the corresponding EM-maps (Schroder et al. 2007). Near atomic resolution EM-maps can now reveal side-chain arrangement in a protein structure as has been done in the studies involving icosahedral viruses (Zhang et al. 2008; Zhou 2008).

As previously mentioned in cryo-electron microscopy, freezing of the protein sample at near native conditions preserves the physiologically relevant structure of the protein in which different mobile and flexible domains can be trapped in different conformations. For the complete analysis of the information provided by an EM-map generated by the single particle method the estimation of the 3D-variance in the map is of importance to observe any mobile or flexible features. For this a bootstrap method (Penczek et al. 2006a; Penczek et al. 2006b) is used, where several hundred volumes are generated from a few randomly chosen images from a given dataset and a 3D-variance is calculated from the different volumes generated. This is then divided by the average structure to remove any error arising from the alignments. Such a 3D-variance map reveals any structural differences or heterogeneity in the dataset. For this study the bootstrap method has been used to study the mobile acyl carrier protein domain as discussed later in results.



## 2.3 Materials and methods

### 2.3.1 Negative stain

Yeast (*S. cerevisiae*) FAS synchronized by addition of NADPH, malonyl-CoA and inhibited by cerulenin was isolated and prepared by our collaborators in Martinsried as described (Johansson et al. 2008). The provided yeast FAS sample was first analyzed for purity and stability by negative staining. The protein sample was applied on a C-film (coated on a Cu-grid) with and stained with uranyl acetate and the stain was blot dried. The grid with stained sample was observed at low acceleration voltage electron microscopes: Philips CM120 or FEI Tecnai G2 Spirit both operating at 120kV.

### 2.3.2 Cryo-sample preparation

After the negative stain analysis, freezing in vitreous ice was used to preserve the yeast FAS sample at liquid N<sub>2</sub> temperature. For this, commercially available holey-C grids (Quantifoil MicroTools) were used, which were treated with chloroform to dissolve any plastic around the holes on the C-film. The grids were then made hydrophilic by glow-discharging, a way of depositing ions using a glow-discharge chamber. About 2.5-3µl of the sample was applied on the pre-treated holey-C grids and the extra sample was blotted off using Whatman IV filter paper. The grid containing the sample was vitrified by injection into liquid ethane using a Vitrobot plunge-freezing device (FEI). A second dataset, which was later collected for high resolution EM-map generation, was taken from the sample frozen using a home built plunge freezing device to produce thin-ice samples by manual control of the blotting conditions.

It is important to have the right humidity conditions while freezing the sample as it controls the amount of solvent left on the sample before vitrification --too high humidity can lead to thick ice formation in the sample, while low humidity can cause drying of the sample.

Table 1. Freezing conditions, where blue and green colors are for values corresponding to initial data and the second high-resolution dataset:

Freezing device	No. of Blots	Blot time (in seconds)	Humidity (in %)
Vitrobot	2	2-3	99
Plunge freezing device	1	4-5	~75

### 2.3.3 Electron cryo-microscopy

A first set of ~15,000 particle images was collected on a Tecnai G2 Polara electron microscope operating at 300 kV at a defocus range of 5-7  $\mu\text{m}$  and an electron dose of 10-12  $e^-/\text{\AA}^2$ . Images were recorded at a magnification of 39,000x on Kodak SO-163 film and scanned on a Zeiss Photoscan scanner (Intergraph) at a step size of 7  $\mu\text{m}$  on an 8-bit scale. Adjacent pixels were averaged to yield a step size of 3.59  $\text{\AA}$  at the specimen. An initial 3D reconstruction by angular reconstitution from the first dataset using ~9,000 particles was performed with IMAGIC V (van Heel et al. 1996) using C1 symmetry -- during later refinements the natural D3 symmetry present in the particles as known from the previous studies was applied (Kolodziej et al. 1996). An initial map was obtained at a resolution of 20  $\text{\AA}$  as measured by the 0.5 criterion (Bottcher et al. 1997).

To improve the resolution of the initial EM-map, a second set of ~25,000 particle images was collected with the same instrument at a lower acceleration voltage of 200 kV to improve contrast, allowing closer to focus data collection. A range of defocus between 1-3  $\mu\text{m}$  was used to compensate for the loss of information at zeroes in the contrast transfer function. A higher electron dose of 20-30  $e^-/\text{\AA}^2$  was applied to enhance contrast produced by electron-specimen interaction. To compensate for the drop in modulation transfer function (Frank 1996) of film at lower magnifications, the second dataset was collected at a value >50000x. An increase in magnification also provides a finer sampling in the images i.e., smaller pixel size, as a result the resolution of 3D-reconstruction becomes less sensitive to 2D-alignment errors. Images in the second dataset were recorded at a nominal magnification of 59,000x on Kodak SO-163 film and scanned as above on a 16-

bit scale with a step size of 1.19 Å at the specimen. A 16-bit scale instead of 8-bit scale was used to improve the dynamic range in the grey scale of the images in the new dataset.

*Table 2. Imaging conditions, where the color scheme is the same as used in Table 1:*

<b>Acceleration Voltage (in kV)</b>	<b>Defocus (in <math>\mu\text{m}</math>)</b>	<b>Electron dose (in <math>\text{e}^-/\text{\AA}^2</math>)</b>	<b>Magnification</b>	<b>Scanner dynamic range (in bits)</b>	<b>Final pixel size (in <math>\text{\AA}</math>)</b>	<b>No. of particles used in final 3D-reconstruction</b>
300	5-8	10-12	39000	8	3.59	9000
200	1-3	25-30	59000	16	1.19	19000

#### **2.3.4 X-ray solution scattering**

X-ray solution scattering experiments were conducted at the Swiss Light Source (SLS) beamline X12SA. FAS samples at concentrations of 10 mg/ml and 2 mg/ml were measured at two detector lengths. The data were background-subtracted using buffer blanks and corrected using established procedures. Data from both length scales were combined into a single scattering profile covering the range from 300 Å to 4 Å resolution.

#### **2.3.5 Data processing**

Particles were selected using the semiautomatic mode of the BOXER module from EMAN (Ludtke et al. 1999). The images were aligned and classified using MSA and HAC classification methods in IMAGIC (van Heel et al. 1996). An initial 3D reconstruction by angular reconstitution from the first dataset using ~9,000 particles was performed using IMAGIC V (van Heel et al. 1996). The resolution of the initial model was determined by Fourier shell correlation to be 20 Å by the 0.5 criterion (Bottcher et al. 1997).

From the second dataset ~25000 particles were picked using the semiautomatic mode of the BOXER module from EMAN (Ludtke et al. 1999). The phase reversals in the images

caused by the Contrast Transfer Function (CTF) were corrected by phase flipping and the amplitudes were corrected using the low angle X-ray solution scattering data. The images were classified and averaged using the structure factor of the FAS particle as a “similarity criterion” (Ludtke et al. 1999). To determine accurate 2D-alignments parameters Wiener filtered (Frank 1996) images were used and the calculated parameters were then applied to the corresponding non-filtered images. An initial 3D reconstruction was obtained with EMAN1 (Ludtke et al. 1999) from ~19,000 particles. The map was initially projected at an angular increment of 8° to generate references to align the 2D-projections which produced a 3D-map at ~11 Å resolution.

### **2.3.6 Resolution Assessment**

The resolution of the final map was determined by splitting the data into two halves of odd and even numbered images by using the eotest module in EMAN1 (Ludtke et al. 1999). Two independent 3D-reconstructions were performed from the split datasets, for which a Fourier shell correlation (FSC) plot was generated. The FSC plot was interpreted using the 0.5 criterion (Bottcher et al. 1997) and the 0.143 criterion (Rosenthal and Henderson 2003). A careful visual inspection of the map for resolvable structural features (e.g. alpha-helices, beta-sheets etc.) was performed by fitting in the yeast FAS X-ray structure (Johansson et al. 2008).

### **2.3.7 Estimate of 3D-variance**

A 3D-variance map was generated in EMAN1 (Ludtke et al. 1999) from 100 volumes generated from the high-resolution dataset using a randomset of ~18,000 particles out of the total ~19000 particles by the bootstrap technique (Penczek et al. 2006a; Penczek et al. 2006b) using the calculateMapVariance.py routine in EMAN1 (Ludtke et al. 1999). The resultant 3D variance map was divided by the average structure to remove any variance arising from structural alignment errors.

### **2.3.8 Map visualization and analysis**

Molecular graphics images were produced using the UCSF Chimera package from the Resource for Biocomputing, Visualization, and Informatics at the University of California, San Francisco (supported by NIH P41 RR-01081) (Pettersen et al. 2004).

Automatic fitting of the enzymatic domains from the yeast FAS structure (2VKZ) (Johansson et al. 2008) and the PPT domain (2WAS) (Johansson et al. 2009) was done in Chimera. The atomic model of ACP was fit into the corresponding EM-densities near the KS, KR, ER and AT domains by rigid body fits in Chimera; all were highly similar in shape and gross features, though densities near the KR, ER and AT domains exhibited higher variability. The fit of the ACP near the KS-domain was performed automatically. Automated fitting into ACP densities near the other three catalytic domains was only possible for gross features, and finer adjustments were applied manually.

For the electrostatic calculations pdb2pqr (Dolinsky et al. 2004) was used to generate pqr-format files which were then used in APBS calculations performed using the VMD software package (Humphrey et al. 1996). Secondary structure predictions were performed with the PHYRE server (<http://www.sbg.bio.ic.ac.uk/phyre>) (Kelley and Sternberg 2009).

## CHAPTER 3

### RESULTS

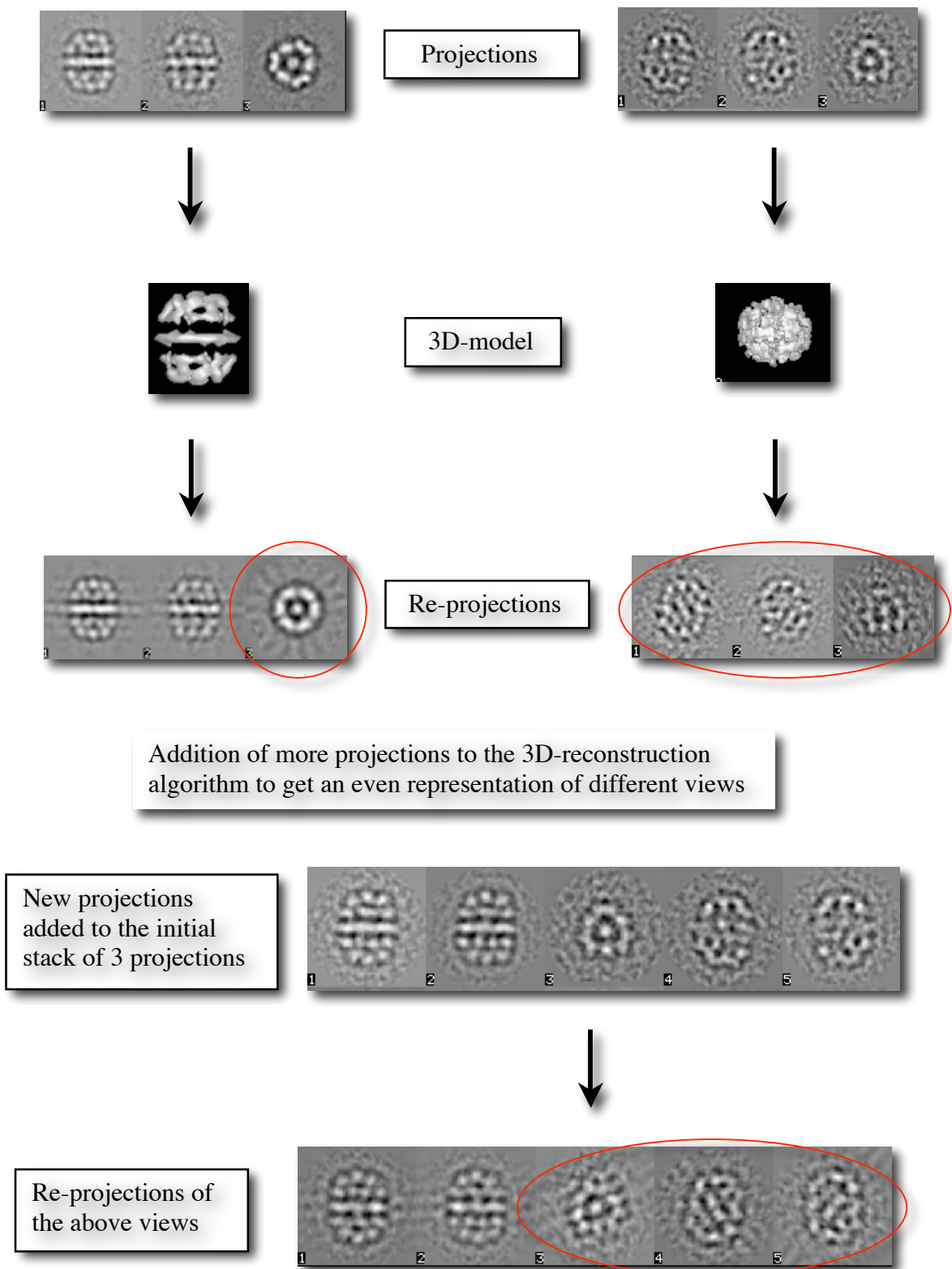
#### 3.1 Initial 3D-map

The initial cryo-EM data was generated from a dataset of ~15,000 particles. The CTF correction was performed by flipping of phases for which the defocus values were obtained from the micrographs using the “periodogram” method as described earlier. The CTF-corrected particles were treated with a circular mask and a band-pass filter before subjecting to 2D-alignments. The pre-treated particles were centered w.r.t. to a circularly averaged reference generated from the total number of particles present in the data. These centered particles were used in a reference free MSA classification to identify the characteristic views present in the data. The class-averages representing the characteristic views of the data were selected as references for classifying the particles present in similar orientations under the same class. Several iterations of alignments were performed until a convergence in classification of particles was obtained. From the resulting class-averages of the final iteration several representative views were used to generate an initial model.

For this study no initial reference model was used to generate an initial volume of yeast FAS. To obtain an ab initio 3D-map of FAS the method of angular reconstitution (van Heel 1987a) was applied. As discussed previously this method requires at least three different views of an object to reconstruct its 3D-structure. For this, three different views (Fig.1) represented by class-averages in the dataset of FAS particles were selected to generate a 3D-volume. To assign Euler angles to the 3-views initially a random set of Euler angles were assigned to back project to obtain a C1 symmetry map. The 3D-volume was forward projected along the direction of projection i.e., the assigned angles to the views to generate re-projections. These re-projections were compared with their original projections for similarity, as any difference between them would reflect incorrect Euler angle assignment to the original views in the 3D-map. Once accurate Euler angles

were assigned to the initial three-views, new projections were added to the 3D-reconstruction algorithm and the above method of “projection-matching” was used to assess the accuracy of the assigned Euler angles (Fig.1).

**Figure 1.** Flow chart for *ab initio* model building using the angular reconstitution approach: the projections assigned with wrong Euler angles does not match its re-projection (encircled in red).





In later iterations of 3D-reconstruction, D3 symmetry was applied to the data as known from literature (Kolodziej et al. 1996), the class-averages and maps obtained from the C1 reconstructions as well revealed a D3-symmetry present in FAS. An initial 3D-map (Fig. 2) at 18 Å from ~9000 particles was generated after several (~17) iterations of the angular reconstitution method. Johansson et al., in Martinsried, used the FAS map for solving the X-ray structure of cerulenin-inhibited FAS.

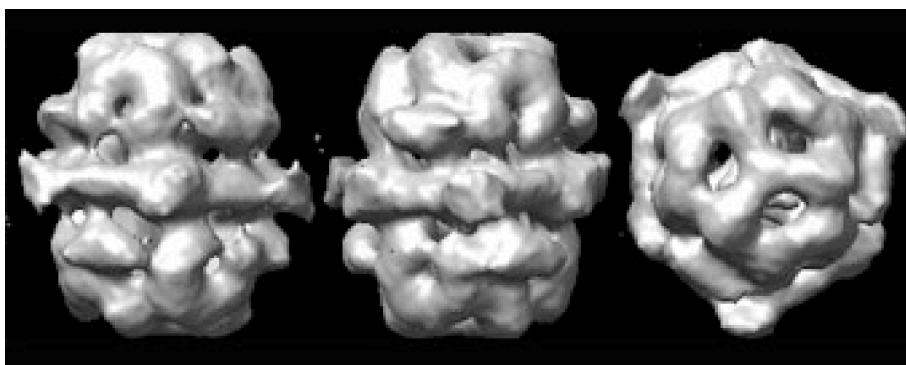


**Figure 2a.** Views of the initial 3D-model (D3 symmetry) of yeast FAS at 18 Å showing two side views along the two-fold axes and a top view along the 3-fold axis of the barrel.

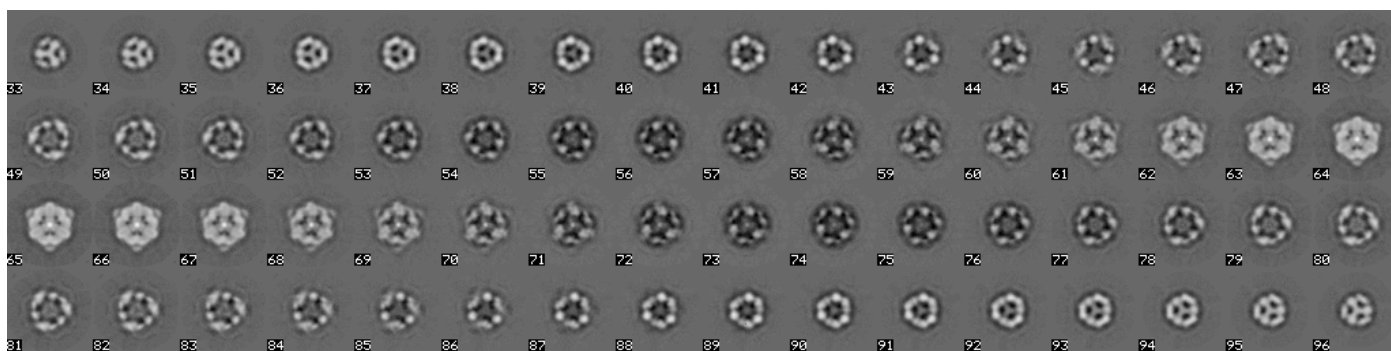


**Figure 2b.** Slices (3.6 Å thick) of the initial 3D-volume parallel to the equator.

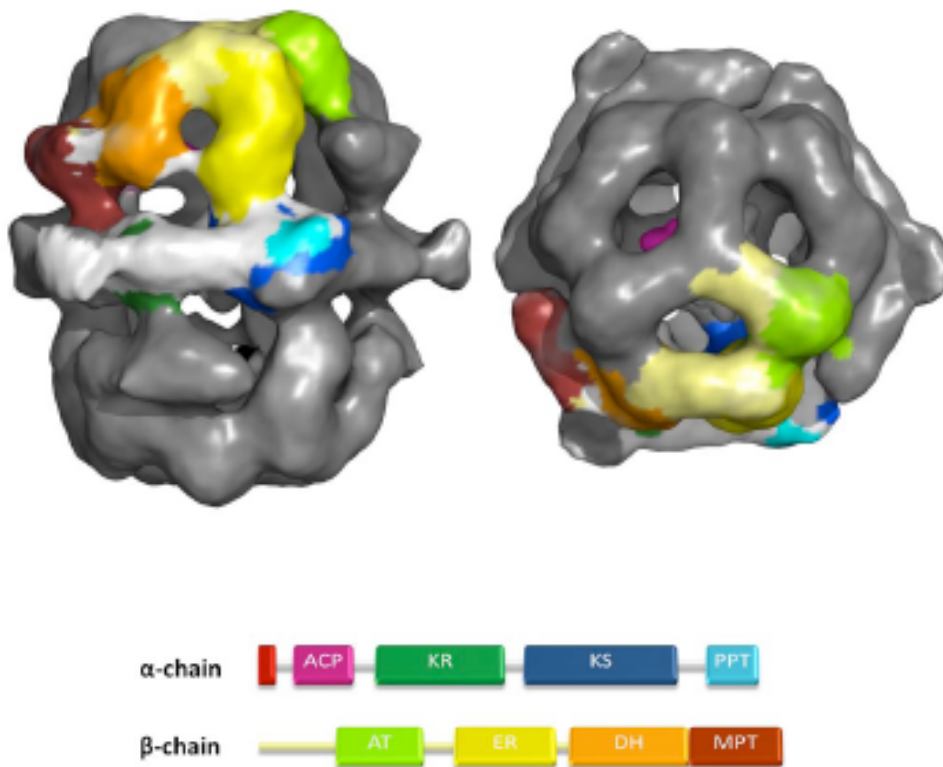


*Figure 2c: Initial model showing one reaction chamber of yeast FAS at 18 Å as seen in a side view and down the 3-fold axis. The color scheme represents different domains contributed by  $\alpha$  and  $\beta$ -chains in one reaction chamber (Johansson et al. 2008).*

The recently available X-ray structure of yeast FAS was fit into the EM-map for analysis, which revealed a good overall fit of the structure. In the X-ray structure, the ACP domain was seen stalled at equator near the KS-domain, while in the EM-map no corresponding density was observed at the equator, but rather density was observed above the equator inside the barrel in both domes (Fig. 4). As no other domain is expected to be present inside the barrel except the ACP, this density might correspond to an averaged density of the ACP domain, although at such low resolutions it is difficult to interpret such densities.

As previously mentioned, in cryo-electron microscopy, freezing of the protein sample at near native conditions can trap different mobile and flexible domains in different conformations. To obtain the mobile ACP domain trapped in different conformations inside the reaction chambers it was important to further improve the resolution of the EM-map for better estimation of the 3D-variance in the map for tracing the mobility of the ACP domain inside the FAS barrel. To improve the resolution of the EM-map, a second dataset at high resolution was collected as described next.

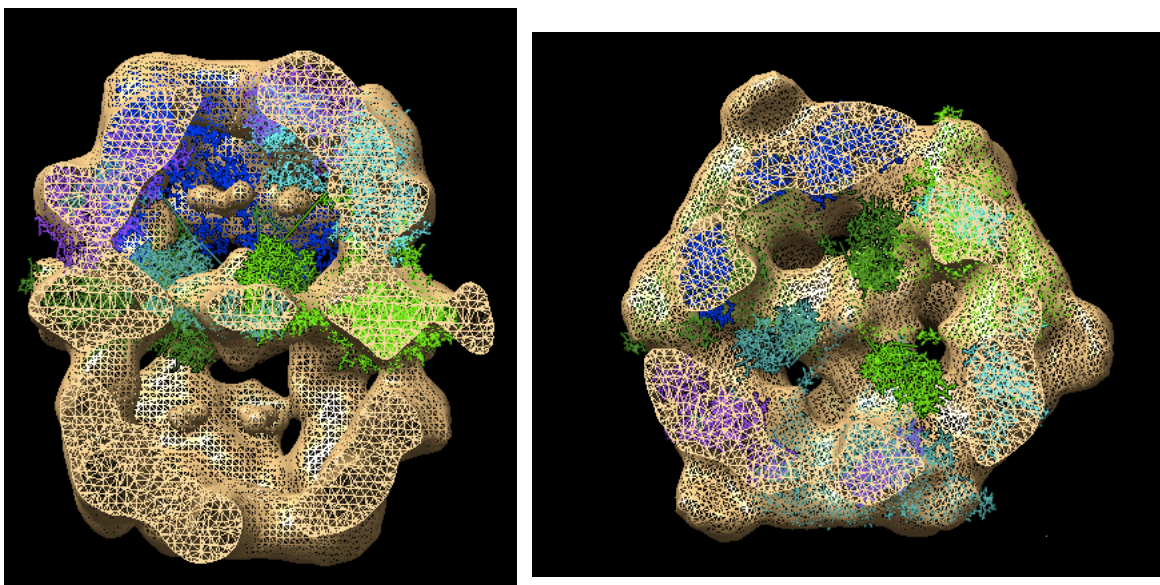


*Figure 3: Fitting of yeast FAS X-ray structure (Leibundgut et al. 2007) into the initial EM-map (shown for one dome).*

### 3.2 High Resolution 3D-map

A second dataset of ~25,000 particles was collected to improve the resolution of the EM-map. A contrast enhancement in the new images was attained by using a lower acceleration voltage at the EM (200 kV), along with a higher electron dose (20-30  $e^-/\text{\AA}^2$ ), which enabled closer to focus data collection. The loss of information at zeroes in the contrast transfer function was compensated for using a range of defocus values (1-3  $\mu\text{m}$ ). The modulation transfer function (Frank 1996) of film drops at lower magnifications and for this reason a higher magnification (>50000x) was used. An increase in magnification also provides a finer sampling in the images (i.e. smaller pixel size). As a result, the resolution of 3D-reconstruction becomes less sensitive to 2D-alignment errors. The pixel size of the second dataset was 1.19  $\text{\AA}$  as compared to 3.59  $\text{\AA}$  of the initial data.

The above improvements led to the attainment of high resolution in the second dataset, which exhibited a high SNR and could be seen at closer to focus conditions (Fig. 4). The particles picked from these high SNR micrographs showed signal even at sub-nanometer resolution (Fig. 5a).

Phase reversals caused by the contrast transfer function (CTF) were corrected by phase flipping (Ludtke et al. 1999). The phase-flipped images were used to generate a 3D-map, during the initial iterations the map was projected at an angular increment of  $8^\circ$  to generate references to align the 2D-projections which produced a 3D-map at  $\sim 11 \text{\AA}$  resolution. In subsequent iterations to improve the resolution further, the map was projected at smaller angular increments  $< 8^\circ$  --an angular step size of  $2^\circ$  generated a 3D-map at  $\sim 6 \text{\AA}$  resolution. Further decrease in angular step size lead to no further improvement in the resolution of the EM-map. The B-factors as calculated from the small angle X-ray solution scattering data were applied in final iterations. Automated refinements were performed at the GWDG UNIX computer cluster, where 40 years of CPU time was used.

A refined 3D map of yeast FAS from ~19,000 high-resolution images was generated. This subset of particles, obtained from the original dataset of ~25000, was selected using

a variance based similarity measure applied by the dfilt option in EMAN. The amplitudes correction was applied on the 3D-map during the final iterations by using the low angle X-ray solution scattering data. The resolution of the 3D-map was 7.2 Å as measured by Fourier shell correlation method (van Heel 1987b) of half datasets using the 0.5 criterion (Bottcher et al. 1997) and 5.9 Å when extrapolated to the full dataset (Rosenthal and Henderson 2003) (Fig. 5b). Careful inspection suggests that the map resolution is indeed close to 6 Å, as it is possible to distinguish  $\beta$  sheets in the protein domains and the helix pitch in some  $\alpha$ -helices (Fig. 8).

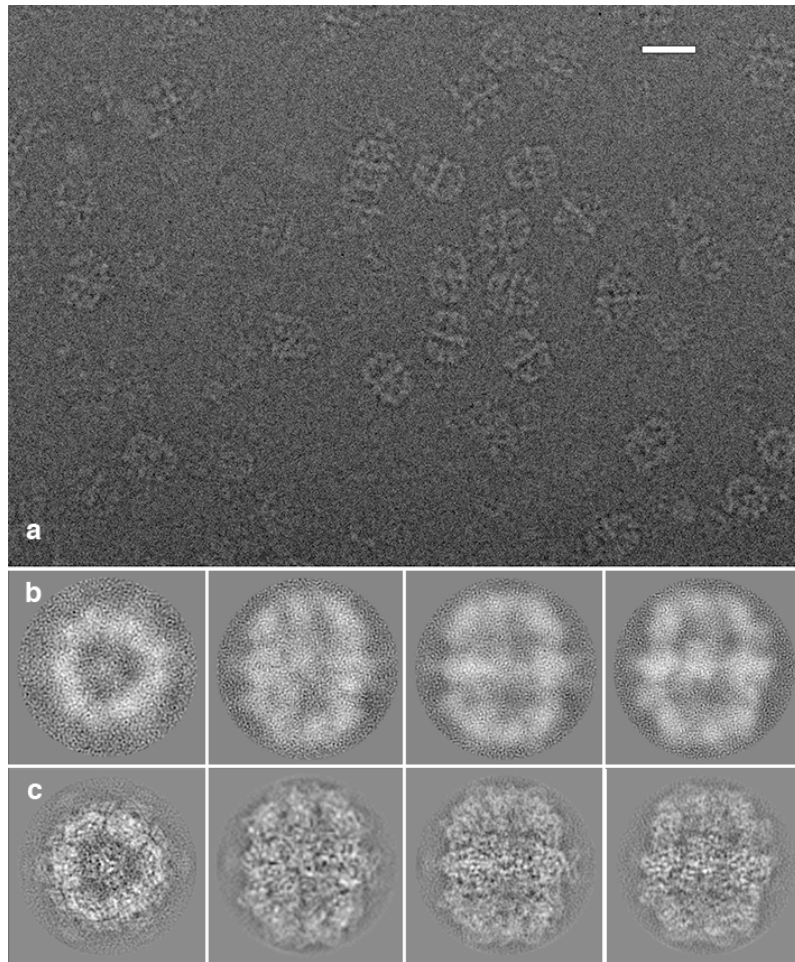


**Figure 4.** Image data. (a) Electron micrograph showing different orientations of FAS particles in vitreous ice at 1.5  $\mu\text{m}$  defocus (scale bar, 260  $\text{\AA}$ ). (b) Representative class averages of characteristic top and side views with (c) corresponding map re-projections.

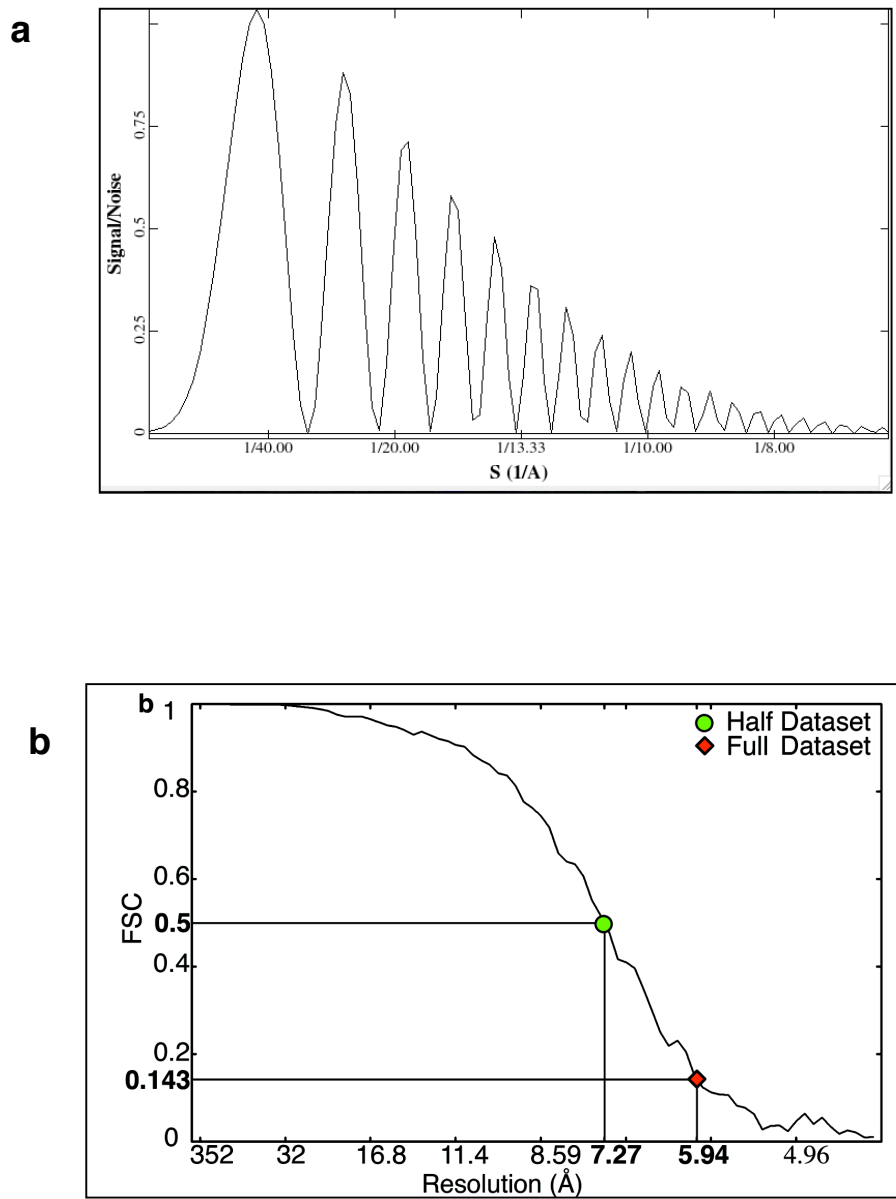


**Figure 5.** (a) SNR plot of an image from the second dataset showing signal at sub-nanometer resolutions generated using CTFIT in EMAN (Ludtke et al. 1999). (b) Fourier shell correlation plot indicating map resolution at 0.5 cut-off, comparing half datasets (Bottcher et al. 1997) (7.2 Å; green) and the full dataset (Rosenthal and Henderson 2003) at 0.143 cut-off (5.9 Å; red)

The decay in amplitudes, i.e. dampening of the CTF at high spatial frequencies due to the envelope function of the microscope, was restored by applying the amplitudes obtained from the low angle X-ray solution scattering data of FAS particles (Fig. 6). As mentioned earlier, the CTF envelope function of an EM leads to dampening of the amplitudes, which increases towards higher resolution. In order to retrieve down-weighted amplitudes and determine the B-factors the FAS scattering curve was used. In this way a complete CTF correction was performed for the final reconstruction.

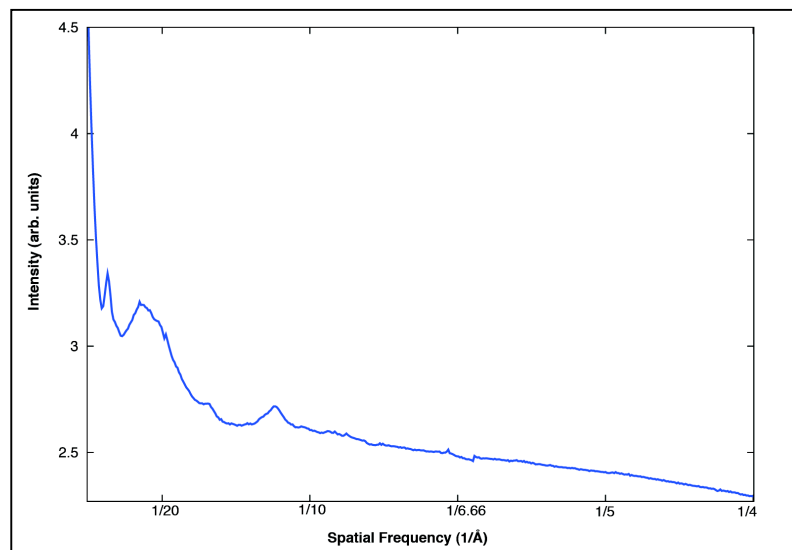


**Figure 6.** X-ray solution scattering curve for yeast FAS representing a 3D-rotationally averaged, normalized, intensity (Y-axis) at different spatial frequencies (X-axis). The scattering profile was applied to restore amplitude decay caused by the CTF-envelope in EM-images



### 3.3 3D-map analysis at 5.9 Å

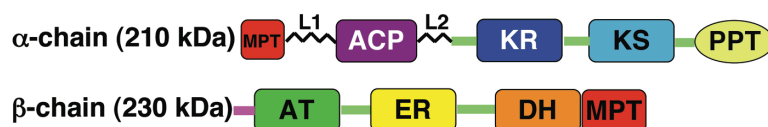


**Figure 7.** Diagrammatic representation of one  $\alpha$ - and  $\beta$ -polypeptide chain in fungal FAS representing the color scheme used for different domains in the subsequent figures.

The cryo-EM map of yeast FAS clearly resolves all structural features (Fig. 7) as seen in the four X-ray structures (Jenni et al. 2007; Leibundgut et al. 2007; Lomakin et al. 2007; Johansson et al. 2008). Rigid body fitting of the atomic model of yeast FAS (Jenni et al. 2007; Leibundgut et al. 2007; Lomakin et al. 2007; Johansson et al. 2008) into the EM-map was performed in order to analyze the map. The final pixel size of the map was recalibrated to 1.14 Å to attain a good automatic fit as judged by the EM-density correlation factor (Pettersen et al. 2004).

The analysis of map details (Fig. 8, 9) shows that the EM-map clearly resolves all the  $\alpha$ -helices and  $\beta$ -sheets present in the different catalytic domains of yeast FAS. The helix-pitch can as well be observed in the  $\alpha$ -helices present in the structural and catalytic domains at the equatorial wheel (Fig. 8e, f). The map reveals a clear density for the isoalloxazine ring of FMN present in the ER domain (Fig. 10). While a perfect fit was observed between the EM-map and the X-ray structure at the equator (Fig. 8c, d), there were significant differences observed in the catalytic domains forming the barrel-wall. The observed differences in the two structures were further analyzed by performing the automated rigid body fits of the atomic models of the individual catalytic domains of yeast FAS into the corresponding EM-density. Remodeled structures of the individual catalytic domains were generated based on the results obtained from their rigid body fits into the corresponding EM-densities. The observed differences between the yeast FAS X-ray structure and the EM-map are discussed in the next sections along with the other new features of interest observed in the map.

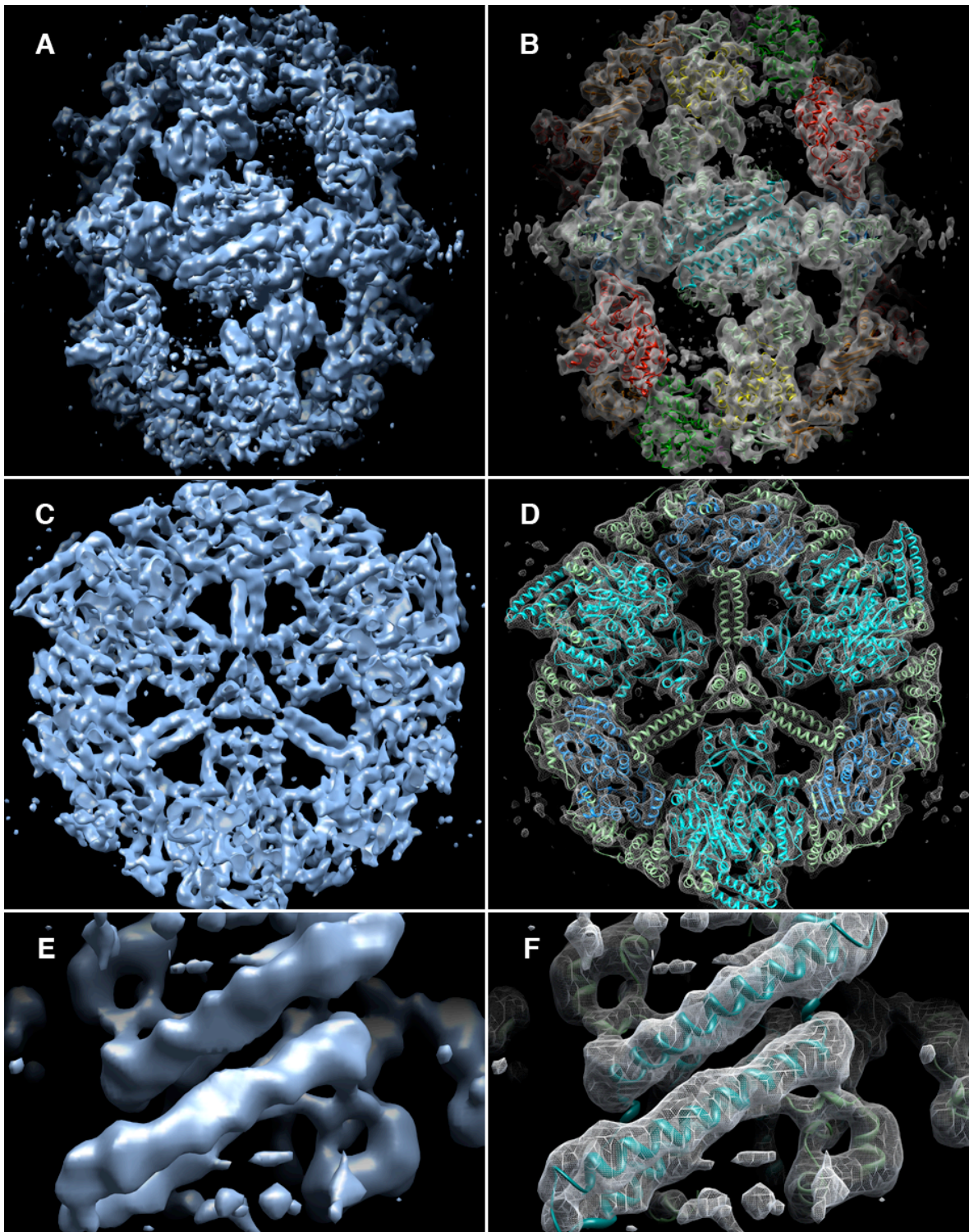


**Figure 8.** 3D map of yeast FAS at 5.9 Å resolution, without and with the domains of the X-ray structure (pdb 2VKZ) (Johansson et al. 2008) fitted as rigid bodies. The domains are colored as per the color scheme shown in Fig. 8; (a, b) Side view of the  $\alpha_6\beta_6$  assembly. (c, d) Central map section showing the  $\alpha_6$  wheel. (e, f) The helix pair near the KS dimer on the outside of the  $\alpha_6$  wheel showing the helix pitch.

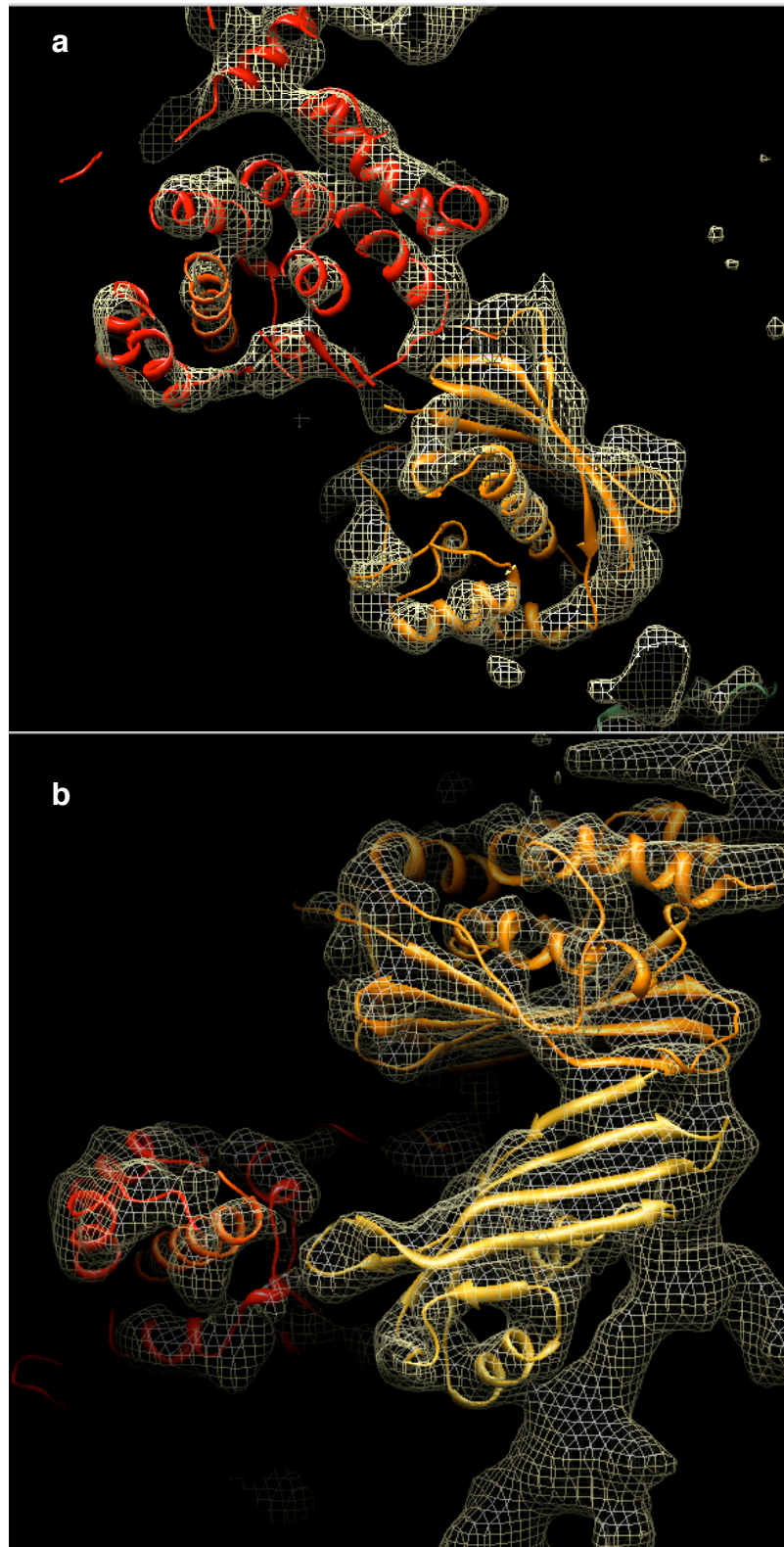


**Figure 9.** Details of the EM map with fitted structure (a, b) The MPT domain (red), which is mainly  $\alpha$ -helical, and the DH domain (orange), which is rich in  $\beta$ -sheets, shown in two different views.

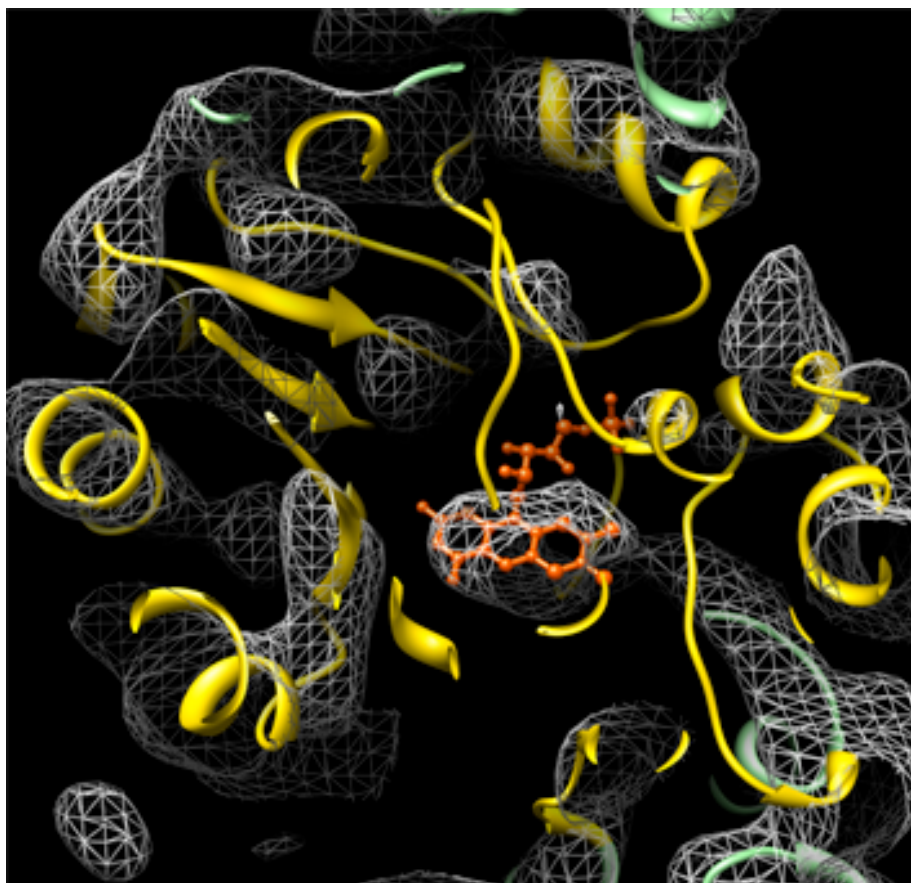


*Figure 10. Clear density is visible for the FMN cofactor (orange) in the ER domain (yellow).*

### 3.4 Structure of the $\alpha_6$ wheel

In the equatorial wheel of the FAS complex, consisting of the six  $\alpha$ -chains, all secondary structure elements from the X-ray models match the corresponding densities closely (Fig. 4d). In the three X-ray structures of *S. cerevisiae* FAS (Leibundgut et al. 2007; Lomakin et al. 2007; Johansson et al. 2008), the  $\alpha_6$  wheel is incomplete, as a part of the  $\alpha$ -chain near the KR dimer contact is missing, and the PPT domain is not resolved in two of the three structures. The *T. lanuginosus* structure (Jenni et al. 2007) shows a four-helix bundle on the outside of the KR dimer, with the helices tilted by  $\sim 45^\circ$  relative to the long axis of the complex, which is not seen in the yeast X-ray structures. The EM map density instead indicates a different structure of this part of the  $\alpha$  chain (Fig. 11a).

In one of the yeast FAS structures (Lomakin et al. 2007; Johansson et al. 2009), the PPT domain was found on the outside of the barrel near the KS dimer. A four-helix bundle on the outside of the equatorial  $\alpha_6$  wheel, which is part of the KS domain, separates two PPT domains, which are related by two-fold symmetry. This four-helix bundle is resolved in all X-ray structures and its density in the EM map is clear (Fig. 5a,b), although it has moved outward by  $\sim 2$  Å. The density of the PPT domain in our 6 Å map is comparatively weak, but the recently solved X-ray structure of the individually expressed yeast PPT domain (2WAS) (Johansson et al. 2009) superimposes well (Fig. 11b). With the PPT domain traced and the missing part of the KS domain visualized, the EM map of the yeast FAS complex shows the complete structure of the  $\alpha_6$  wheel.

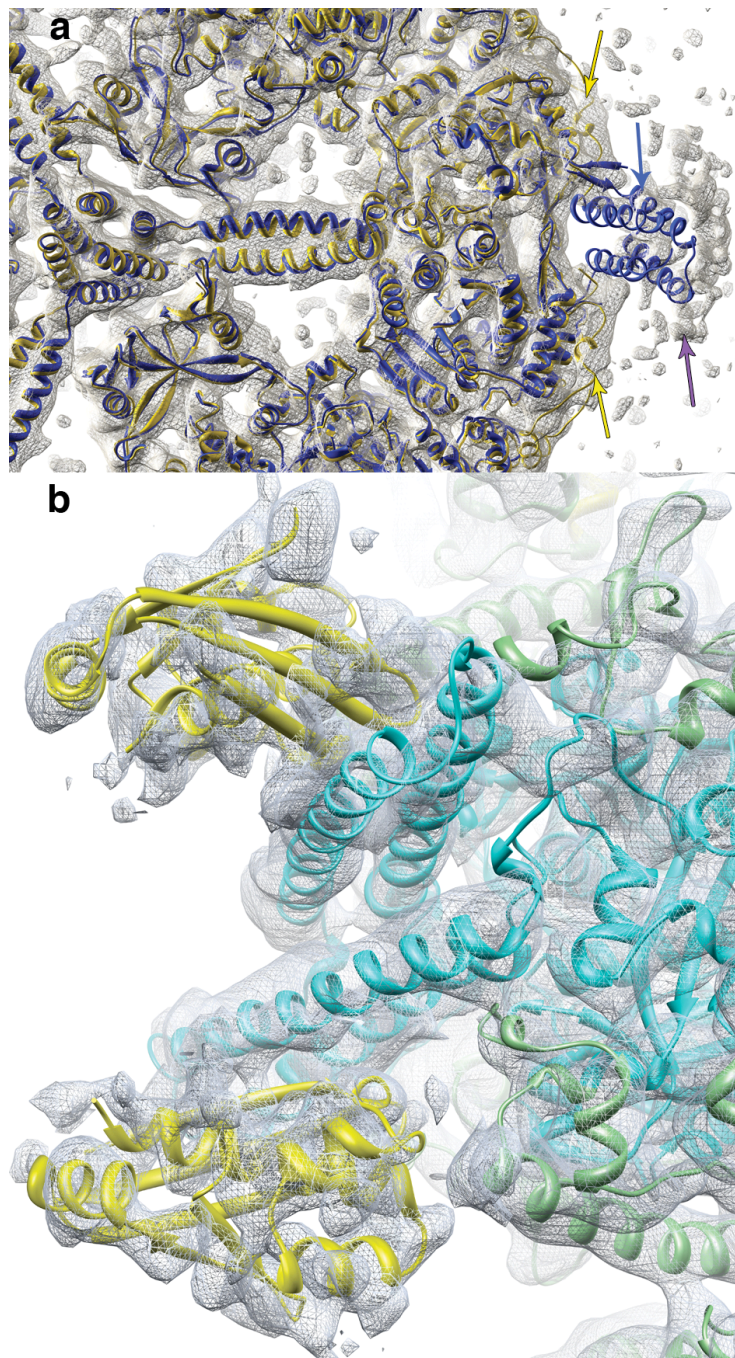


**Figure 11.** Complete structure of  $\alpha_6$  wheel. (a) Differences between yeast (yellow, 2VKZ)<sup>17</sup> and Thermomyces FAS (blue, 2UV9) (Jenni et al. 2007); yellow arrows indicate EM density and structure of the yeast model not present in Thermomyces FAS. Blue arrow indicates the position of the KR four-helix bundle as seen in the Thermomyces X-ray structure, the purple arrow points at the corresponding density in the EM map. (b) Fit of the PPT domain (gold) (2WAS) (Johansson et al. 2009) to the EM density at the KS dimer (cyan). The density is shown at  $1.5\sigma$  isosurface threshold.

### 3.5 Different organization of the reaction chamber wall

In contrast to the  $\alpha_6$  wheel, the global fit of the  $\beta_3$  domes reveals major differences in the position and orientation of the protein domains forming the barrel wall. We remodeled the X-ray structure of yeast FAS by rigid body fits of individual domains into the EM map density (Fig. 12). A significant radial displacement of the MPT domain is evident (Fig. 12.1). This domain includes a distinct  $\alpha$ -helical hairpin loop protruding into the solvent, which is shifted by more than one helix diameter towards the center of the barrel in the X-ray structures (Fig. 12.1b). While the contact to the KR domain in the equatorial wheel is preserved, the MPT domain rotates  $\sim 20^\circ$ , resulting in a 9 Å shift. A smaller displacement of  $\sim 5$  Å in the same direction is observed for the adjacent DH domain (Fig. 12.2a).

The ER domain has a TIM barrel fold and contains flavin mononucleotide (FMN) as a cofactor. Density for the isoalloxazine ring of FMN is clearly visible in the EM map (Fig. 10). While the global fit of the X-ray model for this domain was close, it appears to be shifted inwards in the EM map by  $\sim 3$  Å (Fig. 13), unlike the MPT or DH domains. The AT domain near the top of the barrel was likewise refitted by a  $\sim 9^\circ$  rotation in a plane parallel to the equator (Fig. 7c,d).

Some of the most striking differences between the EM map and the X-ray models are seen in the structural domain at the apex of the dome around the threefold axis. While the contact to the contiguous AT domain is unaffected, the structural domain is shifted by  $\sim 10$  Å downwards, and by a similar distance laterally, relative to the threefold axis, so that the helix closest to this axis moves by  $\sim 15$  Å (Fig. 12.2b). As a result, the molecular contacts between the three  $\beta$ -subunits are entirely different in the EM map compared to the X-ray structures (Fig. 13a).

The refitted EM model indicates a lever-like movement of the  $\beta$ -chain that forms the barrel wall around a pivot point at the MPT domain near its connection to the equatorial wheel. This results in an outward displacement of the domains near the  $\alpha_6$  wheel, and an

inward and downward movement of the upper domains. Overall, the FAS barrel is shorter by  $\sim 20$  Å and the dome is wider by up to 18 Å in the EM structure (Fig. 13b; **movie 1**).

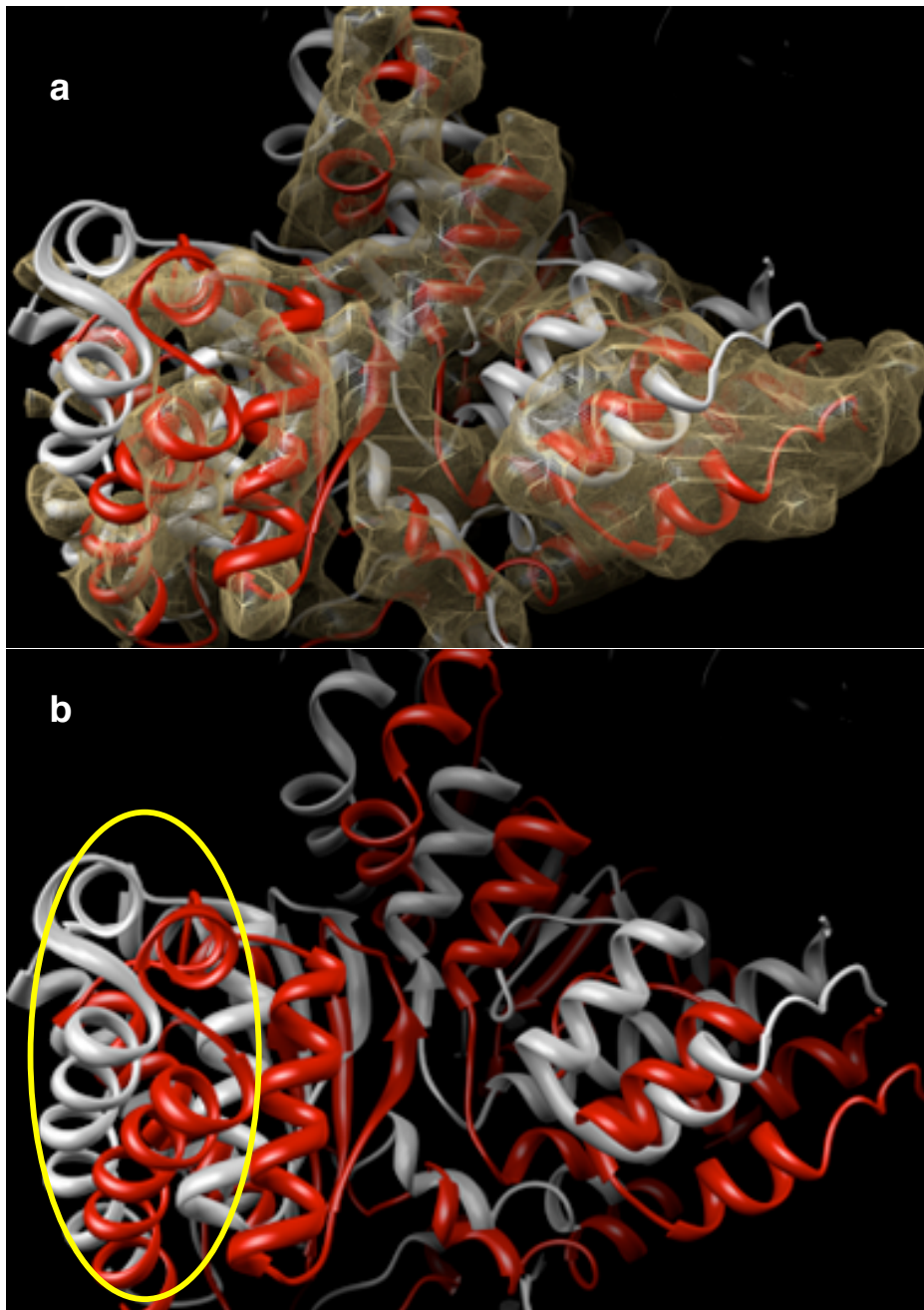


**Figure 12.1.** Differences between the yeast FAS structure fitted to the EM map and the X-ray structure (2VKZ) (Johansson *et al.* 2008). Fitted domains are colored according to figure 8, while the corresponding X-ray structure is white. (a) Remodeling of the MPT domain in the EM map density. (b) The MPT domain is displaced by  $\sim 10$  Å in the crystal structure. The  $\alpha$ -helical hairpin loop protruding into the solvent is encircled in yellow.



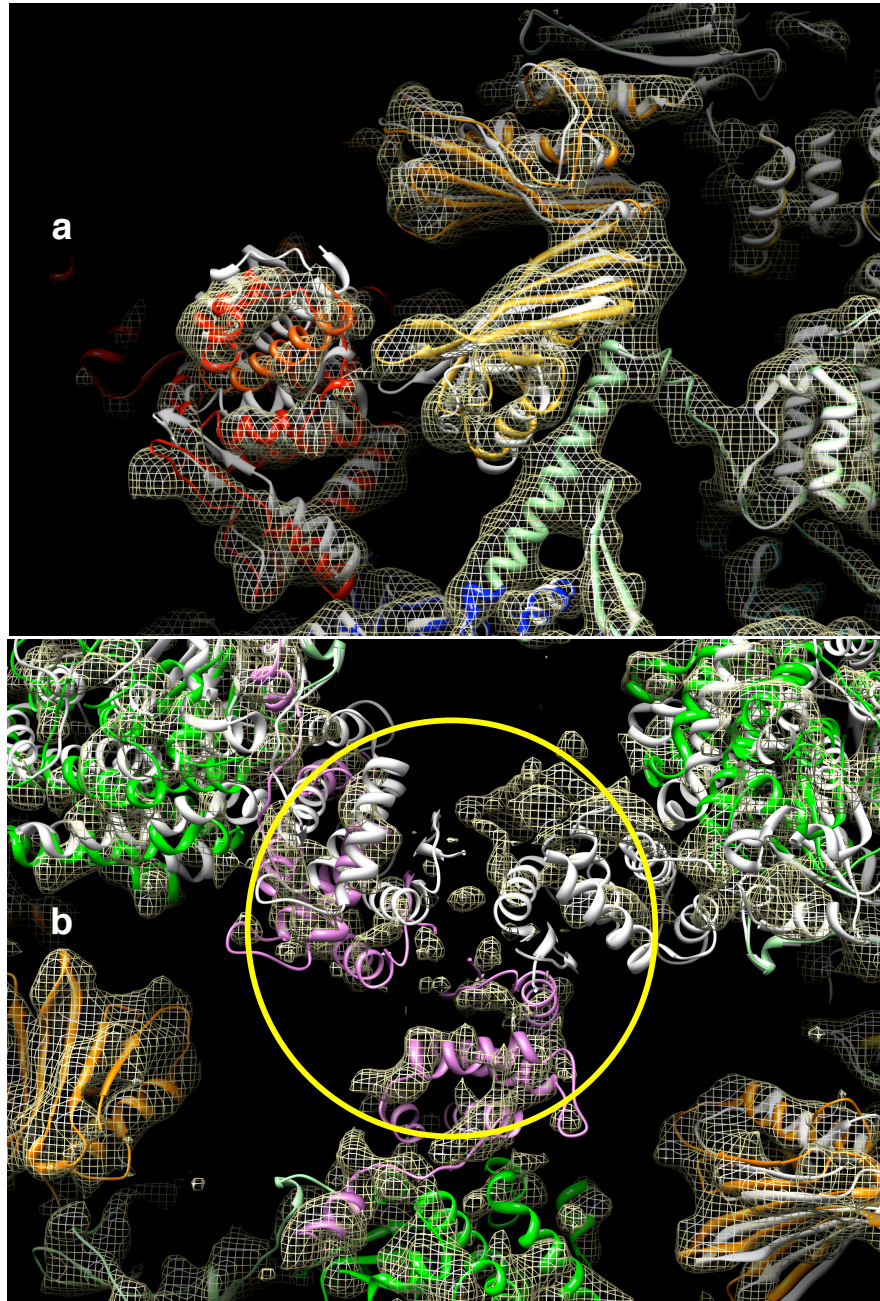


**Figure 12.2.** Differences between the yeast FAS structure fitted to the EM map and the X-ray structure (2VKZ) (Johansson *et al.* 2008). Fitted domains are colored according to figure 8, while the corresponding X-ray structure is white. (a) Remodeling of the DH and MPT domains in the EM map density. (b) The X-ray structure (white) does not fit the structural domain near the three-fold axis (encircled in yellow). Refitting (pink) reveals a movement of up to 15 Å. The contact with the adjacent AT domain (green) remains intact.

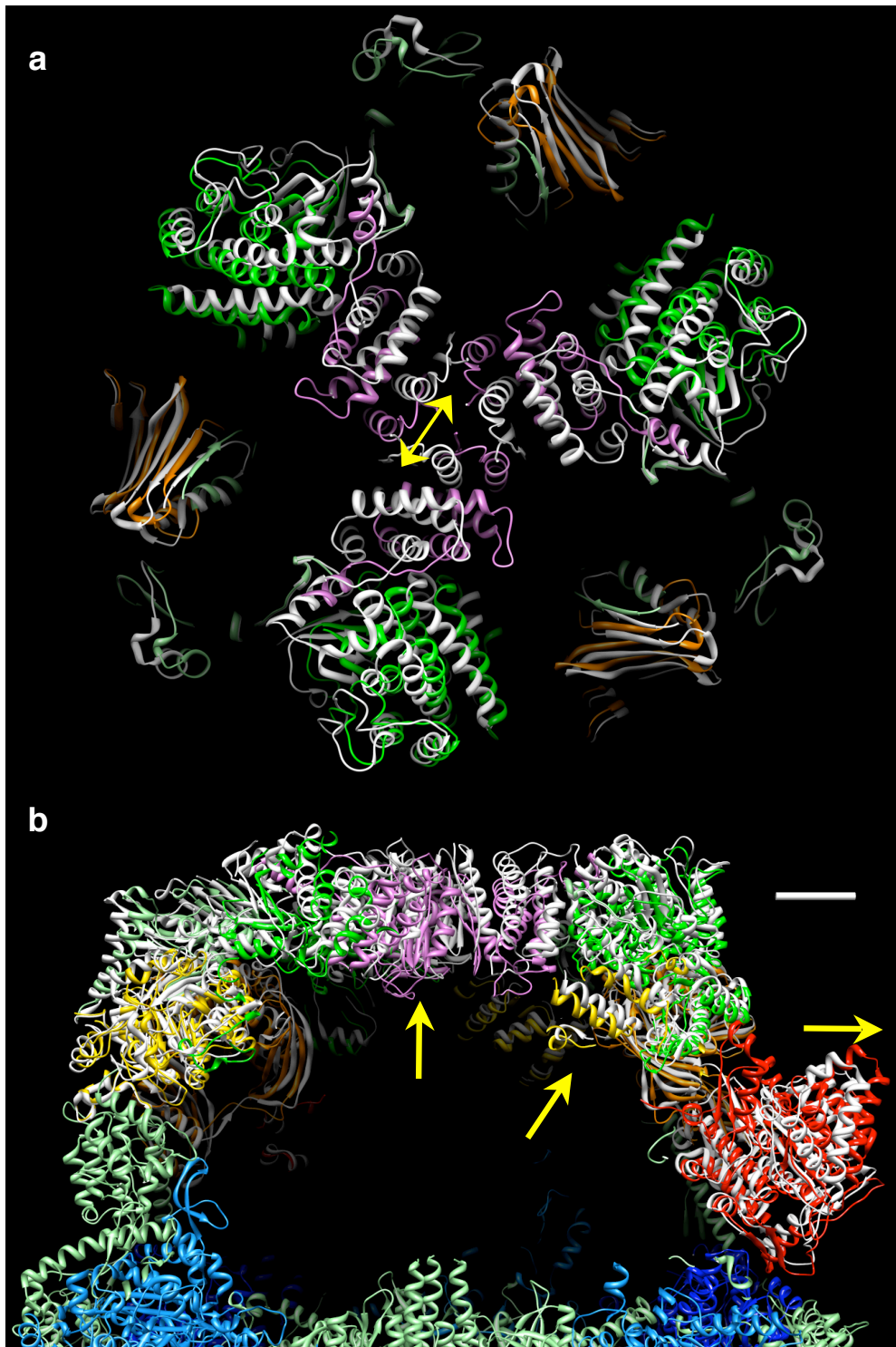


**Figure 13.** Overall differences between the yeast FAS structure fitted to the EM map (color scheme Fig. 8) and the X-ray structure (2VKZ, white) (Johansson et al. 2008). (a) The trimer contact at the tip of the barrel is completely different in the EM and X-ray structures. The double-headed arrow indicates the movement of this helix in the crystal structure with respect to the EM- structure. (b) Side view of one dome (scale bar, 20 Å); the arrows indicate the overall movement of domains in the crystal structure relative to the EM map due to compression by crystal contacts. Overall, the FAS barrel is shorter by ~20 Å and the dome is wider by up to 18 Å in solution.

### 3.6 Multiple positions of the acyl carrier protein

It has been postulated that the ACP domain carries the growing fatty acid chain substrate iteratively to the various catalytic sites in the reaction chamber (Fig.14a) (Leibundgut et al. 2007; Lomakin et al. 2007; Johansson et al. 2008). The AT domain participates in the initiation of fatty acid chain synthesis and the MPT, KS, KR, DH and ER domains each carry out different steps in the chain elongation cycle. So far, however, there has been no experimental evidence for such a substrate shuttling mechanism. In the three X-ray structures of yeast FAS (Leibundgut et al. 2007; Lomakin et al. 2007; Johansson et al. 2008) the ACP is fixed in a single position at the equator near the KS domain (Fig.14a). The relative affinities of the catalytic domains for the ACP are unknown.

We assessed the variability of our 3D volume by a 3D variance map, using a bootstrap algorithm (Penczek et al. 2006a; Penczek et al. 2006b). A suite of 100 3D volumes was calculated from a stack of ~19,000 particles by removing 1000 images randomly at a time, such that each volume was produced from a different set of ~18,000 images. The 3D variance map generated from these 100 volumes indicated a high degree of variability in the interior of the barrel (Fig. 14b). This indicates that a part of FAS moves around in the reaction chambers, as postulated for the ACP domain (Leibundgut et al. 2007). We therefore examined the map features within the reaction chambers at different threshold levels.

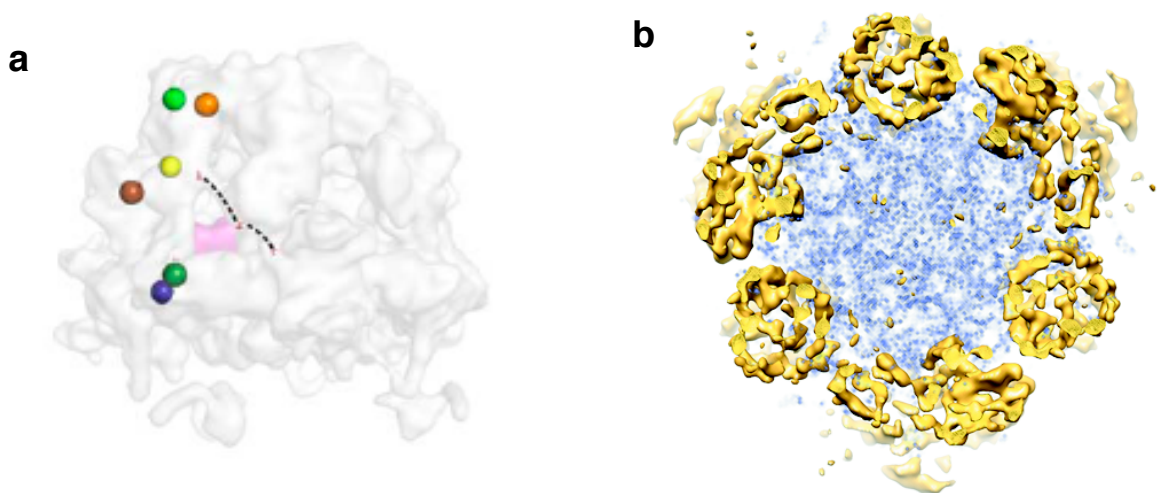


**Figure 14.** (a) Catalytic domains in one reaction chamber shown as colored spheres (b) Slice (20 Å thick) of the 3D-variance map (light blue) of the EM FAS-structure (yellow) as seen from the top of the barrel.

The map was interpreted at different isosurface contour levels to interpret domains with variable flexibility. The  $\alpha_6$  wheel and the barrel wall are clearly observable at an isosurface threshold of 3 standard deviations ( $3\sigma$ ), where, the interior of the barrel appears empty. However, several distinct regions were observed at less than 100% occupancy inside the barrel (Fig. 15a).

Six densities of similar shape and size, each next to a catalytic domain, were observed in the reaction chamber. At an isosurface threshold of  $1.5\sigma$ , three comparatively strong densities appear (Fig. 15a). Two strong densities are located near the AT and ER domains at the top of the barrel (Fig. 15c) while the third is located near the equator adjacent to the KS domain (Fig. 15b). The KR domain at the equator shows a density at a threshold level of  $0.7\sigma$  (Fig. 15b), while the MPT and DH domains show weaker densities at  $0.5\sigma$ . In the *T. lanuginosus* structure (Leibundgut et al. 2007; Lomakin et al. 2007; Johansson et al. 2008) the ACP is not resolved. The three X-ray structures of yeast FAS (Jenni et al. 2007; Leibundgut et al. 2007; Lomakin et al. 2007; Johansson et al. 2008), show the ACP domain stalled at the KS domain. The EM-map as well reveals density near the KS-domain, which was fully accounted for by the atomic model of ACP. This model (Leibundgut et al. 2007; Lomakin et al. 2007; Johansson et al. 2008) fits equally well in to the densities seen next to the KR, ER and AT domains (Fig. 8b,c). Map regions can therefore be assigned to the ACP domain, present at alternative positions in the reaction chamber (Fig. 16, **movie 2**). The length of the pantetheine arm is  $\sim 18$  Å (Leibundgut et al. 2007) and the measured distances between the phosphopantetheine attachment site at Ser180 and the catalytic sites of the KS, KR, ER and AT domains (19 Å, 20 Å, 21 Å, 18 Å respectively) are in excellent agreement.

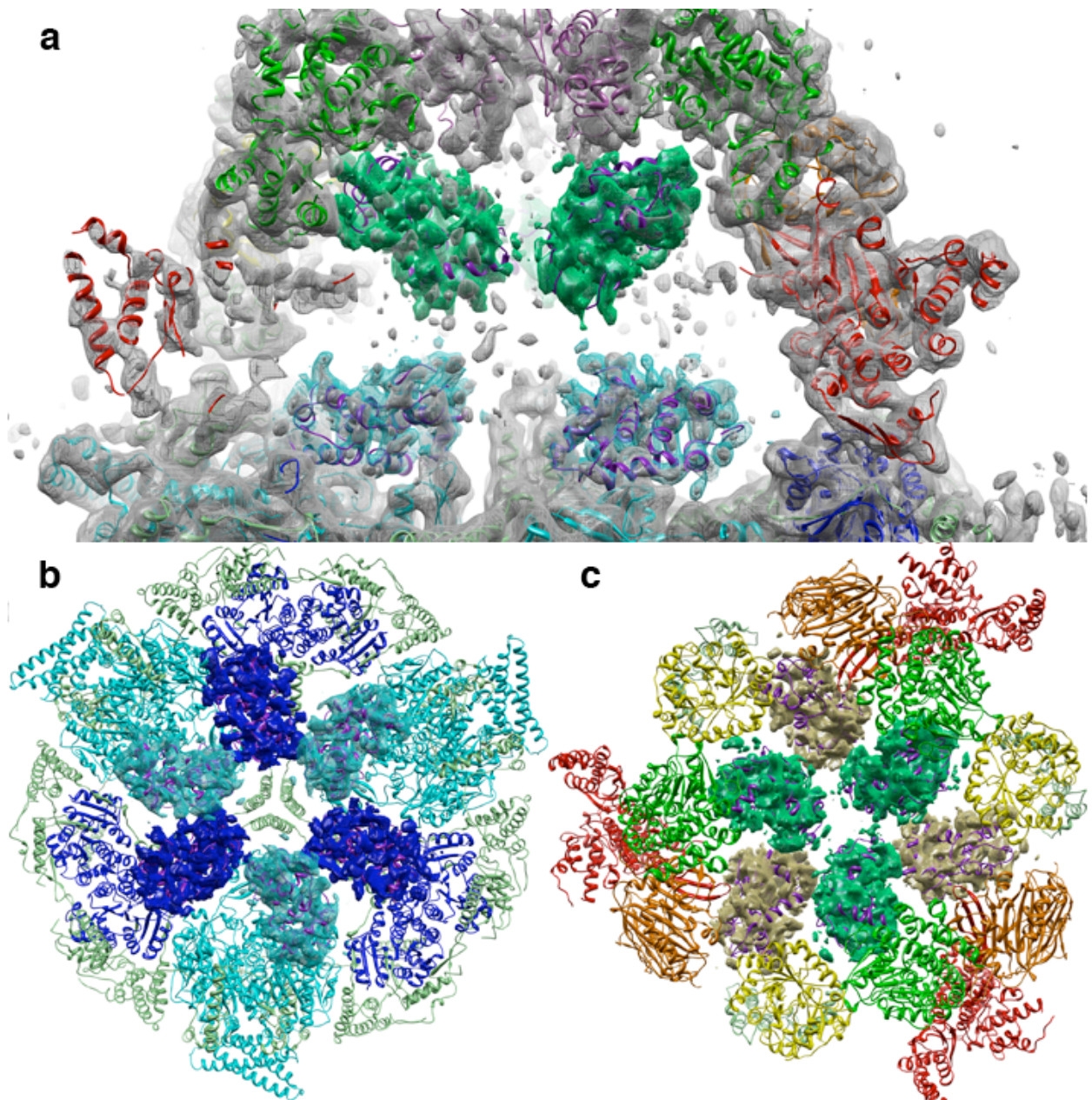


**Figure 15.** Multiple locations of the ACP domain in the reaction chamber. The domains are colored according to figure 1, depending on which catalytic domain they are next to. The walls of the reaction chamber are contoured at  $2\sigma$ , while the ACP densities are contoured at  $1.5\sigma$ . The ACP X-ray structure (Johansson et al. 2008) is shown as a purple ribbon fitted to the EM-density. (a) Section through two reaction chambers with ACP density next to the AT (green) and the KS domain (cyan); (b) ACP next to the KR (blue) and KS (cyan) domain; (c) ACP next to the AT (green) and ER (yellow) domains.

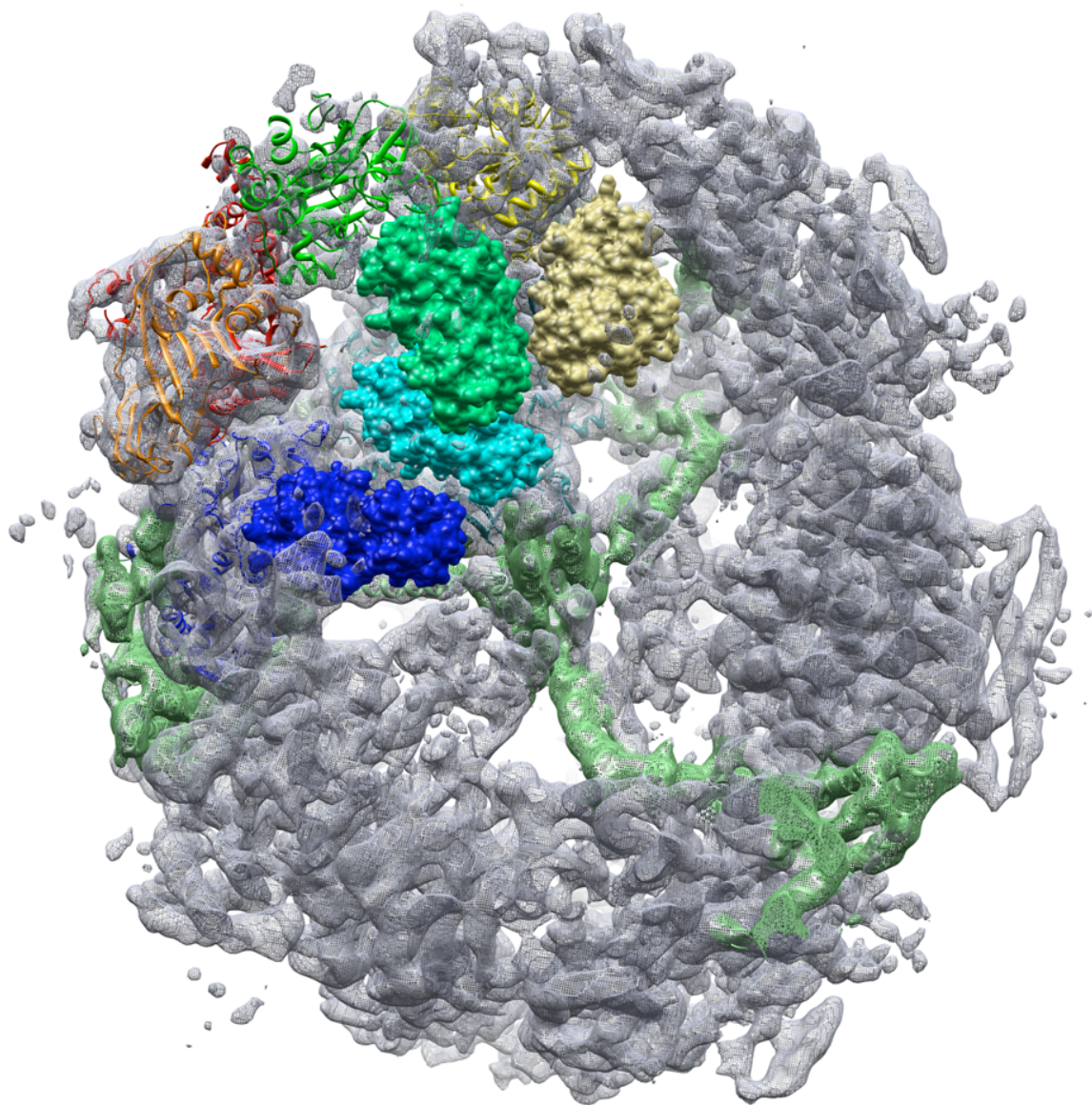


**Figure 16.** Movement of ACP in the reaction chamber. The three chambers in one dome are delineated by structural domains (light green).

### 3.7 ACP docking and relative occupancies

A surface charge potential analysis was done, in order to understand the docking mechanism of ACP inside the reaction chamber, while a calculation of the occupancy of different ACP-bound sites in the EM-map allowed an estimation of the relative binding affinity of ACP to the different catalytic domains.

Electrostatic surface potential calculation was performed for the complete yeast FAS structure and the ACP domain. The ACP faces the four different catalytic domains with the same surface, which is negatively charged, whereas the interacting surfaces of the KS, KR, ER and AT domains have a positive surface potential, as have the funnels leading to their catalytic centers. This indicates surface charge complementarity in the region where ACP docks to these domains.

The relative occupancies of ACP sites adjacent to the KS, ER and AT domains were estimated from the map densities as ~30%, while the density next to the KR domain suggests a ~10% occupancy. The estimated occupancy of the ACP positions next to the MPT and DH domains was below 10%. Considering that the FAS used for our studies is synchronized by adding NADPH and malonyl-CoA and then inhibited with cerulenin (Jenni et al. 2007; Leibundgut et al. 2007; Lomakin et al. 2007; Johansson et al. 2008), and thus not active in fatty acid chain synthesis. The occupancies reflect the affinities of the catalytic domains for ACP which remains free to move in cerulenin inhibited FAS. Apparently three domains, KS, AT and ER, each have roughly equal affinities for the ACP domain, which is about 3-fold higher than that of the KR, while the affinity of the MPT and DH domains for ACP is lower than that of the KR. As no intermediate or overlapping ACP positions were observed in the EM-map, this suggests that these occupancies near the three catalytic domains well represent the occupancy of the bound domains (as opposed to simply a generalized overlapping spatial occupancy).

## CHAPTER 4

### DISCUSSION

#### Part I: Analysis of yeast FAS EM-map at 5.9 Å

##### 4.1 Structure and dynamics of yeast FAS

Yeast FAS has evolved into the most efficient machinery available for fatty acid synthesis in a cell. It has a rigid cage-like structure with six closed reaction chambers working independently for the increased efficiency of fatty acid synthesis. Here, ACP (Leibundgut et al. 2007; Lomakin et al. 2007; Johansson et al. 2008) is proposed to be the only mobile domain performing the substrate shuttling, unlike the open mammalian FAS structure (Brignole et al. 2009), which has two open reaction chambers where the efficiency of the fatty acid synthesis is determined by the high conformational flexibility of the protein. An iterative substrate shuttling mechanism (Leibundgut et al. 2007; Lomakin et al. 2007; Johansson et al. 2008) has been proposed for the type I FAS system, where ACP plays a central role of delivering the substrate intermediates to different catalytic sites. However, ACP still remains unresolved in mammalian FAS structure, while in some recent fungal FAS studies (Leibundgut et al. 2007; Lomakin et al. 2007; Johansson et al. 2008) ACP was observed, but the substrate shuttling mechanism could not be observed as the ACP was seen fixed in a single position at the equator near the KS domain.

##### 4.2 Structure of the $\alpha_6$ wheel

In the equatorial wheel of the FAS complex, consisting of the six  $\alpha$ -chains, all secondary structure elements from the X-ray models match the corresponding densities closely. In the three X-ray structures of *S. cerevisiae* FAS (Leibundgut et al. 2007; Lomakin et al. 2007; Johansson et al. 2008), the  $\alpha_6$  wheel is incomplete, as a part of the  $\alpha$ -chain near the



KR dimer contact is missing, and the PPT domain is not resolved in two of the three structures. The *T. lanuginosus* structure (Jenni et al. 2007) shows a four-helix bundle on the outside of the KR dimer, with the helices tilted by  $\sim 45^\circ$  relative to the long axis of the complex, which is not seen in the yeast X-ray structures. The EM map density instead indicates a different structure of this part of the  $\alpha$  chain.

In one of the yeast FAS structures (Lomakin et al. 2007), the PPT domain was traced on the outside of the barrel near the KS dimer. The four-helix bundle on the outside of the equatorial  $\alpha_6$  wheel, separating the two PPT domains is resolved in all X-ray structures and its density in the EM map is clear although it has moved outward by  $\sim 2$  Å. The density of the PPT domain in our 6 Å map is comparatively weak, but the recently solved X-ray structure of the individually expressed yeast PPT domain (2WAS) (Johansson et al. 2009) superimposes well. With the PPT domain traced and the missing part of the KS domain visualized, the EM-map of the yeast FAS shows the complete structure of the  $\alpha_6$  wheel.

### **4.3 Reaction chamber conformation and biosynthetic activity**

The overall architecture of yeast FAS as seen in the EM map is similar to the X-ray structures (Leibundgut et al. 2007; Lomakin et al. 2007; Johansson et al. 2008), but significant conformational differences are observed in the positions of the domains in the barrel wall, where the four X-ray structures superimpose exactly onto one another. As the complex in our EM study had been prepared in the same way as that used in one of the X-ray structures (Leibundgut et al. 2007; Lomakin et al. 2007; Johansson et al. 2008), it is likely that these differences are caused by crystal contacts, which might easily distort the large, hollow FAS barrel. Indeed, a prominent crystal contact involves the loop extending from the MPT domain, which in our map extends  $\sim 10$  Å further into the solvent (Fig. 1; chapter 4, Fig. 12.1b). This contact is present in all crystals of yeast or *Thermomyces* FAS used for structure determination (Fig. 1). It seems to initiate an inward movement of the MPT and the adjacent DH domain, a concomitant outward movement of the ER domain, plus a displacement of the AT and the structural domain at the N-terminus of the  $\beta$ -chain near the threefold axis.

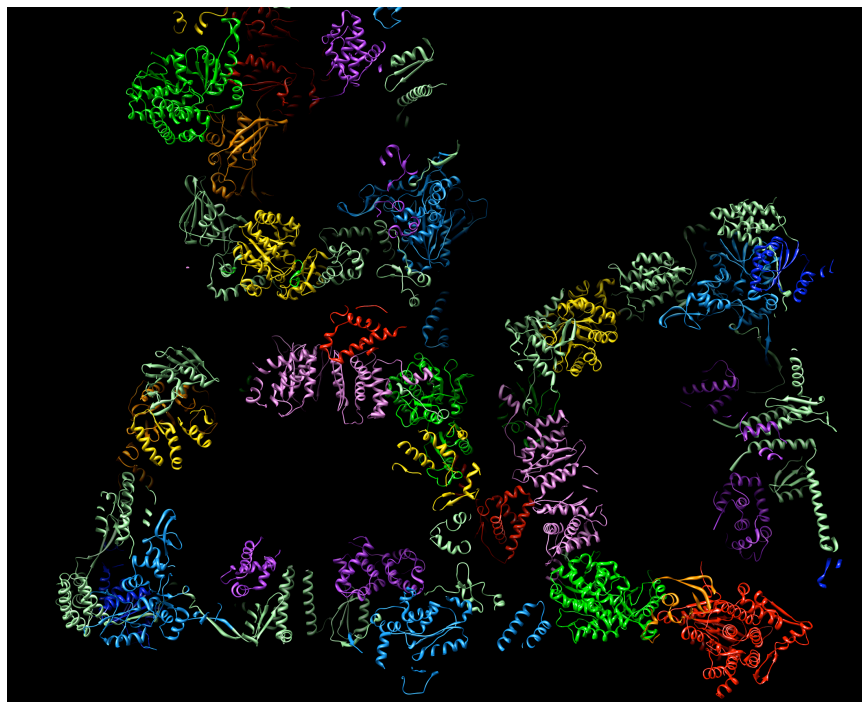


**Figure 1.** A slice view of 45 Å thickness showing the crystal contacts seen in all crystals of yeast and *Thermomyces* FAS.

As a result of these large domain movements, the reaction chamber has a different shape in the EM solution structure (chapter 4, Fig. 13). This may be the reason why so far, all yeast FAS X-ray structures (Leibundgut et al. 2007; Lomakin et al. 2007; Johansson et al. 2008) show the ACP in a single location at the equatorial KS domain. This is the only one of the observed positions where it is not in contact with the barrel wall, and therefore would be least affected by changes in shape of the reaction chamber.

The multiple positions occupied by the ACP suggest strongly that our EM map shows a conformation of the complex that is capable of carrying out fatty acid synthesis, which requires the ACP to visit different sites in the chain elongation cycle. This does not appear to be the case in the crystal structures where the ACP domain is seen in a single location. The EM map shows that it can indeed move and attach to different catalytic centers in the unconstrained solution conformation.

#### **4.4 Substrate shuttling mechanism**

The six reaction chambers in fungal FAS are thought to operate independently (Kolodziej et al. 1996). Our observation of up to six alternative ACP sites combined with uniform variance in the reaction chambers suggests that the docking events are stochastic in the inhibited enzyme. This, along with the assumed independence of the reaction chambers implies that several thousand different states of the FAS exist simultaneously in solution, not counting possible intermediates. If only a few different states coexist, as in the translating ribosome (van Heel 1987b) or in folding intermediates in the GroEL/ES system (Kanno et al. 2009) these states can be separated into individual class averages by single-particle image processing, but this is clearly not feasible in the case of fungal FAS. Instead, we visualized the mobility of the ACP domain by a variance map (Penczek et al. 2006a; Penczek et al. 2006b), which shows the highest degree of structural variability in the map regions corresponding to the reaction chamber. This indicates that the ACP domain is indeed mobile within the FAS barrel, enabling it to visit successive catalytic sites (chapter 4, Fig. 16; movie 2).

The relative occupancies of the ACP sites we observe show that no single catalytic domain has a dominant affinity for the ACP domain. For substrate delivery and chain elongation, the ACP would have to spend different amounts of time attached to each catalytic site, depending on the rate of the individual reaction. This may be reflected in the different occupancies of ACP sites in the EM map, which in turn is likely to be governed by the extent of charge and surface complementarity between the ACP and catalytic domains (Leibundgut et al. 2007; Lomakin et al. 2007; Johansson et al. 2008).

#### **4.5 Linker peptide**

In the upper half of the reaction chamber, between the MPT and the ACP density seen near the ER domain in the reaction chambers, two elongated  $\sim 64$  Å regions of density are seen (Fig. 2a) roughly parallel to one another and to the equator. Here, the density is higher than that for any of the ACP domains, though these features are not traced in any of the four X-ray structures of fungal FAS. Together with their partial occupancy and

similar appearance these features might represent alternative positions of the same structure.

Sequence analysis of yeast FAS shows a single stretch of unresolved polypeptide in this region that is long enough to account for a feature of this size. This stretch is 44-amino acids long and is thought to form the unstructured linker peptide L1 (chapter 4, Fig. 8) that tethers the ACP domain to the  $\alpha$ -chain segment of the MPT domain (Leibundgut et al. 2007; Lomakin et al. 2007; Johansson et al. 2008). According to secondary structure prediction (Kelley and Sternberg 2009) most of the sequence is likely to take on a random coil conformation, while a stretch of 12 amino-acids at the C-terminus and a stretch of 5 amino acids at the N-terminus has some propensity for helix formation (Fig. 2b). This indicates that, although the linker peptide may not tend to form an ordered structure when free in solution, it may be able to do so, if only partially, in the confined space of the reaction chamber. Other unlikely possibilities include that it might be a large conformational change of some nearby domain or some other molecule trapped during protein purification.

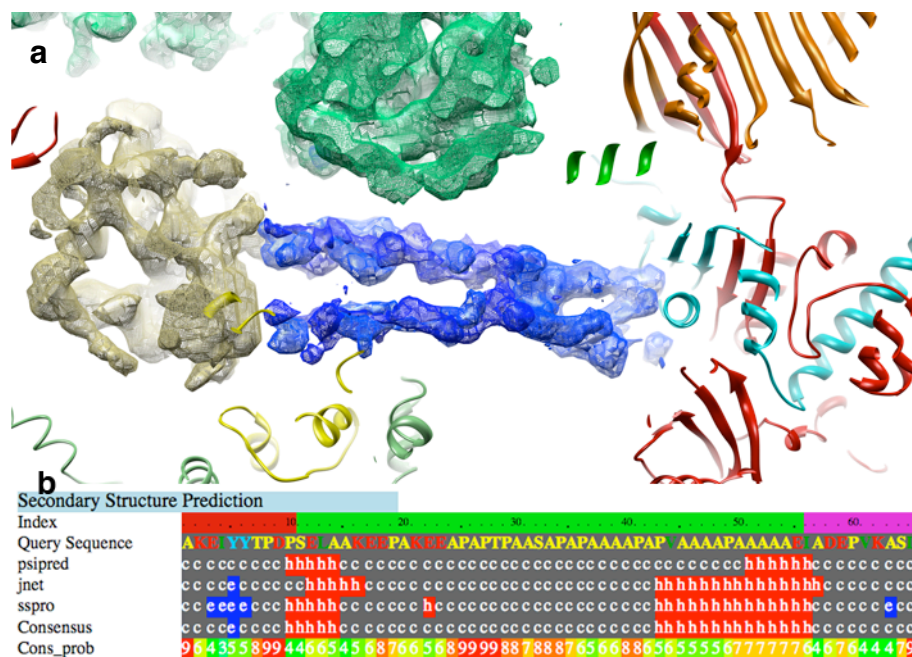


**Figure 2.** Two  $\sim 50$  Å-long densities in the reaction chamber, at an isosurface threshold of  $1.6\sigma$ . The densities are not resolved in the X-ray structures and might correspond to the peripheral linker peptide which connects the ACP ( $1.5\sigma$ , yellow mesh) to the  $\alpha$  chain segment (cyan) of the MPT domain (red). Secondary structure prediction of peripheral ACP linker obtained from PHYRE server can be seen below (c: coil, h:  $\alpha$ -helix, e:  $\beta$ -sheet). The linker sequence is shown below the green bar, while the neighboring MPT and ACP domains are presented below red and purple bars respectively.

## **Part II: Single particle analysis towards higher resolutions**

To perform structural studies of biological samples at their near native conditions has been the aim of cryo-EM in biology. Over the last decade improving resolution of the structures obtained by cryo-EM has been the main concern in this field. To achieve this, several developments in EM and software have been developed. New high-end electron microscopes with highly improved coherent electron beam sources, reduced lens aberrations and in-column sample holders have been designed. The Tecnai G2 Polara operating at 300kV is an example of such a high-end microscope which was used for this study.

The continued validity of Moore's Law has led to remarkably consistent advancements in computing power which yearly increase the amount of EM-data that can be processed in a limited time. This study utilized a parallel UNIX-computer cluster (200 processors) to process cryo-EM data worth of ~40 years of CPU processing time. Much in the way of methods development work has also contributed to the field, both in developing better mathematical and computational algorithms for the processing of data coming out of EM as well as automation of the process as a whole (Ludtke et al. 1999; Suloway et al. 2005; Grigorieff 2007).

Recently owing to the above developments, the method of single particle analysis has broken its initial resolution barrier of 20-30 Å to the new achievable resolution range of 3.5-10 Å. Studies involving various symmetric and asymmetric macro-molecular complexes have now achieved sub-nanometer resolutions (Ludtke et al. 2008); (Matadeen et al. 1999), while near-atomic resolutions have been obtained in the structural studies involving icosahedral viruses (Jiang et al. 2008; Yu et al. 2008).

## **4.6 Factors limiting high-resolution in EM**

The factors that limit resolution in cryo-electron microscopy can be broadly divided into two categories based on their source, that of data collection and data processing. The following section discusses the various factors under these categories that can be optimized to obtain high resolution in cryo-EM.

### **4.6.1 EM-data collection**

#### **Sample**

Smaller particles are difficult to align especially with regard to determining orientation parameters as compared to the larger particles. This results from the fact that small particles scatter less, resulting in poor resolution and less information in the images. The size of particles that can be studied by cryo-EM is limited to 100kD owing to the poor scattering of unstained biological samples (Henderson 1995).

Sample homogeneity is an important factor in achieving high resolution in SPA. Two kinds of heterogeneity can be present in a sample, sample heterogeneity and structural heterogeneity. The former arises from the impurity of the sample, though obvious impurities or contaminants can be easily removed during particle selection and classification steps of processing. The structural heterogeneity of the sample, arising either from damage to the structure or its inherent flexibility, can be more challenging computationally. Such data has been analyzed in studies involving ribosomes, where the method of focused classification was used for data segregation using an available initial reference. Here, the bootstrap technique was then used to obtain a 3D-variance map of the data (Penczek et al. 2006a).

#### **Ice-thickness**

Thicker ice increases the fraction of inelastically & multiple-scattered electrons, adding to the background noise in the image, which in turn reduces the signal in the image produced by the elastically scattered electrons. Low SNR in images leads to poor cross-correlation between particles and references during alignments. It is therefore important

to optimize the ice thickness of the sample (which varies based on the size of the particle e.g. 400-1200 Å) to improve the contrast in images.

### **EM-alignments**

Before collecting images at the EM, the electron optics are aligned to obtain high-resolution electron micrographs. For this, the condenser and objective lenses are aligned to a common optical axis and their apertures are also aligned relative to this axis. The result being such that the illumination cone is centered relative to the center of the viewing phosphor screen. Any astigmatism of the condenser and objective lens is adjusted by varying their current intensities. The quality of this alignment is judged by observing the Thon-rings obtained from a C-film --high quality indicated by the presence of Thon-rings at higher frequencies.

### **Magnification**

Higher magnification leads to more information in the images and finer sampling (smaller pixel size) of the images. The smaller sampling size is also less sensitive to alignment errors. For example, if the pixel-size is 4 Å then a 5-pixel alignment error will correspond to achievable resolution of  $4 \times 5$  i.e. 20 Å, while a 2 Å pixel size with the same 5-pixel alignment accuracy will still produce  $2 \times 5$ , i.e. a 10 Å structure.

### **Acceleration voltage**

The contrast in EM images is produced by electron-specimen interactions. The cross-section of scattering is inversely related to the acceleration voltage (or equivalently, the energy) of the electron, therefore events of elastic & inelastic scattering decrease with an increase in the voltage. This in turn reduces the radiation damage of the sample due to reduction in inelastic scattering, though this comes at the expense of contrast in images (due to correspondingly reduced elastic scattering). This is the cause of the increased contrast observed with a decrease in the acceleration voltage. An acceleration voltage in the range of 120-300 kV has been used in all high-resolution studies by SPA.

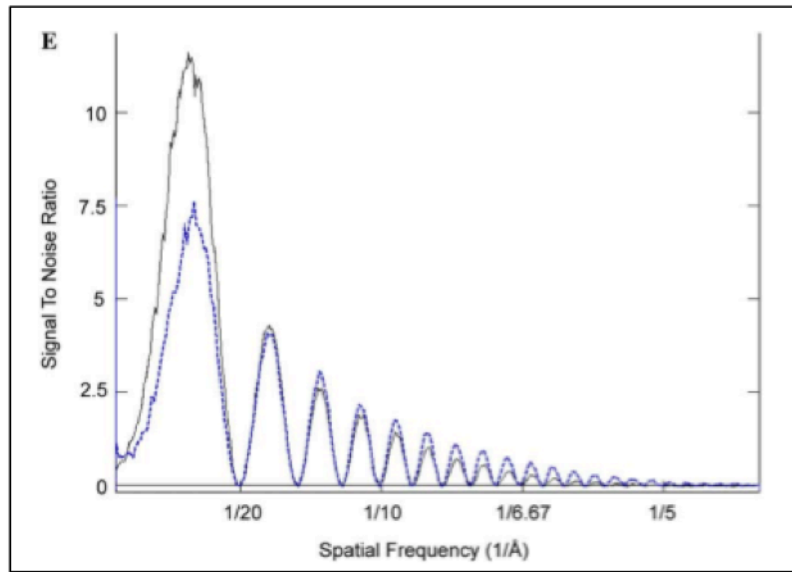


**Electron dose**

As stated before, high electron-dose increases the elastic scattering events in the sample and hence the contrast in images, but it also increases the susceptibility of the biological samples to radiation damage. A dose of 15-30  $e^-/A^2$  has been used in high-resolution studies performed by SPA.

**CCD & Film:**

Film continues to provide greater SNR at spatial frequencies greater than  $2/5$  Nyquist frequency (Nyquist being  $2 \times \text{pixel-size}$ ) and gives a larger field of view necessary for collecting the quality & quantity of data needed for obtaining high-resolution structures. Use of the CCD can also yield high resolution structures, as seen in studies of GroEL & icosahedral viruses (Booth et al. 2004), but the MTF of the CCD falls faster at higher resolutions than for film (Fig. 3). This can be improved by using more particles to build up statistics in order to retrieve information beyond  $2/5$  of Nyquist frequency. Alternatively, higher magnification can be used so that the Nyquist frequency would correspond to higher spatial frequency (Fig. 3) (Booth et al. 2004). This, however, would mean fewer particles per CCD frame --in either approach more data is required. For this, an automated method of image acquisition would make such a process easier.



Relationship of effective microscope magnification, sampling value, specimen area and 2/5 Nyquist frequency relative to those at 82800× magnification

Effective Microscope magnification	Å/pix	Dimension of CCD frame on specimen (nm)	CCD frame area compared to 82 800 (%)	2/5 Nyquist (Å)
55 200	2.71	1110	225.00%	13.55
69 000	2.17	886	144.00%	10.84
82 800	1.81	738	100.00%	9.03
1 10 400	1.35	554	56.25%	6.77
1 38 000	1.08	443	36.00%	5.42
2 07 000	0.72	295	16.00%	3.61

**Figure 3.** SNR plot of images of amorphous film recorded on CCD and photographic film. Solid line represents the SNR calculated from image collected on CCD, dotted line represents the SNR calculated from digitized image taken on film (Booth et al. 2004). Table (below) shows the variation of sampling value, specimen area and 2/5 Nyquist frequency at an effective magnification relative to those at 82,800x magnification (Booth et al. 2004; Stagg et al. 2008).

## **4.6.2 EM-data processing**

The various factors which can limit resolution during data processing are as follows:

### **CTF correction**

The oscillation of the CTF between positive and negative values leads to zeros in the spectrum of the images, this results in a loss of information at certain resolutions as discussed in detail earlier. An accurate determination of defocus is important to correct for the CTF and in order to fill in the missing information for any given value, a range of defocus values are used.

### **2D-alignments & Classification**

An accurate estimation of the translational and rotational alignment parameters of different particles w.r.t. each other (or a reference) is important so that particles in a similar orientation can be classified together. Any error in this step can lead to an error in the generated class averages representing the characteristic views of the data, which are used for back projection in to a 3D-volume.

### **Angular distribution and total number of particles**

An even distribution of different views of the particles is needed to obtain a high resolution EM-map, especially in the case of asymmetric particles. A reliable 3D-map can be generated only with the assignment of accurate Euler angles to the 2D-projections w.r.t. each other. The total number of particles needed to achieve higher resolution is inversely related to the symmetry of the protein molecule. In the case of highly symmetric icosahedral viruses, the number of particles used to achieve a near-atomic resolution structure was 10 times less than that used in the case of ribosome studies to obtain a sub-nanometer resolution structure (Table 1, 4).

## 4.7 Breaking the resolution barrier for yeast FAS structure

The aim of this project was to study structure and dynamics of yeast FAS at its near native conditions by performing high-resolution cryo-EM using the method of single particle analysis. To achieve this, several steps involved in the process i.e., sample preparation, data collection and data processing were analyzed and optimized accordingly. The factors which led to the resolution improvement were: thin-ice in sample preparation, use of high-end Polara EM, better EM-alignments for data collection, image recording at higher magnification, accurate CTF-correction, use of better 2D-alignment and classification procedures and improved 3D-reconstruction and refinement routines.

To improve the resolution of the initial EM-map, a lower acceleration voltage of 200 kV at the Polara microscope and higher electron dose ( $20-30 \text{ e}^-/\text{\AA}^2$ ) was used to collect the second dataset of  $\sim 25,000$  particles. Contrast in EM-images is contributed by electron-specimen interactions, but biological samples (composed of mainly C, N, O) produce poor contrast due to weak electron scattering properties. Although higher acceleration voltage in EM decreases inelastic scattering, it also produces poor contrast when imaging biological samples due to a decrease in total (both elastic and inelastic) scattering events (Williams and Carter 1996). Therefore, it is important to determine the optimal acceleration voltage and electron dose for a particular sample to obtain a high-contrast in the images. The loss of information at the zeroes in the CTF of the EM at a particular defocus value was compensated using CTFs obtained at different defocus values (1-3  $\mu\text{m}$ ). Additionally, the use of higher magnification helps to compensate for the drop in modulation transfer function (Frank 1996) of a negative at lower magnifications, while an increase in magnification also provides a finer sampling in the images making it less sensitive to 2D-alignment errors.

The above optimizations of various cryo-EM conditions and methods analysis helped in breaking the resolution barrier of 20  $\text{\AA}$  as obtained in the initial map to the final resolution of 5.9  $\text{\AA}$  of yeast FAS. The cryo-EM map obtained at high-resolution was

analyzed by using map-segmentation and 3D-variance analysis methods to study the structure and dynamics of yeast FAS, as discussed next.

#### 4.8 Near-atomic & sub-nanometer resolution structures by SPA

With the previously described achievements, SPA has evolved into a method with broad potential applications for the study of protein structure and dynamics at their near-native conditions, available in a new resolution range of 3.88-10 Å. In cryo-EM studies involving rotavirus DLP6 and cytoplasmic polyhedrosis virus (CPV), near atomic resolution of 3.8 Å has been achieved where ~8400 and ~30000 particles were used by the SPA method (Table 1, 2) (Zhang et al. 2008; Zhou 2008; Schuette et al. 2009). In both these studies individual beta-strands could be seen along with the grooves in helices. An atomic model was built by side-chain fitting such that almost ~100% agreement was observed between the side-chains in the EM-map and the corresponding X-ray structures, showing the reliability of side-chain prediction using near-atomic resolution EM-maps (Fig. 4A, B). The achievement of such resolution in icosahedral viral studies can be attributed to their high stability and high molecular weight (~1800 MDa), which produces high contrast in cryo-EM images and their 60-fold symmetry, which reduces the number of images needed to generate a high-resolution 3D-map.

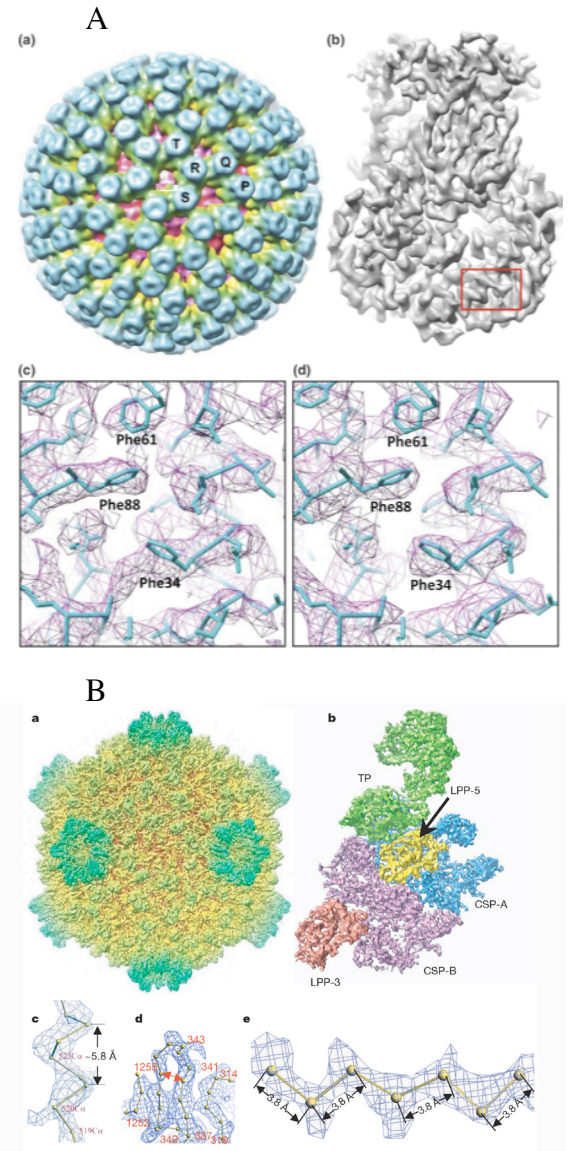


**Figure 4.** Near-atomic resolution structures by SPA. (A) Overall structure of rotavirus filtered at 20 Å (a); (b) a single viral protein (VP6) at 3.88 Å; (c) & (d) fitting of side chains from the corresponding X-ray structure into the EM-density (shown at 3.88 Å) (Zhang et al. 2008). (B) Overall structure of CPV virus at 3.88 Å (a); (b) an asymmetric unit (at 3.88 Å); (c) & (d) EM-density for an alpha-helix and individual beta-strands fit with the corresponding X-ray structure; (e) fit of C $\alpha$ -model of a  $\beta$ -strand into the EM-density, the EM-map shows clear density for side-chains (Zhou 2008).

There are two intermediate symmetry structures other than icosahedral viruses that have been studied in a resolution range of 4-6 Å (Table 3). GroEL (D7 symmetry) has been studied at 4.1 Å, 5.4 Å and 6 Å resolutions (Fig. 5A-C) and has been extensively used over the last decade as a test specimen for software development in this field (Ludtke et al. 2008). Yeast FAS structure (D3 symmetry), presented in this study, is the other low-symmetry structure which has been studied at 5.9 Å resolution (Gipson et al. 2009). When compared to the EM-map of GroEL at a similar resolution of 6 Å, the FAS map resolves helices much better and even helical-pitch can be seen, in the case of helices present at the equator (Fig. 5D). Additionally, the density for the isoalloxazine ring of FMN can be seen in the FAS-map, as shown in the results section. When compared at the level of resolvable structural features (e.g. alpha-helices, beta-sheets etc.) the FAS details appear closer to the GroEL details solved at 5.4 Å and 4.2 Å rather than the map at 6Å.

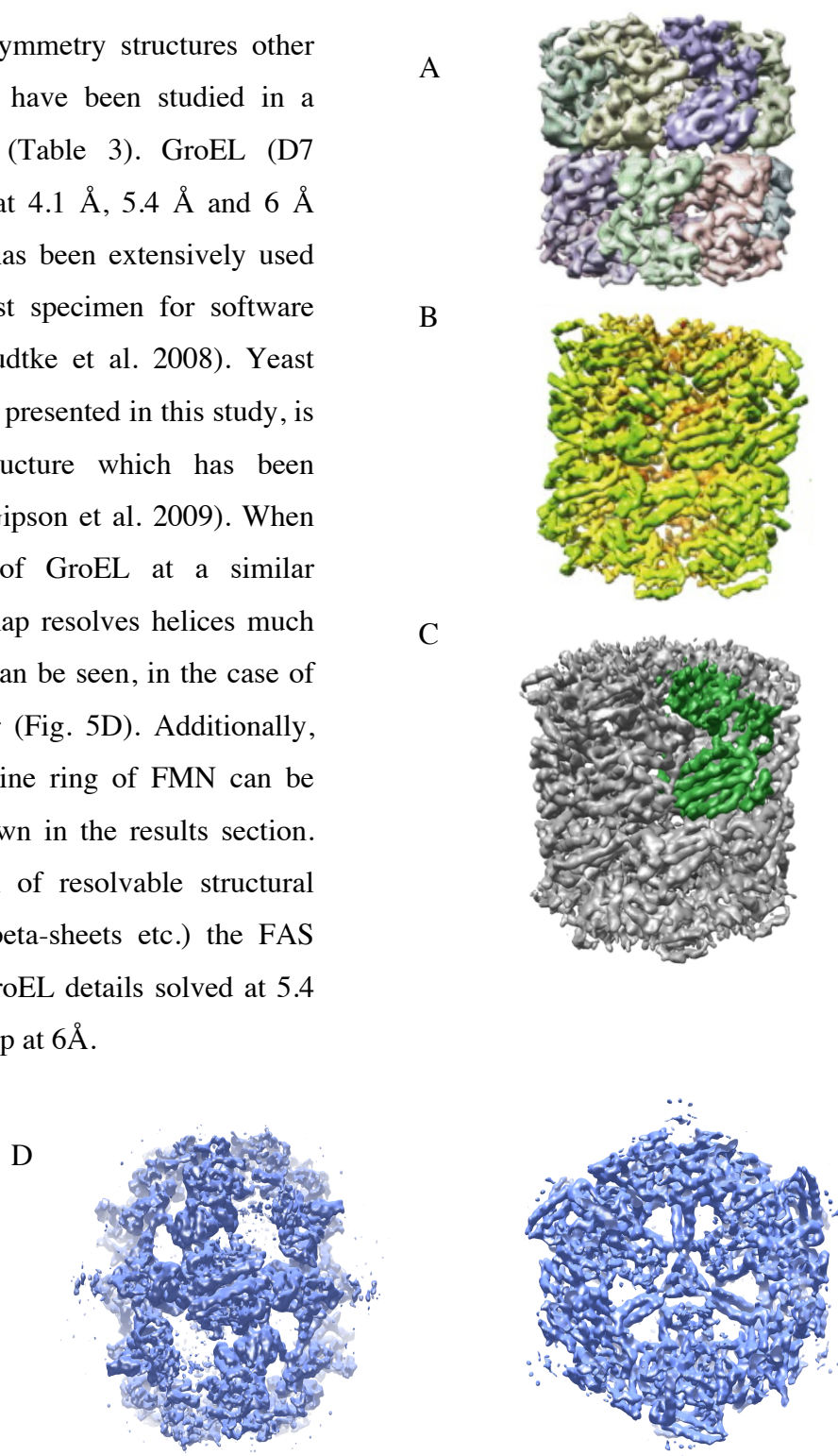


**Figure 5.** Low-symmetry structures obtained by SPA at 5-6 Å. (A), (B) & (C) overall structure of GroEL at 6 Å, 5.4 Å and 4.2 Å respectively (Ludtke et al. 2008); (D) overall structure of yeast FAS at 5.9 Å, where a side-view and the equatorial-wheel are shown (Gipson et al. 2009).

Ribosomes are the only non-symmetric structures which have been studied in the resolution range of 6-10Å (Fig. 6, Table 4). The cryo-EM studies on the ribosome in complex with various translational factors (e.g. elongation factor EF-Tu and signal recognition particle/SRP) over the last few decades have made major contributions towards the understanding of the structure and dynamics of protein synthesis in the cell (Halic et al. 2006). The study on heterogeneous ribosome data has even led to the development of the SPA technique into new directions such as bootstrap 3D-variance analysis and focused or reference-based classification methods, used to analyze the conformational and structural (e.g. bound or unbound ligand state) variance present in the data (Penczek et al. 2006a; Penczek et al. 2006b).

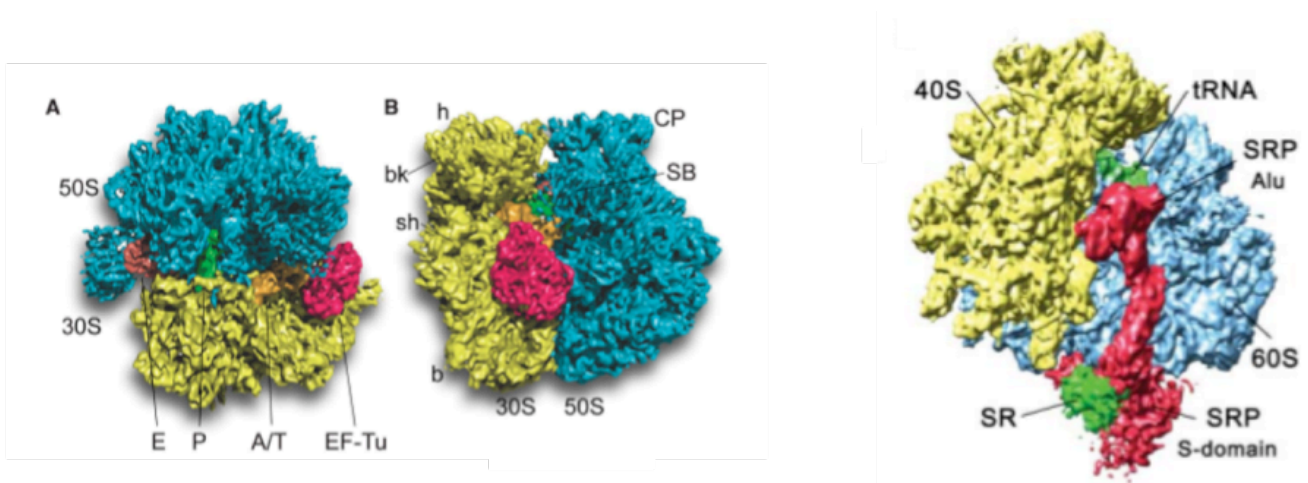


**Figure 6.** Asymmetric structures obtained by SPA at 6-7 Å. (A) & (B) a surface representation of ribosome along with elongation factor EF-Tu at 6.4 Å (left) (Schuette et al. 2009); structure of ribosome bound to signal recognition complex (SRP) at 7.4 Å resolution (right) (Halic et al. 2006).

Table 1-4. Imaging conditions of various structures (submitted in EM-database with their respective EMID) solved in a resolution range of 3-4 Å (Table 1), 4-5 Å (Table 2), 5-6 Å (Table 3), 6-8 Å (Table 4) by SPA.

**Table 1**

EMID	Sample name	Resolution (in Å)	Microscope	Magnification	Recording medium	No. of Particles
1461	Rotavirus VP6 protein ( <i>icosahedral</i> )	3.8	FEI TECNAI F30 (300kV)	59000	Film	~8400
1571	VP7 recoated rotavirus DLP ( <i>icosahedral</i> )	3.8	FEI TECNAI F30 (300kV)	59000	Film	Un-published
1508	Cytoplasmic polyhedrosis virus ( <i>icosahedral</i> )	3.9	FEI TECNAI F30 (300kV)	154380	CCD	~13000

**Table 2**

EMID	Sample name	Resolution (in Å)	Microscope	Magnification	Recording medium	No. of Particles
5001	Native unliganded GroEL, residual ADP (D7)	4.2	JEOL 3000SFF (300kV)	60000	Film	~20400
1609	VP7 recoated rotavirus DLP ( <i>icosahedral</i> )	4.2	FEI TECNAI F30 (300kV)	59000	Film	Un-published
5003	Bacteriophage epsilon15 ( <i>icosahedral</i> )	4.5	JEOL 3000SFF (300kV)	60000	Film	~36259
5002	Native unliganded GroEL, residual ADP (C7)	4.7	JEOL 3000SFF (300kV)	60000	Film	~20400



**Table 3**

<b>EMID</b>	<b>Sample name</b>	<b>Resolution (in Å)</b>	<b>Microscope</b>	<b>Magnification</b>	<b>Recording medium</b>	<b>No. of Particles</b>
1460	Bovine rotavirus DLP <i>(icosahedral)</i>	5.1	FEI TECNAI F30 <i>(300kV)</i>	59000	Film	~8400
1457	GroEL <i>(D7)</i>	5.4	FEI TECNAI F20 <i>(120kV)</i>	100000	CCD	~41000
1623	Cerulenin-inhibited yeast FAS <i>(D3)</i>	5.9	FEI TECNAI F30 <i>(200kV)</i>	59000	Film	~19000
1081	Native naked GroEL <i>(D7)</i>	6.0	JEOL 2010F <i>(200kV)</i>	50000	Film	~39000

**Table 4**

<b>EMID</b>	<b>Sample name</b>	<b>Resolution (in Å)</b>	<b>Microscope</b>	<b>Magnification</b>	<b>Recording medium</b>	<b>No. of Particles</b>
5030	Ribosome in complex with Tu(EF-Tu), tRNA & GDP	6.4	FEI TECNAI F30	39000	Film	~323688
5036	70S ribosome from E. coli complex 70S- fMet-tRNA-Phe- tRNA-EF-Tu-GDP- kirromycin	6.7	FEI TECNAI F30	59000	Film	~130000
1315	Complex of <i>Thermus thermophilus</i> 70S ribosomes and EF- G-GMPPNP	7.3	FEI TECNAI F30	39000	Film	~77000
1285	Yeast 80S ribosome in complex with the CrPV IRES RNA	7.3	FEI TECNAI F30	39000	Film	~290000
1217	Ribosome-SRP-SR	7.4	FEI TECNAI F30	N/A	Film	~100000

## 4.9 Conclusions and Outlook

We have presented a 6 Å map obtained by cryo-electron microscopy of single particles of yeast FAS. This study shows that single particle analysis is a powerful tool for the study of the structure and dynamics of macro-molecular complexes such as yeast FAS in its native environment. It is possible to obtain higher resolutions by using single particle analysis, which as a field has moved from earlier limits at low-resolution ranges of 20-30 Å to recent higher resolutions such as 4-6 Å. With recent studies (Jiang et al. 2008; Yu et al. 2008) showing that near atomic resolutions are possible with Single Particle analysis (owing to advancements in microscopy and computation) this method is increasingly finding traction in the world of atomic-resolution structural biology.

Our 6 Å EM map of yeast FAS presents for the first time a virtually complete structure of this 2.6 MDa cellular machine. The map shows all domains in the  $\alpha$ -polypeptide chain, including the PPT and KS domains that were previously absent or incompletely resolved. The arrangement of catalytic and structural domains of the  $\beta$  chain forming the barrel wall is significantly different in the unconstrained solution structure observed in our EM map, in which the reaction chamber is both wider and lower than in the crystal structures (Leibundgut et al. 2007; Lomakin et al. 2007; Johansson et al. 2008). The more constrained conformation of the  $\beta$  dome in the X-ray structures appears to be due to a crystal contact. This contact pushes the MPT domain inward, resulting in a change in the position and orientation of all other domains in the  $\beta$  chain which move relative to one another as rigid bodies. The shape of the reaction chamber appears to affect the ability of the ACP domain to dock to the catalytic sites, as it is found in only one position in the yeast FAS X-ray structures, whereas in the EM map it is seen in up to 6 different positions with varying occupancies.

The alternative positions of the ACP domain next to the various catalytic sites in the reaction chamber provide immediate insight into the mechanism of substrate delivery and fatty acid chain elongation. Even though the enzyme complex investigated by us is inhibited and thus unable to synthesize fatty acids, the different occupancies of the ACP domain next to the catalytic centers indicate different binding affinities that are likely

related to reaction rates. Moreover, we see a pair of intriguing elongated densities in the reaction chamber that might correspond to a structured linker peptide.

Further studies are needed to understand the mechanistic details of the movement of the ACP domain inside each reaction chamber, interactions between ACPs from neighboring chambers and the role of linkers as well as forces such as electrostatics and steric hindrance on its movement. Such analytical studies can be done using designed computational simulation studies, and our collaborators Anselmi et al., are currently pursuing this. Another intriguing area of further research involving both biochemical and EM methods would be the assembly of the type I multi-enzyme complex, which is still not understood. Presently, our collaborators Grininger et al., are trying to understand the assembly of the  $\alpha$ -chain complex. On the other hand, FAS being a macromolecular complex can be used as a model experimental sample, in the same way as GroEL, for studies involving resolution improvement in EM.

#### **4.10 Accession code**

The EM map has been deposited in the EM data bank under the entry code EMD-1623.

## **BIBLIOGRAPHY:**

Asturias, F. J., J. Z. Chadick, I. K. Cheung, H. Stark, A. Witkowski, A. K. Joshi and S. Smith (2005). "Structure and molecular organization of mammalian fatty acid synthase." Nat Struct Mol Biol **12**(3): 225-32.

Baumeister, W. (2002). "Electron tomography: towards visualizing the molecular organization of the cytoplasm." Curr Opin Struct Biol **12**(5): 679-84.

Booth, C. R., W. Jiang, M. L. Baker, Z. H. Zhou, S. J. Ludtke and W. Chiu (2004). "A 9 angstroms single particle reconstruction from CCD captured images on a 200 kV electron cryomicroscope." J Struct Biol **147**(2): 116-27.

Bottcher, B., S. A. Wynne and R. A. Crowther (1997). "Determination of the fold of the core protein of hepatitis B virus by electron cryomicroscopy." Nature **386**(6620): 88-91.

Brignole, E. J., S. Smith and F. J. Asturias (2009). "Conformational flexibility of metazoan fatty acid synthase enables catalysis." Nat Struct Mol Biol **16**(2): 190-7.

Brink, J., S. J. Ludtke, C. Y. Yang, Z. W. Gu, S. J. Wakil and W. Chiu (2002). "Quaternary structure of human fatty acid synthase by electron cryomicroscopy." Proc Natl Acad Sci U S A **99**(1): 138-43.

Byers, D. M. and H. Gong (2007). "Acyl carrier protein: structure-function relationships in a conserved multifunctional protein family." Biochem Cell Biol **85**(6): 649-62.

Cronan, J. E., Jr. (2004). "The structure of mammalian fatty acid synthase turned back to front." Chem Biol **11**(12): 1601-2.

Crowther, R. A., L. A. Amos, J. T. Finch, D. J. De Rosier and A. Klug (1970). "Three dimensional reconstructions of spherical viruses by fourier synthesis from electron micrographs." Nature **226**(5244): 421-5.

DeRosier, D. J. and A. Klug (1968). "Reconstruction of Three Dimensional Structures from Electron Micrographs." Nature **217**: 130-134.

Dolinsky, T. J., J. E. Nielsen, J. A. McCammon and N. A. Baker (2004). "PDB2PQR: an automated pipeline for the setup of Poisson-Boltzmann electrostatics calculations." Nucleic Acids Res **32**(Web Server issue): W665-7.

Dubochet, J., M. Adrian, J. J. Chang, J. C. Homo, J. Lepault, A. W. McDowell and P. Schultz (1988). "Cryo-electron microscopy of vitrified specimens." Q Rev Biophys **21**(2): 129-228.

Elmlund, H., J. Lundqvist, S. Al-Karadaghi, M. Hansson, H. Hebert and M. Lindahl (2008). "A new cryo-EM single-particle ab initio reconstruction method visualizes secondary structure elements in an ATP-fueled AAA+ motor." J Mol Biol **375**(4): 934-47.

Finking, R. and M. A. Marahiel (2004). "Biosynthesis of nonribosomal peptides." Annu Rev. Microbiol. **58**: 453-488.

Frank, J. (1990). Quart. Rev. Biophys **23**: 281-329.

Frank, J. (1996). "Three-Dimensional Electron Microscopy of Macromolecular Assemblies." Academic Press 1st Edition.

Frank, J. (2001a). "Cryo-electron microscopy as an investigative tool: the ribosome as an example." Bioessays **23**(8): 725-32.

Frank, J. (2001b). "Ribosomal dynamics explored by cryo-electron microscopy." Methods **25**(3): 309-15.

Frank, J. (2002). "Single-particle imaging of macromolecules by cryo-electron microscopy." Annu Rev Biophys Biomol Struct **31**: 303-19.

Gipson, P., D. J. Mills, R. Wouts, M. Grininger, J. Vonck and W. Kühlbrandt (2009). "Mobility of acyl carrier protein in yeast fatty acid synthase revealed by electron cryo-microscopy at 5.9 Å resolution." Submitted.

Glaeser, R. M. (1999). "Review: electron crystallography: present excitement, a nod to the past, anticipating the future." J Struct Biol **128**(1): 3-14.

Gonen, T., Y. Cheng, P. Sliz, Y. Hiroaki, Y. Fujiyoshi, S. C. Harrison and T. Walz (2005). "Lipid-protein interactions in double-layered two-dimensional AQP0 crystals." Nature **438**(7068): 633-8.

Grigorieff, N. (2007). "FREALIGN: high-resolution refinement of single particle structures." J Struct Biol **157**(1): 117-25.

Halic, M., M. Gartmann, O. Schlenker, T. Mielke, M. R. Pool, I. Sinning and R. Beckmann (2006). "Signal recognition particle receptor exposes the ribosomal translocon binding site." Science **312**(5774): 745-7.

Hall, C. E. (1955). J. Biophysic. and Biochem. Cytol **1**: 1.

Harwood, J. L. (1988). "Fatty acid metabolism." Annual Review of Plant Physiology and Plant Molecular Biology **39**: 101-138.

Henderson, R. (1995). "The potential and limitations of neutrons, electrons and X-rays for atomic resolution microscopy of unstained biological molecules." Q Rev Biophys **28**(2): 171-93.

Henderson, R., J. M. Baldwin, T. A. Ceska, F. Zemlin, E. Beckmann and K. H. Downing (1990). "Model for the structure of bacteriorhodopsin based on high-resolution electron cryo-microscopy." J Mol Biol **213**(4): 899-929.

Hoppe, W., Schramm, H.J., Sturm, M., Hunsmann, N. & Gaßmann, J (1976). "Three-dimensional electron microscopy of individual biological objects. Part III. Experimental results on yeast fatty acid synthetase." Z. Naturforsch **31a**: 1380-1390

Humphrey, W., A. Dalke and K. Schulten (1996). "VMD: visual molecular dynamics." J Mol Graph **14**(1): 33-8, 27-8.

Jenni, S., M. Leibundgut, D. Boehringer, C. Frick, B. Mikolasek and N. Ban (2007). "Structure of fungal fatty acid synthase and implications for iterative substrate shuttling." Science **316**(5822): 254-61.

Jiang, W., M. L. Baker, J. Jakana, P. R. Weigele, J. King and W. Chiu (2008). "Backbone structure of the infectious epsilon15 virus capsid revealed by electron cryomicroscopy." Nature **451**(7182): 1130-4.

Johansson, P., B. Mulinacci, C. Koestler, R. Vollrath, D. Oesterhelt and M. Grninger (2009). "Multimeric options for the auto-activation of the fungal FAS type I megasynthase." Structure **17**: 1-12.

Johansson, P., B. Wiltschi, P. Kumari, B. Kessler, C. Vonrhein, J. Vonck, D. Oesterhelt and M. Grninger (2008). "Inhibition of the fungal fatty acid synthase type I multienzyme complex." Proc Natl Acad Sci U S A **105**(35): 12803-8.

Kanno, R., A. Koike-Takeshita, K. Yokoyama, H. Taguchi and K. Mitsuoka (2009). "Cryo-EM structure of the native GroEL-GroES complex from thermus thermophilus encapsulating substrate inside the cavity." Structure **17**(2): 287-93.

Kelley, L. A. and M. J. Sternberg (2009). "Protein structure prediction on the Web: a case study using the Phyre server." Nat Protoc **4**(3): 363-71.

Kiselev, N. A., M. B. Sherman and V. L. Tsuprun (1990). "Negative staining of proteins." Electron Microsc Rev **3**(1): 43-72.

Kniazeva, M., Q. T. Crawford, M. Seiber, C. Y. Wang and M. Han (2004). "Monomethyl branched-chain fatty acids play an essential role in Caenorhabditis elegans development." PLoS Biol **2**(9): E257.

Kolodziej, S. J., P. A. Penczek, J. P. Schroeter and J. K. Stoops (1996). "Structure-function relationships of the Saccharomyces cerevisiae fatty acid synthase. Three-dimensional structure." J Biol Chem **271**(45): 28422-9.

Kuhajda, F. P. (2006). "Fatty acid synthase and cancer: new application of an old pathway." Cancer Res **66**(12): 5977-80.

Kuhajda, F. P., E. S. Pizer, J. N. Li, N. S. Mani, G. L. Frehywot and C. A. Townsend (2000). "Synthesis and antitumor activity of an inhibitor of fatty acid synthase." Proc Natl Acad Sci U S A **97**(7): 3450-4.

Kuhlbrandt, W., D. N. Wang and Y. Fujiyoshi (1994). "Atomic model of plant light-harvesting complex by electron crystallography." Nature **367**(6464): 614-21.

Leibundgut, M., S. Jenni, C. Frick and N. Ban (2007). "Structural basis for substrate delivery by acyl carrier protein in the yeast fatty acid synthase." Science **316**(5822): 288-90.

Little, J. L., F. B. Wheeler, D. R. Fels, C. Koumenis and S. J. Kridel (2007). "Inhibition of fatty acid synthase induces endoplasmic reticulum stress in tumor cells." Cancer Res **67**(3): 1262-9.

Loftus, T. M., D. E. Jaworsky, G. L. Frehywot, C. A. Townsend, G. V. Ronnett, M. D. Lane and F. P. Kuhajda (2000). "Reduced food intake and body weight in mice treated with fatty acid synthase inhibitors." Science **288**(5475): 2379-81.

Lomakin, I. B., Y. Xiong and T. A. Steitz (2007). "The crystal structure of yeast fatty acid synthase, a cellular machine with eight active sites working together." Cell **129**(2): 319-32.

López, M. and C. Diéguez (2007). "C75, a Fatty Acid Synthase (FAS) Inhibitor." Recent Patents on Endocrine, Metabolic & Immune Drug Discovery **1**: 53-62.

Lucic, V., F. Forster and W. Baumeister (2005). "Structural studies by electron tomography: from cells to molecules." Annu Rev Biochem **74**: 833-65.

Ludtke, S. J., M. L. Baker, D. H. Chen, J. L. Song, D. T. Chuang and W. Chiu (2008). "De novo backbone trace of GroEL from single particle electron cryomicroscopy." Structure **16**(3): 441-8.

Ludtke, S. J., P. R. Baldwin and W. Chiu (1999). "EMAN: semiautomated software for high-resolution single-particle reconstructions." J Struct Biol **128**(1): 82-97.



Lynen, F. (1980). "On the structure of fatty acid synthetase of yeast." Eur J Biochem **112**(3): 431-42.

Maier, T., S. Jenni and N. Ban (2006). "Architecture of mammalian fatty acid synthase at 4.5 Å resolution." Science **311**(5765): 1258-62.

Maier, T., M. Leibundgut and N. Ban (2008). "The crystal structure of a mammalian fatty acid synthase." Science **321**(5894): 1315-22.

Majerus, P. W., A. W. Alberts and P. R. Vagelos (1965a). "Acyl Carrier Protein. 3. An Enoyl Hydrase Specific for Acyl Carrier Protein Thioesters." J Biol Chem **240**: 618-21.

Majerus, P. W., A. W. Alberts and P. R. Vagelos (1965b). "Acyl carrier protein. VII. The primary structure of the substrate-binding site." J Biol Chem **240**(12): 4723-6.

Matadeen, R., A. Patwardhan, B. Gowen, E. V. Orlova, T. Pape, M. Cuff, F. Mueller, R. Brimacombe and M. van Heel (1999). "The Escherichia coli large ribosomal subunit at 7.5 Å resolution." Structure **7**(12): 1575-83.

Milne, J. L. and S. Subramaniam (2009). "Cryo-electron tomography of bacteria: progress, challenges and future prospects." Nat Rev Microbiol **7**(9): 666-75.

Mitsuoka, K., T. Hirai, K. Murata, A. Miyazawa, A. Kidera, Y. Kimura and Y. Fujiyoshi (1999). "The structure of bacteriorhodopsin at 3.0 Å resolution based on electron crystallography: implication of the charge distribution." J Mol Biol **286**(3): 861-82.

Morisaki, N., H. Funabashi, R. Shimazawa, J. Furukawa, A. Kawaguchi, S. Okuda and S. Iwasaki (1993). "Effect of side-chain structure on inhibition of yeast fatty-acid synthase by cerulenin analogues." Eur J Biochem **211**(1-2): 111-5.

Nelson, D. L. and M. M. Cox (2000). "Lehninger Principles of Biochemistry." W.H. Freeman **3rd Edition**.

Nogales, E., S. G. Wolf and K. H. Downing (1998). "Structure of the alpha beta tubulin dimer by electron crystallography." Nature **391**(6663): 199-203.

Penczek, P. A., J. Frank and C. M. Spahn (2006a). "A method of focused classification, based on the bootstrap 3D variance analysis, and its application to EF-G-dependent translocation." J Struct Biol **154**(2): 184-94.

Penczek, P. A., C. Yang, J. Frank and C. M. Spahn (2006b). "Estimation of variance in single-particle reconstruction using the bootstrap technique." J Struct Biol **154**(2): 168-83.

Penczek, P. A., J. Zhu, R. Schröder and J. Frank (1997). " Three Dimensional Reconstruction with Contrast Transfer Compensation from Defocus Series " Scanning Microscopy **11**: 147.

Pettersen, E. F., T. D. Goddard, C. C. Huang, G. S. Couch, D. M. Greenblatt, E. C. Meng and T. E. Ferrin (2004). "UCSF Chimera--a visualization system for exploratory research and analysis." J Comput Chem **25**(13): 1605-12.

Radermacher, M., T. Wagenknecht, A. Verschoor and J. Frank (1987). "Three-dimensional reconstruction from a single-exposure, random conical tilt series applied to the 50S ribosomal subunit of Escherichia coli." J Microsc **146**(Pt 2): 113-36.

Rangan, V. S., A. K. Joshi and S. Smith (2001). "Mapping the functional topology of the animal fatty acid synthase by mutant complementation in vitro." Biochemistry **40**(36): 10792-9.

Rosenthal, P. B. and R. Henderson (2003). "Optimal determination of particle orientation, absolute hand, and contrast loss in single-particle electron cryomicroscopy." J Mol Biol **333**(4): 721-45.

Sachse, C., J. Z. Chen, P. D. Coureux, M. E. Stroupe, M. Fandrich and N. Grigorieff (2007). "High-resolution electron microscopy of helical specimens: a fresh look at tobacco mosaic virus." J Mol Biol **371**(3): 812-35.

Schroder, G. F., A. T. Brunger and M. Levitt (2007). "Combining efficient conformational sampling with a deformable elastic network model facilitates structure refinement at low resolution." Structure **15**(12): 1630-41.

Schuette, J. C., F. V. t. Murphy, A. C. Kelley, J. R. Weir, J. Giesebrecht, S. R. Connell, J. Loerke, T. Mielke, W. Zhang, P. A. Penczek, V. Ramakrishnan and C. M. Spahn (2009). "GTPase activation of elongation factor EF-Tu by the ribosome during decoding." EMBO J **28**(6): 755-65.

Schuster, A. (1898). "On the investigation of hidden periodicities with application to a supposed 26 day period of meteorological phenomena." Terrestrial Magnetism and Atmospheric Electricity **3**: 13-41.

Schweizer, E. and J. Hofmann (2004). "Microbial type I fatty acid synthases (FAS): major players in a network of cellular FAS systems." Microbiol Mol Biol Rev **68**(3): 501-17.

Singh, N., S. J. Wakil and J. K. Stoops (1985). "Yeast fatty acid synthase: structure to function relationship." Biochemistry **24**(23): 6598-602.

Smith, S., A. Witkowski and A. K. Joshi (2003). "Structural and functional organization of the animal fatty acid synthase." Prog Lipid Res **42**(4): 289-317.

Smith, S. W. (2002). "The Scientist and Engineer's Guide to Digital Signal Processing." Newnes 2nd Edition.

Stagg, S. M., G. C. Lander, J. Quispe, N. R. Voss, A. Cheng, H. Bradlow, S. Bradlow, B. Carragher and C. S. Potter (2008). "A test-bed for optimizing high-resolution single particle reconstructions." J Struct Biol **163**(1): 29-39.

Suloway, C., J. Pulokas, D. Fellmann, A. Cheng, F. Guerra, J. Quispe, S. Stagg, C. S. Potter and B. Carragher (2005). "Automated molecular microscopy: the new Legion system." J Struct Biol **151**(1): 41-60.

van Heel, M. (1984). "Multivariate statistical classification of noisy images (randomly oriented biological macromolecules)." Ultramicroscopy **13**(1-2): 165-83.

van Heel, M. (1987a). "Angular reconstitution: a posteriori assignment of projection directions for 3D reconstruction." Ultramicroscopy **21**(2): 111-23.

van Heel, M. (1987b). "Similarity measures between images." Ultramicroscopy **21**: 95-100.

van Heel, M., G. Harauz, E. V. Orlova, R. Schmidt and M. Schatz (1996). "A new generation of the IMAGIC image processing system." J Struct Biol **116**(1): 17-24.

Wakil, S. J., J. K. Stoops and V. C. Joshi (1983). "Fatty acid synthesis and its regulation." Annu Rev Biochem **52**: 537-79.

White, S. W., J. Zheng, Y. M. Zhang and Rock (2005). "The structural biology of type II fatty acid biosynthesis." Annu Rev Biochem **74**: 791-831.

Williams, D. B. and B. C. Carter (1996). "Transmission electron microscopy: A textbook of material sciences." Springer I.

Witkowski, A., A. Ghosal, A. K. Joshi, H. E. Witkowska, F. J. Asturias and S. Smith (2004). "Head-to-head coiled arrangement of the subunits of the animal fatty acid synthase." Chem Biol **11**(12): 1667-76.

Woolford, D., G. Ericksson, R. Rothnagel, D. Muller, M. J. Landsberg, R. S. Pantelic, A. McDowall, B. Pailthorpe, P. R. Young, B. Hankamer and J. Banks (2007). "SwarmPS: rapid, semi-automated single particle selection software." J Struct Biol **157**(1): 174-88.

Yu, X., L. Jin and Z. H. Zhou (2008). "3.88 Å structure of cytoplasmic polyhedrosis virus by cryo-electron microscopy." Nature **453**(7193): 415-9.

Zhang, X., E. Settembre, C. Xu, P. R. Dormitzer, R. Bellamy, S. C. Harrison and N. Grigorieff (2008). "Near-atomic resolution using electron cryomicroscopy and single-particle reconstruction." Proc Natl Acad Sci U S A **105**(6): 1867-72.

Zhou, Z. H. (2008). "Towards atomic resolution structural determination by single-particle cryo-electron microscopy." Curr Opin Struct Biol **18**(2): 218-28.

# Zusammenfassung

## Einleitung

Die Fettsäure Synthase (FAS) ist das Schlüsselenzym bei der Biosynthese von Fettsäuren in lebenden Organismen. Zwei Arten der FAS sind bekannt. Der Typ-II FAS der Prokarioten ist aus verschiedenen Einzelenzymen aufgebaut, während der Typ-I FAS der Eukarioten aus einem Multi-Enzym Komplex besteht (Smith et al., 2003). Der Typ-I FAS Komplex der Säugetiere ist ein  $\alpha_2$ -Homodimer (Brink et al., 2002), der Typ-I FAS Komplex der Bäckerhefe wird dagegen aus einem  $\alpha_6\beta_6$  Heterododecamer aufgebaut, der eine molekulare Masse von 2,6 MDa besitzt (Brink et al., 2002). Obwohl Pilz- und Säugertyp FAS deutlich unterschiedliche Strukturen aufweisen, sind alle, zur Synthese von Fettsäuren notwendigen Enzyme (Fig. 1), in beiden FAS-Komplexen konserviert.

Früheren elektronenmikroskopischen Untersuchungen (Kolodziej et al., 1996) zeigten die FAS als eine  $260 \text{ \AA} \times 230 \text{ \AA}$  Fass-ähnliche Struktur mit D<sub>3</sub> Symmetrie. Die dreidimensionalen Röntgenkristallstrukturen der *Thermomyces lanuginosus* (Jenni et al., 2007) und *S. cerevisiae* FAS bei einer Auflösung von  $3,1 \text{ \AA}$  beziehungsweise  $4,0 \text{ \AA}$  (Leibundgut et al., 2007; Lomakin et al., 2007; Johansson et al., 2008) weisen kaum Unterschiede auf. Die sechs  $\alpha$ -Untereinheiten der FAS bauen ein äquatoriales Rad auf, das die fassartige Struktur in zwei separate Kuppeln aufteilt. Die Kuppeln wiederum bestehen aus jeweils drei  $\beta$ -Untereinheiten. Die  $\alpha$ - und  $\beta$ -Untereinheiten bilden pro Kuppel drei Reaktionsräume mit acht Reaktionszentren. Für die Reaktionszentren stellt die  $\alpha$ -Untereinheit die Phosphopentetheinyl-Transferase (PPT), das Acyl-Carrier-Protein (ACP), die Ketoacyl-Synthase (KS), die Ketoacyl-Reduktase (KR) und einen Teil der Malonyl-Palmitoyl-Reduktase (MPT)-Domäne bereit. Die Acetyl-Transferase (AT), die Enoyl-Reduktase (ER), die Dehydratase (DH) sowie der Hauptteil der MPT wird von der  $\beta$ -Untereinheit eingebracht. In der Pilztyp FAS wird das ACP durch zwei flexible Verbindungsstücke gehalten, die es mit der MPT-Domäne und dem Zentrum des äquatorialen Rads verbindet. Die Verbindungsdomänen definieren den Reaktionsradius des ACP, der weitgehend mit dem Reaktionsraum übereinstimmt (Leibundgut et al., 2007). Die Reaktionsbereiche aller katalytischen Domänen, ausgenommen die der PPT,

weisen in Richtung Reaktionsraum im Inneren der FAS (Leibundgut et al., 2007; Lomakin et al., 2007; Johansson et al., 2008). Zusätzlich zu den Reaktionsdomänen, existieren weitere sechs Strukturdomänen, zwei in der a-Untereinheit (SD1-2a) und vier in der b-Untereinheit (SD1-4b). Kürzlich veröffentlichte Studien konnten zeigen, dass jeder Reaktionsraum unabhängig von einander arbeitet (Singh et al., 2008).

Das ACP gehört zu der Klasse der universal vorkommenden, hochkonservierten *Carrier*-Proteine, die Acyl-Zwischenprodukte über den ~18 Å langen Phosphopantetheinarm binden und in sehr unterschiedlichen metabolischen Reaktionen, einschließlich denen der Biosynthese von Polyketiden oder Fettsäuren (Byers and Gong, 2007), aktiv sind. Die ACP werden in zwei Klassen, Typ-I und Typ-II, eingeteilt, die beide  $\alpha$ -helicale Strukturen mit einer konservierten, zentralen vier-Helix Anordnung besitzen. Die vier-Helix Anordnung stellt die Bindestelle für die Acylketten-Zwischenprodukte zur Verfügung. ACP-abhängige Enzymreaktionen sind essentiell für jede Zelle. Daher ist die Pilztyp FAS eine wichtige Angriffsstelle medikamentöser Behandlung (Byers und Gong, 2007).

In früheren Studien wurde postuliert, dass die ACP-Domäne nacheinander die wachsende Fettsäurekette zu den verschiedenen katalytischen Zentren des Reaktionsraums trägt (Leibundgut et al., 2007; Lomakin et al., 2007; Johansson et al., 2008). Die AT ist an der Initiation der Fettsäurekettensynthese beteiligt und stellt somit eine der ersten Reaktionsdomänen in der katalytischen Fettsäuresynthese dar. Die MPT-, KS-, KR-, DH- und ER-Domänen sind an jeweils unterschiedlichen Reaktionsschritten während der Fettsäurekettenverlängerung beteiligt. Die wachsende Fettsäure ist an die *Carrier*-Domäne gebunden. Diese transportiert die wachsende Fettsäure zu den jeweiligen katalytischen Zentren. Erreicht die Fettsäure eine Länge von 16 bis 18 Methylgruppen, wird sie von der *Carrier*-Domäne entlassen. Die Fettsäuresynthese in der Bäckerhefe vollzieht sich in der räumlich eingeschränkten Umgebung des katalytischen Käfigs, wodurch dieser aufwendige Prozess erheblich effizienter wird verglichen mit prokaryotischen Typ-II Fettsäuresynthese, die auf die Diffusion des ACP zu den einzelnen Enzymen angewiesen ist. Experimentell war es bisher jedoch nicht möglich den

Substrattransportmechanismus nachzuweisen. Die dreidimensionale Röntgenkristallstruktur der FAS aus der Bäckerhefe, in der auch das ACP aufgelöst ist, zeigt das Protein in der Position der Äquatorialebenen nahe der KS-Domäne (Leibundgut et al., 2007; Lomakin et al., 2007; Johansson et al., 2008). Die relativen Affinitäten der katalytischen Domänen für das ACP sind bisher unbekannt.

In dieser Arbeit wird die *Cryo*-Elektronenmikroskopie (*Cryo*-EM) Struktur der FAS der Bäckerhefe bei einer Auflösung von 5,9 Å beschrieben, die durch Einzelpartikelanalyse erstellt werden konnte. Die erstellte *Cryo*-EM-Mappe der FAS zeigt entscheidende Unterschiede in der Domänenorganisation verglichen mit den vier, überwiegend identischen Röntgenkristallstrukturen. Diese Unterschiede in der Domänenorganisation deuten auf eine Konformationsflexibilität der FAS-Wand hin. Beispielsweise konnte das ACP an verschiedenen Positionen neben den katalytischen Zentren innerhalb des Reaktionsraums lokalisiert werden. Dies ist der erste direkte Beweis für den ACP-vermittelten Substrattransportmechanismus.

### **Konformation des Reaktionsraums und Biosyntheseaktivität**

Die globale Architektur der FAS aus der Bäckerhefe wie sie in der *Cryo*-EM-Mappe zu erkennen ist, ähnelt sehr denen der Röntgenstrukturen (Leibundgut et al., 2007; Lomakin et al., 2007; Johansson et al., 2008). Entscheidende Konformationsunterschiede sind jedoch in den Positionen der Einzeldomänen sowie der FAS-Wand zu erkennen. Anders als in der EM-Struktur sind diese Bereiche in den vier Röntgenkristallstrukturen identisch. Da die in unseren Untersuchungen verwendete FAS in gleicher Weise behandelt wurde wie eine dessen dreidimensionale Röntgenkristallstruktur gelöst wurde (Johansson et al., 2008), ist sehr wahrscheinlich, dass die Unterschiede der Röntgenkristallstruktur durch Kristallkontakte hervorgerufen wurden, die vermutlich den großen, hohlen Bereich des FAS verformen. Tatsächlich ist ein *loop*-Bereich, der von der MPT-Domäne ausgeht, in der Röntgenkristallstruktur an einem wichtigen Kristallkontakt beteiligt. Dieser wichtige Kontakt ist in allen Kristallen der *Thermomyces* FAS vorhanden. In unserer *Cryo*-EM-Mappe ragt dieser *loop* jedoch etwa 10 Å in den freien, Lösungsmittel-zugänglichen Bereich. Der Kristallkontakt scheint eine Bewegung der MPT-Domäne in Richtung der

FAS Innerenseite zu bewirken. Eine entgegengesetzt Bewegung führt dagegen die DH-Domäne durch, was eine ebenfalls nach außen gerichtete Bewegung der ER-Domäne verursacht. Die AT- und die strukturelle Domäne der b-Kette des N-Terminus zeigt eine Verschiebung hin zur dreizähligen Achse. Das ACP hingegen ist in den verschiedenen Röntgenkristallstrukturen (Leibundgut et al., 2007; Lomakin et al., 2007; Johansson et al., 2008) nahe der äquatorialen KS-Domäne zu finden und ist vermutlich aufgrund des Kristallkontakts an dieser Stelle fixiert.

Die *Cryo*-EM-Struktur zeigt bisher die einzigen Positionen, bei der das ACP nicht in Kontakt mit der FAS-Wand ist und daher den Reaktionsraum am wenigsten beeinflusst wird.

Die unterschiedlichen Positionen, in der das ACP in der *Cryo*-EM-Struktur zu finden ist, zeigen verschiedene Konformationen der FAS, die sie während des Prozesses der Fettsäurekettenverlängerung annimmt. Die *Cryo*-EM-Struktur zeigt deutlich, dass das ACP innerhalb der FAS frei beweglich ist und Verbindungen zu den verschiedenen katalytischen Zentren eingehen kann.

### **Substrattransportmechanismus**

Unsere Untersuchungen, die sechs verschiedene ACP Bindestellen im Reaktionsraum zeigen, weisen darauf hin, dass die ACP Bindung an die Bindestellen im funktionsinhibierten Enzym zufällig und unabhängig voneinander stattfindet. Dies bedeutet, dass die FAS in Lösung, ohne die möglichen Zwischenkonformationen mit einbezogen, vermutlich unzählig verschiedene Konformationen annehmen kann.

Nehmen Protein-Komplexe nur einige wenige Konformationen an, wie im Fall des translatierenden Ribosoms (Penczek et al., 2006) oder die Faltungszwischenstufen im GroEL/ES-Systems (Kanno et al., 2009), kann man diese während der Einzelpartikelanalyse in separate Klassen aufteilen und entsprechend bearbeiten. Aufgrund der Vielzahl der Konformationen ist dies jedoch nicht bei der Bearbeitung der Pilztyp FAS möglich. Mit Hilfe einer Varianzmappe, welche die strukturelle Variabilität



im Bereich des Reaktionsraums darstellt, konnten wir die hohe Mobilität der ACP-Domäne innerhalb der FAS nachweisen (Fig. 9).

Die relative Besetzung der ACP-Bindestellen an den katalytischen Zentren, die wir in unserer *Cryo*-EM-Struktur sehen, weist auf eine eher geringe Affinität für die ACP-Domäne hin. Das ACP bindet während der Fettsäureanlieferung und –verlängerung, je nach Reaktionsrate, unterschiedlich lang an die katalytischen Zentren. Dies erklärt die unterschiedliche Besetzung der ACP-Bindestellen in unserer *Cryo*-EM-Struktur. Die Bindeaffinität wird vermutlich durch die gegenseitigen Ladungsverhältnisse zwischen den katalytischen Zentren und ACP-Domäne reguliert (Lomakin et al., 2007).

### **Verbindungspeptid**

Im oberen Bereich des Reaktionsraums nahe der MPT- und ER-Domäne zeigen sich in der *Cryo*-EM-Mappe zwei etwa 50 Å lange Dichten, die annähernd parallel zueinander und zur äquatorialen Ebene der FAS angeordnet sind. Diese Dichten, die deutlicher aufgelöst sind als die der ACP-Domänen, konnte in den Röntgenkristallstrukturen nicht gebildet werden. Die ähnliche Erscheinung und parallele Anordnung, zusammen mit der teilweisen Besetzung, lässt vermuten, dass diese beide Dichten zwei unterschiedliche Anordnungen eines einzigen Objektes darstellen.

Die Aminosäuresequenz der Bäckerhefe FAS weist nur eine Polypeptidsequenz auf, die für die in der *Cryo*-EM-Struktur aufgelöste Dichte lang genug ist. Es handelt sich dabei um einen 44-Aminosäure langen Bereich, der vermutlich das überwiegend unstrukturierte Linkerpeptid L1 darstellt. Das Linkerpeptid verbindet die ACP-Domäne mit dem  $\alpha$ -Kettensegment der MPT-Domäne (Leibundgut et al., 2007). Sekundärstrukturvorhersagen (Kelley und Sternberg, 2009) zeigen, dass der Großteil des Peptids eine ungeordnete *coil*-Struktur annimmt, während jedoch etwa 12 Aminosäuren des C-Terminus und 5 Aminosäuren des N-Terminus vermutlich helicale Formationen annehmen. Obwohl das Linkerpeptid in Lösung wahrscheinlich keine geordnete Struktur annimmt, wäre dies jedoch im eingeschränkten Bereich des Reaktionsraums möglich. Eine alternative Erklärung für die Dichte in der *Cryo*-EM-Struktur wäre ein bisher nicht charakterisiertes

Molekül, das möglicherweise während der Fettsäurebindung oder des -transportes benötigt wird.

### **Schlussfolgerung**

Die in dieser Arbeit präsentierte 6 Å *Cryo*-EM-Mappe der FAS aus der Bäckerhefe zeigt zum ersten Mal die vollständige Struktur der 2,6 MDa zellulären Maschine. Es können alle Domänen der  $\alpha$ -Polypeptidkette, einschließlich der PPT- und KS-Domäne, die bisher nicht oder nur teilweise aufgelöst werden konnte, dargestellt werden. Die Anordnung der katalytischen und strukturellen Domänen der  $\beta$ -Kette formen eine Fass-ähnliche Wand, die entscheidende Unterschiede verglichen mit den Röntgenkristallstrukturen (Leibundgut et al., 2007; Lomakin et al., 2007; Johansson et al., 2008) aufweist. Die FAS *Cryo*-EM-Struktur, welche aus Partikeln in Lösung erstellt wurde, die keinerlei Einschränkungen unterlagen, zeigt den Reaktionsraum deutlich weiter und niedriger verglichen mit den Röntgenkristallstrukturen. Die Form des Reaktionsraums wiederum scheint die Bindung der ACP-Domäne an den katalytischen Zentren zu beeinflussen. In den Röntgenkristallstrukturen wurden die ACP-Domänen der FAS aus der Bäckerhefe nur jeweils in einer einzigen Position gebunden, während die *Cryo*-EM-Struktur sechs unterschiedliche Positionen mit jeweils unterschiedlicher Besetzung der ACP-Domäne zeigt.

Die alternativen Positionen der ACP-Domäne in der Nähe der katalytischen Zentren im Reaktionsraum ermöglicht einen direkten Einblick in den Mechanismus der Substratanlieferung und Fettsäurekettenverlängerung. Obwohl die in unseren Untersuchungen verwendete FAS funktionell inhibiert wurde und daher die Fettsäuresynthese nicht mehr möglich war, weist die unterschiedliche Positionierung und Besetzung der ACP-Domäne in der Nähe der katalytischen Zentren auf unterschiedliche Bindungsaffinitäten hin, die wiederum von den jeweiligen Reaktionsraten während des Fettsäuresyntheseprozesses abhängig sind. Weiterhin zeigt unsere *Cryo*-EM-Mappe zwei längliche Dichten im Reaktionsraum, die in den Röntgenkristallstrukturen bisher nicht aufgelöst werden konnten. Bei diesen beiden Dichten handelt es sich vermutlich um das in diesem Fall strukturierte Linkerprotein, das in zwei Konformationen vorliegt.

April 23, 2010

## Dr. Preeti Gipson (Kumari)

### Curriculum Vitae

#### Address

Max-Planck Institute of Biophysics,  
Max-Von-Laue Str. 3, Frankfurt 60438,  
Germany.

#### Personal Details

Date of Birth: 06 May 1980  
Marital Status: Married  
Children: None  
Nationality: Indian, Permanent Resident of USA

#### Degree Qualifications

**PhD** at Max Planck Institute of Biophysics,  
Frankfurt. (April, 2010)

**Advisor:** Prof. Werner Kühlbrandt

**Thesis:** High resolution cryo-electron microscopy study of structure and dynamics of yeast fatty acid synthase by single particle analysis.

**M.Tech** in Biological Sciences and Bioengineering

Indian Institute of Technology, Kanpur, India. (August, 2005)

**Advisor:** Prof. Bhaskar Dasgupta (Center of Robotics, Dept. of Mechanical Engineering) and Dr. Balaji Prakash (Dept. of Biological Sciences & Bioengineering)

**Thesis:** Algorithmic optimization of electrostatic interactions for bound docking of protein complexes in MATLAB.

**M.Sc** in Life Sciences

School of Life Sciences, (August, 2003)

Jawaharlal Nehru University, New Delhi, India.

**Advisor:** Prof. Rajendra Prasad (School of Life Sciences) and Dr. Andrew Lynn (Bioinformatics Center)

**Thesis:** Structure determination of nucleotide binding domain of a multidrug transporter CDR1 found in *Candida albicans* by homology modeling.

**B.Sc Honors** in Botany (July, 2001)

Maitreyi College, Delhi University, India.

#### Publications

**P. Gipson**, D. J. Mills, R. Wouts, J. Vonck and W. Kühlbrandt. *Direct structural insight into the substrate shuttling mechanism of yeast fatty acid synthase revealed by cryoelectron microscopy*. Proc. of Nat. Acad. of Sci. published ahead of print March 15, 2010, doi: 10.1073/pnas.0913547107.

C. Anselmi, M. Grininger, **P. Gipson** and J. F. Gomez. *Dynamics of the acyl-carrier protein inside the fatty-acid mega-synthase*. (Submitted to J. Am. Chem. Soc. 2010).

P. Johansson, B. Wiltschi, **P. Kumari**, B. Kessler, C. Vonrhein, J. Vonck, D. Oesterhelt and M. Grininger. *Inhibition of the fungal fatty acid synthase type I multienzyme complex*. Proc. of Nat. Acad. of Sci. 105, 12803-8, 2008.

**P. Kumari**, J. Vonck, R.R. Schröder and W. Kühlbrandt. *3D Cryo-Electron Microscopy of Yeast Fatty Acid Synthase*. Microsc. and Microanal., 13, S03, 158-159, 2007.

## Invited Talks/Presentations

Selected talk and poster presentation at Gordon Research Conference, *Mobility of acyl carrier protein in yeast fatty acid synthase at 5.9Å*. New London, New Hampshire, USA, July 2009.

Invited talk on *Fatty acid synthase (type I) --megasyntase machines* at Oswalt Symposium, Frankfurt, Germany, September 2009.

Invited talk on *3D-cryoelectron microscopy of yeast fatty acid synthase*, International Microscopy Conference, Saarbrücken, Germany, September 2007.

Presented talk on *Angular 3D-reconstruction method in single particle analysis*, EMBO-workshop, Birkbeck College, London, UK, September 2007.

Invited talk on *Cryo-EM study of yeast fatty acid synthase*, University of California, Davis, USA, May 2007.

## Conferences & Workshops

*Gordon Research Conference*, Colby-Sawyer College, New London, New Hampshire, USA, July 2009.

*Single Particle Reconstruction, Map Interpretation and Visualization* workshop at University of Houston Texas, USA, December 2008.

*International Microscopy Conference* at Saarbrücken, Germany, September 2007.

*Image Processing for Cryo-electron Microscopy* course by EMBO at Institute of Structural Molecular Biology (ISMB), Birkbeck College, London, UK, September 2007.

*Acquisition and Analysis for Electron Tomography, 3DEM* course at Max Planck Institute of Biochemistry, Martinsried, Germany, March 2006.

## Scholastic Achievements

International Max-Planck Research School Scholar (IMPreS) at Frankfurt, Germany, 2005.

National competition of Council of Scientific and Industrial Research/National Eligibility Test- Junior Research Fellow (CSIR/NET-JRF) qualified, India, 2003.

National competition of Indian Council of Medical Research-Junior Research Fellow (ICMR-JRF) qualified, India, 2003.

National Graduate Aptitude Eligibility Test (GATE) qualified (95.56 percentile), India, 2003.

## **Organization and Communication**

Served as an active member of scientific seminars organizing committee to invite international speakers at Max Planck Institute of Biophysics, Frankfurt.

Served as student president and organized many inter-college events at Biology department at Maitreyi College, Delhi University, India.